

A parallel elastic and inelastic heterogeneous multiscale method for rate-independent materials

Zur Erlangung des akademischen Grades eines

DOKTORS DER NATURWISSENSCHAFTEN

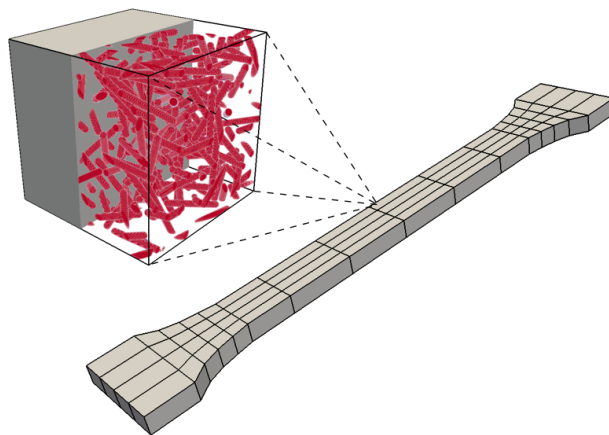
von der Fakultät für Mathematik des
Karlsruher Instituts für Technologie (KIT)

genehmigte

DISSERTATION

von

Ramin Shirazi Nejad



Tag der mündlichen Prüfung: 29. August 2017

1. Referent: Prof. Dr. Christian Wieners

2. Referent: Prof. Dr. Willy Dörfler

Acknowledgements

First and foremost, I would like to express my sincerest gratitude to my advisor Prof. Dr. Christian Wieners for giving me the opportunity to work on this interesting topic. In countless valuable discussions he inspired me with his deep mathematical knowledge. I thank him for his kind support and patience he gave me during my doctoral studies. I am also very thankful to Prof. Dr. Willy Dörfler for helpful improvement suggestions and being my second supervisor.

I gratefully acknowledge the Bundesministerium für Bildung und Forschung (BMBF) for funding the project MUltiskalenSIEmulation KOMpositen (MuSiKo) via 05M13VKA. Many thanks for the marvellous cooperation, the thesis would not have become to a successful completion without the support and valuable discussions on the workshops of each project partner of the MuSiKo team. My special thanks goes to Dr. Sarah Staub and student assistant Daniel Reinhardt of the Fraunhofer ITWM in Kaiserslautern for providing me the microstructures and its octree based interface as well as the experimental parameters and Celine Röhrig of the institute of technical mechanics of the University Saarbrücken for providing me the measured values of the experimental component tests.

I am grateful to the many dear colleagues at the research group for having a great time. I will never forget the countless battles at the table football. Moreover, I want to give my gratitude to my friends on which I always can count on when times are rough. In particular, I am also greatly indebted to Manfred Kröhnert for proofreading countless pages of meaningless mathematics.

Lastly, and most importantly, I thank my family for all their love and encouragement.

Ramin Shirazi Nejad, Karlsruhe in July 2017

Contents

1	Introduction	1
1.1	Basic concepts in multiscale modelling	1
1.2	State of the art in multiscale approximation	5
1.2.1	Analytical homogenization modelling schemes	5
1.2.2	Mathematical and numerical analysis of homogenization	5
1.2.3	Numerical homogenization schemes	6
1.2.4	Homogenization for rate-independent models	6
1.3	Goal and contribution	7
1.4	Outline	7
2	Thermodynamic principles in solid mechanics	9
2.1	Linear kinematics	9
2.2	Equilibria equations	12
2.3	Constitutive theory	13
2.3.1	Small deformations	13
2.3.2	Small strain constitutive relations	16
2.3.3	Materials with memory	17
2.3.4	Evolution of the inelastic material behavior	19
2.3.5	Generalized standard materials	19
3	Two-scale homogenization for linear elasticity	21
3.1	Asymptotic two-scale homogenization for linear elasticity	22
3.1.1	Oscillating small strain elasticity	22
3.1.2	Two-scale asymptotic expansion and convergence	22
3.1.3	Method of oscillating test functions	23
3.1.4	The unit cell and the homogenized problem	23
3.1.5	The numerical approach	24
3.2	Parallel heterogeneous two-scale FEM for linear elasticity	25
3.2.1	Small strain elasticity	25
3.2.2	The multiscale idea	26
3.2.3	The discrete multiscale setting	26

3.2.4	The multiscale problem	27
3.2.5	The two-scale problem and the multiscale tensor	27
3.2.6	The parallel two-scale model	29
4	Numerical experiments for linear elastic two-scale models	31
4.1	The experimental setting	31
4.1.1	Tensile testing	31
4.1.2	Materialography	32
4.2	Numerical setting	34
4.3	Numerical convergence analysis	35
4.4	Experiments for various fiber orientations and filler contents	42
5	Rate-independent material models with memory	47
5.1	Materials with memory	47
5.1.1	A simple damage model	48
5.1.2	Small strain elasto-plasticity	50
5.1.3	Damage and elasto-plasticity	52
5.2	The incremental problem	52
5.2.1	The incremental flow rule for the damage model	53
5.2.2	The incremental flow rule for elasto-plasticity	55
5.2.3	The incremental flow rule for damage and elasto-plasticity	57
6	Heterogeneous two-scale FEM for inelasticity	59
6.1	Two-scale models with memory	59
6.2	The incremental two-scale problem	60
6.2.1	The incremental two-scale damage problem	61
6.2.2	The incremental two-scale elasto-plasticity model	64
6.2.3	The incremental two-scale elasto-plastic damage model	65
6.3	The parallel nonlinear two-scale algorithm	66
7	Numerical experiments for inelastic material models	71
7.1	Monotonic tensile tests	71
7.1.1	Simple two-scale damage model	72
7.1.2	The two-scale elasto-plasticity model	75
7.1.3	Two-scale elasto-plasticity with damage	78
7.1.4	Various fiber orientations and filler contents	82
7.2	Cyclic component tests	87
7.2.1	Comparison of inelastic two-scale models	87
7.2.2	Reduced FE ² method	90

7.3	Numerical convergence analysis	91
8	Implementation	95
8.1	Parallel two-scale data structure	95
8.1.1	The parallelization scheme	96
8.1.2	The two-scale data structure	96
8.1.3	A storage reduced two-scale data structure	96
8.2	Strategies for data and storage reduction	98
8.2.1	A reduced internal variable representation	99
8.2.2	Interface for the representation of the microstructure	99
8.2.3	Working memory efficient microstructure representation	101
9	Conclusion and outlook	103
9.1	Summary and main results	103
9.2	Outlook and further applications	104
A	Fundamental tools from convex analysis and optimization	105
A.1	Optimality conditions for semi-smooth unconstrained problems	106
A.1.1	First order optimality condition	107
A.1.2	Existence of solutions	109
B	Hardware Specification	111
B.1	DELTA Cluster MA-PDE	111
B.2	Institute Cluster IC2	111
B.3	Forschungshochleistungsrechner ForHlr2	112
	Bibliography	115

Chapter 1

Introduction

Almost all products and applications we encounter in our daily life have a multiscale character. Some have a natural or biological origin such as wood or soil layers. However, in the last decades, sophisticated materials in engineering became steadily more important. Especially in the automotive and aerospace industry the use of composites is increasingly enforced in the field of lightweight constructions. Apart from cost cutting through weight reduction the material must be designed with the necessary stability to prevent premature failure under external influences. Further application fields involve inter alia: metal alloys, textiles, or polycrystalline materials. On closer examination, the properties of materials are influenced decisively by their micromechanical consistency. In order to select or to design appropriate materials for engineering applications [51, 14], the simulation of composites with a complex multiscale character is of great interest. For this purpose, a parallel realization of a heterogeneous multiscale method is introduced using a multigrid method with a highly scalable coarse grid solver. Particularly, this work is focusing on the numerical simulation of short fiber-reinforced materials. Various fiber orientations and filler contents for such composites vary widely in their overall macroscopic material behavior under external loading.

The compelling necessity for developing a heterogeneous multiscale method is described in the following section by means of introducing fundamental concepts in multiscale modelling for a simple linear elliptic problem class.

1.1 Basic concepts in multiscale modelling

Many phenomena with a multiscale character in science and engineering can be described by differential equations. As an introductory example, we consider the rainwater infiltration through a porous medium. This problem can be modeled as finding a solu-

tion $u_\delta : \Omega \rightarrow \mathbb{R}$ for the equations

$$\operatorname{div}(-\boldsymbol{\kappa}_\delta \nabla u_\delta) = 0 \quad \text{in } \Omega, \quad (1.1a)$$

$$\boldsymbol{\kappa}_\delta \nabla u_\delta \cdot \mathbf{n} = \mathbf{g}_N \quad \text{on } \Gamma_N, \quad (1.1b)$$

$$u_\delta = u_D \quad \text{on } \Gamma_D, \quad (1.1c)$$

with a highly oscillating permeability tensor $\boldsymbol{\kappa}_\delta \in \mathbb{R}_{\text{sym}}^{D \times D}$, a domain $\Omega \subset \mathbb{R}^D$ with $D = 2, 3$ and a Neumann and Dirichlet boundary $\Gamma_N \cup \Gamma_D = \partial\Omega$. The subscript δ emphasizes the multiscale character of the problem. In this example it is the measure of the length scale of the very small heterogeneity for a periodically continuous porous medium. In the following, we consider a $2D$ reduction of the porous medium equations for a fixed characteristic scale $\delta = 10^{-6}$ of the heterogeneity on the unit square domain $\Omega = (0, 1)^2$ with Neumann and Dirichlet boundary conditions given by

$$\begin{aligned} \boldsymbol{\kappa}_\delta \nabla u_\delta(x_1, x_2) \cdot \mathbf{n} &= (0, -1)^T & \text{for } x_2 = 1, \\ \boldsymbol{\kappa}_\delta \nabla u_\delta(x_1, x_2) \cdot \mathbf{n} &= (0, 0)^T & \text{for } x_1 = 0 \text{ and } x_2 = 0, \\ u_\delta(x_1, x_2) &= 0 & \text{for } x_1 = 0. \end{aligned}$$

To illustrate the rainwater infiltration through a porous medium on the fine-scale of a soil layer, we consider an artificial example for the permeability

$$\boldsymbol{\kappa}_\delta(x_1, x_2) = \begin{pmatrix} p_\delta(x_1, x_2) & 0 \\ 0 & p_\delta(x_1, x_2) \end{pmatrix}, \quad (1.2)$$

which is considered to be varying rapidly on the coarse-scale and modeled by the function

$$p_\delta(x_1, x_2) = 7.7^{((0.01 x_1 + 0.007625 x_2)/\delta) \bmod 7}.$$

The left hand side in Figure 1.1 shows the almost homogeneous appearing permeability distribution of (1.2) on the coarse-scale. However, upon closer inspection through an magnification, the heterogeneous structure can be clearly recognized, as shown on the right hand side in Figure 1.1. A straightforward spatial discretization with a finite element method of equation (1.1a) with (1.2) is inappropriate, because capturing the highly varying soil layer heterogeneities requires an extremely small mesh size. This results in a tremendous amount of degrees of freedom, which makes computation infeasible. This is mainly due to the fact that the method scales in the characteristic fine length δ of equation (1.1a). In Table 1.1, we observe the strongly to the scale of heterogeneity linked flux error. The flux error relates back to an insufficient evaluation through subsampling of some quadrature rule and provides a measure of the deviation for the conservation of the flux across the domain Ω defined by $\int_{\partial\Omega} \boldsymbol{\kappa}_\delta \nabla u_\delta \cdot \mathbf{n} \, da$. For a convergent method it is expected that the flux error disappears for a grid size $h \rightarrow 0$.

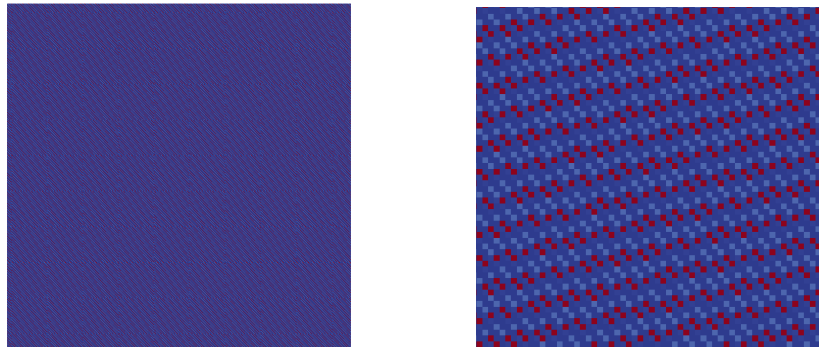


Figure 1.1: Illustration of the permeability κ_δ . Left: Permeability κ_δ of the entire domain Ω . Right: Enlarged section $\mathcal{K} \subset \Omega$ of the permeability κ_δ (approximately 7 times δ).

DoFs	Flux Error
263 169	34.0594
105 0625	20.0077
4 198 401	9.40926
16 785 409	10.0449

Table 1.1: Comparison of the flux error $\int_{\partial\Omega} \kappa_\delta \nabla u_\delta \cdot \mathbf{n} \, da$ for uniform mesh refinements using a classical finite element method.

All conclusions presented above motivate the need of an appropriate numerical approach. The most important demand is to establish a method which is independent of the fine-scale complexity δ . Particularly, the rapid progress regarding efficiency increase in computational power and working memory allows designing numerical homogenization schemes. For this reason, we address the treatment of the limit case of (1.1) for δ goes to zero in L_2 which implies the coarse-scale problem

$$\begin{aligned}
 \operatorname{div}(-\boldsymbol{\kappa}_0 \nabla u_0) &= 0 && \text{in } \Omega, \\
 \boldsymbol{\kappa}_0 \nabla u_0 \cdot \mathbf{n} &= \mathbf{g}_N && \text{on } \Gamma_N, \\
 u_0 &= u_D && \text{on } \Gamma_D.
 \end{aligned}$$

This raises the question, how the coarse-scale solution can be computed efficiently by an effective permeability tensor $\boldsymbol{\kappa}_0 \in \mathbb{R}_{\text{sym}}^{D \times D}$ that includes all the necessary fine-scale information. Classical homogenization schemes, e.g. see [64, 15], provide a possibility as discussed in the next section. Some are based on the principle idea of scale separation for periodic media. Therefore, in a representative domain $\mathcal{Y}_\xi = \xi + \delta(-0.5, 0.5)^2$ around specific sample points ξ on the coarse-scale, appropriate periodic boundary value

problems

$$\operatorname{div}(-\boldsymbol{\kappa}(\mathbf{e}_i + \nabla w_i)) = 0 \quad \text{in } \mathcal{Y}_\xi$$

are solved on the fine-scale corresponding to the standard basis \mathbf{e}_i of the space \mathbb{R}^D , where the fine-scale solutions w_i are \mathcal{Y}_ξ -periodic. In this treatment we use a permeability

$$\boldsymbol{\kappa} = \begin{cases} \boldsymbol{\kappa}_p & \text{in the pore,} \\ \boldsymbol{\kappa}_r & \text{in the rock,} \end{cases}$$

where $\boldsymbol{\kappa}_p = 0.075 \mathbf{I}$ and $\boldsymbol{\kappa}_r = 0.95 \mathbf{I}$ are the permeabilities of the pore and the rock, respectively. The symbol \mathbf{I} identifies the second order identity tensor. It turns out that depending on the fine-scale solutions an upscaled effective coarse response

$$\boldsymbol{\kappa}_0 \approx \begin{pmatrix} 0.2648 & -0.0019 \\ -0.0019 & 0.2167 \end{pmatrix}$$

can be constructed (see Section 3.2.5) replacing the highly varying permeability tensor in (1.2). Then, the coarse-scale solution u_0 is determined independently of the characteristic fine-scale δ . This results in a small flux error $\int_{\partial\Omega} \boldsymbol{\kappa}_0 \nabla u_0 \cdot \mathbf{n} \, da = 5.3e-4$ and a computation time of 4 minutes and 41 seconds using 32 cores on a single node on the DELTA B.1 cluster for solving two fine and the coarse-scale boundary value problems with 4 206 593 degrees of freedom on the fine-scale and 66 049 on the coarse-scale. Figure 1.2 shows the microstructural permeability of the representative domain \mathcal{Y}_ξ and the homogenized coarse-solution u_0 in the domain Ω of the heterogeneous multiscale method [64]. The two fine-scale solutions w_i , used to determine the constant effective coarse response, of the periodic boundary value problems of the representative domain are shown in Figure 1.3.

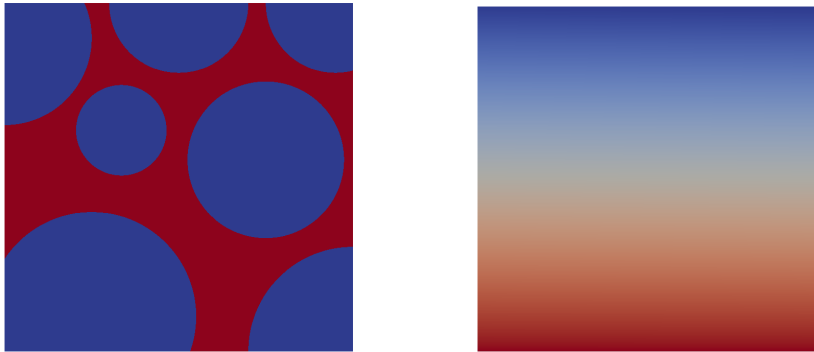


Figure 1.2: *Left: Permeability $\boldsymbol{\kappa}_r = 0.95 \mathbf{I}$ for the rock and $\boldsymbol{\kappa}_p = 0.075 \mathbf{I}$ for the pore of the porous representative fine domain $\mathcal{Y}_\xi = \xi + \delta(-0.5, 0.5)^2$. Right: Coarse-scale solution u_0 of the heterogeneous rainwater infiltration of the domain $\Omega = (0, 1)^2$.*

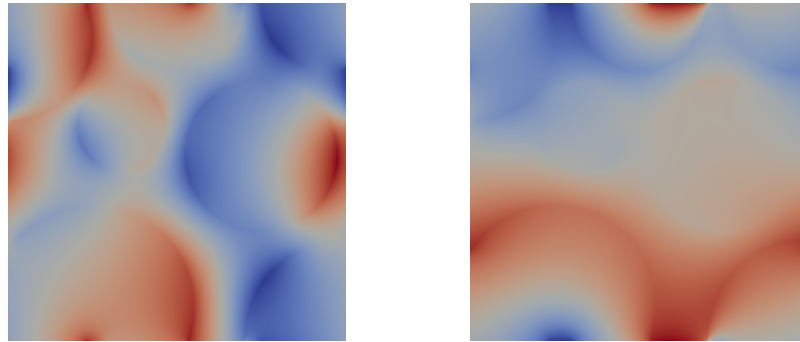


Figure 1.3: Fine-scale solutions w_i corresponding to the standard basis e_i of the space \mathbb{R}^D for $i = 1$ on the left hand side and $i = 2$ on the right hand side of the representative domain \mathcal{Y}_ξ for evaluating the homogenized permeability tensor κ_0 .

1.2 State of the art in multiscale approximation

Up to now, many numerical homogenization techniques in continuum mechanics have been discussed to describe an appropriate scale transition of the micromechanical processes adequately. The extensive amount of literature for various methods from the early 1900's up to the present is reviewed briefly in this section.

1.2.1 Analytical homogenization modelling schemes

The *rule of mixture* is the simplest form for describing an effective response by weighting the different material phase properties by their volume fraction. This method was first introduced by Reuss [50] and Voigt [63]. The *mean-field method* is an analytical homogenization technique including the Eshelby tensor [17]. Eshelby introduced the theory of a single ellipsoidal equivalent inclusion in an infinitely large matrix. Many extensions based upon the Eshelby approach can be found. In particular, these include the self-consistent method by Kröner [29, 23], the generalized self-consistent scheme, see e.g. [9] and Mori-Tanaka's method [43] with the same name, just to name a few. All these methods have an inaccurate effective material response in common due to strong limited microstructural assumptions. On the other hand, these assumptions usually result in over and underestimations, respectively.

1.2.2 Mathematical and numerical analysis of homogenization

Classical mathematical homogenization techniques such as G-, H- and Γ -convergence demonstrate solely the existence of an effective quantity without providing an explicit

expression, see for instance [58, 57, 47, 61, 12, 7]. The fundamentals of asymptotic homogenization typically allows describing micromechanical behavior more accurately. This mathematical concept for composite media dates back to Bensoussan [48], Sanchez-Palencia and Zaoui [52] and Bakhvalov and Passenko [6]. The asymptotic homogenization follows the idea of asymptotic expansion for continuous periodically oscillating variational problems with test functions oscillating in the same phase, see for instance [11]. If the solution u_δ of equation (1.1a) converges weakly to the coarse-solution u_0 in the limit case $\delta \rightarrow 0$, it leads to an explicit expression for the effective response on the coarse-scale by solving suitable unit cell problems on the fine-scale. The classical analysis of two-scale homogenization and convergence for linear and nonlinear elliptic equations can be found in [3]. An approach for solving arbitrary linear second order elliptic problems is described in [33] and for porous media in [5].

1.2.3 Numerical homogenization schemes

The *heterogeneous multiscale method* for linear elliptic problems with a complete error analysis was first introduced by E and Engquist [64]. Its origin lies in the variational asymptotic homogenization for periodic micro-problems. For linear elasticity the heterogeneous multiscale method coincides with the *finite element square* (FE²) approach as presented by Feyel and Chaboche [18] and Smit [56], as well as Miehe [36, 37], which states a homogenization scheme for nonlinear continuum mechanics models.

1.2.4 Homogenization for rate-independent models

In addition to the already presented approaches, an FE² method considering a progressive continuum mechanics damage model is introduced in [59, 60]. Here, the microscopic boundary value problems are replaced by an equivalent problem, as proposed in [30, 13], which can be efficiently solved by a fast Fourier transformation, see [44]. A general overview of the FE² method is given in [53] and, in particular, the treatment of an elasto-plasticity model can be found.

All these methods consider energetic formulations for rate-independent material models, e.g. see [38, 40, 41]. A two-scale convergence assertion for rate-independent energetic material models of generalized standard materials with periodic coefficients for two-scale homogenization can be found in [42]. This work also contains an existence and uniqueness statement. An introductory overview on the analysis for rate-independent systems can be found in [39].

1.3 Goal and contribution

The goal of this thesis is to develop a highly scalable and parallel heterogeneous multi-scale method to efficiently compute the linear and, in particular, the nonlinear behavior for rate-independent material models with a complex microstructure. For this purpose, we propose an FE² methodology working massively in parallel using a multigrid method with a highly scalable coarse grid solver to speed up the complex computations on the micro-scale. This process can be used for the numerical and metrological analysis of short fiber-reinforced materials to refrain from consuming component tests in the future. The realization is divided into two parts as described in the following:

First, an efficient two-scale algorithm of a solid body $\Omega \subset \mathbb{R}^D$ with $D = 2, 3$ for the linear small strain elasticity

$$\begin{aligned} -\operatorname{div} \boldsymbol{\sigma}_\delta(\boldsymbol{\varepsilon}(\mathbf{u}_\delta)) &= \mathbf{b} && \text{in } \Omega, \\ \boldsymbol{\sigma}_\delta(\boldsymbol{\varepsilon}(\mathbf{u}_\delta))\mathbf{n} &= \mathbf{t}_N && \text{on } \Gamma_N, \\ \mathbf{u}_\delta &= \mathbf{u}_D && \text{on } \Gamma_D, \end{aligned}$$

is proposed with displacement $\mathbf{u}_\delta \in \mathbb{R}^D$, strain $\boldsymbol{\varepsilon} \in \mathbb{R}_{\text{sym}}^{D \times D}$, stress $\boldsymbol{\sigma}_\delta \in \mathbb{R}_{\text{sym}}^{D \times D}$, body force $\mathbf{b} \in \mathbb{R}^D$, surface traction $\mathbf{t}_N \in \mathbb{R}^D$ on the Neumann boundary Γ_N and Dirichlet boundary condition $\mathbf{u}_D \in \mathbb{R}^D$ on Γ_D .

Next, the linear case is extended to nonlinear material models by means of the generalized standard materials

$$\begin{aligned} -\operatorname{div} \boldsymbol{\sigma}_\delta(\boldsymbol{\varepsilon}(\mathbf{u}_\delta), \mathbf{z}_\delta) &= \mathbf{b} && \text{in } \Omega, \\ \boldsymbol{\sigma}_\delta(\boldsymbol{\varepsilon}(\mathbf{u}_\delta), \mathbf{z}_\delta)\mathbf{n} &= \mathbf{t}_N && \text{on } \Gamma_N, \\ \mathbf{u}_\delta &= \mathbf{u}_D && \text{on } \Gamma_D, \\ \dot{\mathbf{z}}_\delta &\in \Phi(\boldsymbol{\varepsilon}(\mathbf{u}_\delta), \mathbf{z}_\delta) && \text{in } \Omega, \end{aligned}$$

with a history variable $\mathbf{z}_\delta \in \mathbb{R}^N$ whose evolution is described with the plastic potential \mathcal{R}^* through a multivalued flow rule $\Phi = \partial \mathcal{R}^*$ to state thermodynamically admissible states.

1.4 Outline

The thesis is structured in eight chapters, each providing the following contributions.

Chapter 2 gives a brief introduction to continuum mechanics for elastic and inelastic solids. Here, kinematical relations and quasi-static equilibria equations for small strain

elasticity and generalized standard materials are stated and thermodynamic principles are presented to describe a closed constitutive theory.

The classical asymptotic homogenization for small strain elasticity and its two-scale model is introduced in Chapter 3. Moreover, a parallel realization of a classical heterogeneous multiscale method is presented.

Several numerical experiments for small deformations are investigated in Chapter 4. Here, we focus on component testing of short fiber-reinforced polymers with varying fiber filler content and fiber orientation. Furthermore, an experimental convergence analysis is examined for various scales of heterogeneities on the fine-scale for the small strain two-scale method.

In order to describe the micromechanical proceedings like damage and plasticity phenomenologically, several inelastic material models are presented in Chapter 5. Furthermore, a brief introduction into continuum damage mechanics is given.

Various rate-independent inelastic two-scale models described by a history variable are presented in Chapter 6. In addition, a parallel heterogeneous multiscale method using an FE^2 approach for the computation of the inelastic behavior for rate-independent material models is introduced.

Chapter 7 extends the numerical experiments for small deformations to inelastic material models. For the optimization with regard to efficiency and working memory issues of the complex inelastic two-scale experiments a reduced FE^2 method is introduced. Here, within a region of interest, we use a finer discretization for the representation of the variables on the fine-scale. The behavior in convergence for the nonlinear damage model is only discussed on the fine-scale using the reduced FE^2 approach, due to the complexity of the inelastic two-scale method.

A modular and flexible data structure for energetic material models of the generalized standard material type and reduction methods for optimization issues developed in this thesis is described in Chapter 8. These models are based on a parallelized two-scale data structure and allow for reducing the consumption of working memory.

Chapter 9 concludes with a summary and an outlook containing possible future extensions.

Chapter 2

Thermodynamic principles in solid mechanics

This chapter gives a brief introduction into the continuum mechanics framework for solids. At first, a body's deformation process is described by kinematic relations. Then, with this result the equilibria equations of linear and angular momentum can be stated. After that, principles of thermodynamic are introduced to deduce constitutive relations for elastic materials. For describing the inelastic material evolution the introduction of further assumptions are required. Altogether, this approach results in a description of a material body by partial differential equations and, in case of inelastic material behavior, in an additional differential inclusion for the constitutive plastic evolution.

An extensive body of literature exists, covering continuum mechanics. For instance, see [34, 21, 24], for a more complete treatment of this topic.

2.1 Linear kinematics

Continuum mechanics aims for a relation between applying forces and motion of bodies embedded in a three dimensional Euclidean space endowed with a metric $\|\mathbf{x}\|_2 = (\mathbf{x} \cdot \mathbf{x})^{\frac{1}{2}}$ whose coordinates are denoted by x , y and z . It is assumed that a body is described by an infinite set of material points continuously distributed in space. Under the influence of external forces, the body moves and deforms, respectively. This can be described geometrically with kinematical relations. In order to prevent that a material point of a body either can be created, nor be annihilated, the motion of a deformation is a time-parametrized one to one mapping $\varphi(t, \mathbf{X}) = \mathbf{x}$ between a material points initial position \mathbf{X} of the reference configuration Ω and a material points final position \mathbf{x} of the current configuration $\widehat{\Omega}$, which defines, as illustrated in the sketch in Figure 2.1, the

displacement field

$$\mathbf{u}(t, \mathbf{X}) = \varphi(t, \mathbf{X}) - \mathbf{X}.$$

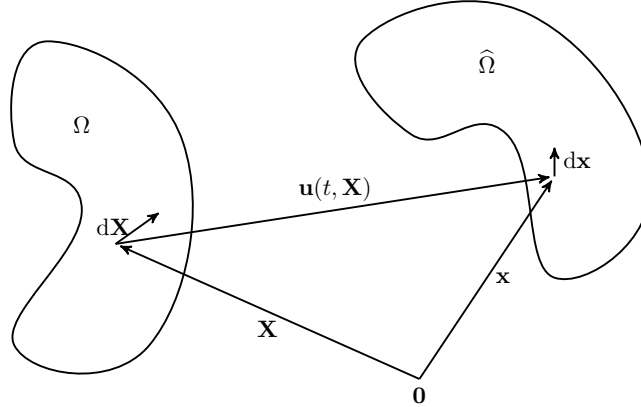


Figure 2.1: Illustration of the motion $\varphi(t, \mathbf{X})$ of a body from the reference configuration Ω into the current configuration $\hat{\Omega}$.

A motion applied by a translation or rotation does not change the shape or the volume of a body and is called a *rigid body motion*. On the other hand it is called a *deformation* if the volume of the body changes. This happens every time when the displacement between two or the angle between three neighboring material points changes. Infinitesimal changes of the deformation can be described by the displacement gradient $\nabla \mathbf{u}$. It maps a line element $d\mathbf{X}$ of the undeformed configuration Ω to a line element $d\mathbf{x}$ of the current configuration $\hat{\Omega}$. However, it is no suitable measure for the deformation process, since it includes rigid body motions. Therefore, we introduce the strain measure. For this purpose, we take a closer look on an infinitesimal volume element $dV = dx dy dz$ of the body for the special case of small deformations, i.e. $\|\nabla \mathbf{u}\|_2 \ll 1$, and therefore the distinction between reference and current configuration disappears. Then, the displacement $\mathbf{u} = (u_x, u_y, u_z)$ can be represented by the first order term of the Taylor expansion in each component. Exemplarily, we consider linearizations of the componentwise displacements in the xy -plane

$$\begin{aligned} u_x(t, x + dx, y, z) &= u_x(t, x, y, z) + \partial_x u_x(t, x, y, z) dx, \\ u_x(t, x, y + dy, z) &= u_x(t, x, y, z) + \partial_y u_x(t, x, y, z) dy, \\ u_y(t, x + dx, y, z) &= u_y(t, x, y, z) + \partial_x u_y(t, x, y, z) dx, \end{aligned}$$

which is sufficient for an adequate description for the measure in strain. Then, the relative change in the length of an infinitesimal volume element in the direction of the

x -axis as illustrated on the right hand side in Figure 2.2 is determined by the so called *elongation*

$$\varepsilon_x = \frac{u_x(x + dx, y, z) - u_x(x, y, z)}{dx} = \partial_x u_x.$$

Analogously, the elongations, also known as *normal shear* in y and z -direction, are determined by

$$\varepsilon_y = \partial_y u_y \quad \text{and} \quad \varepsilon_z = \partial_z u_z.$$

The change of the right angle of an infinitesimal volume element in the xy -plane is described by the *shear strain* τ_{xy} . As illustrated on the right hand side in Figure 2.2 it is divided into two angles, i.e.

$$\tau_{xy} = \alpha + \beta.$$

Because of small deformations, i.e. $\alpha \ll 1$ and $\beta \ll 1$, holds approximately that $\alpha \approx \tan \alpha$ and $\beta \approx \tan \beta$. This implies that the angles can be described in terms of the displacement such that

$$\alpha = \frac{u_x(x, y + dy, z) - u_x(x, y, z)}{dy} = \partial_y u_x$$

and

$$\beta = \frac{u_y(x + dx, y, z) - u_y(x, y, z)}{dx} = \partial_x u_y.$$

In the same manner, the shear in the xz and yz -plane is determined by

$$\tau_{xz} = \partial_z u_x + \partial_x u_z \quad \text{and} \quad \tau_{yz} = \partial_y u_x + \partial_x u_y.$$

In conclusion, the entire deformation is described by an *infinitesimal strain tensor*

$$\boldsymbol{\varepsilon} = \begin{pmatrix} \varepsilon_x & \frac{1}{2}\tau_{xy} & \frac{1}{2}\tau_{xz} \\ \frac{1}{2}\tau_{yx} & \varepsilon_y & \frac{1}{2}\tau_{yz} \\ \frac{1}{2}\tau_{zx} & \frac{1}{2}\tau_{zy} & \varepsilon_z \end{pmatrix},$$

which is symmetric, i.e. $\tau_{xy} = \tau_{yx}$, $\tau_{xz} = \tau_{zx}$ and $\tau_{yz} = \tau_{zy}$. The strain tensor has 6 independent components and can be represented by the displacement gradient, i.e.

$$\boldsymbol{\varepsilon}(\mathbf{u}) = \text{sym}(\nabla \mathbf{u}) = \frac{1}{2}(\nabla \mathbf{u} + (\nabla \mathbf{u})^T).$$

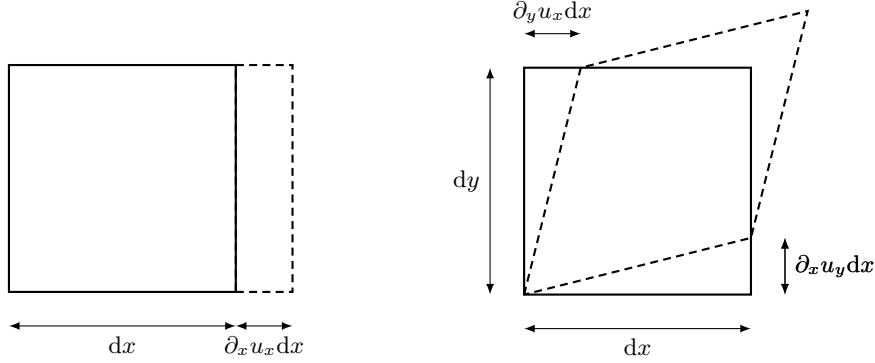


Figure 2.2: Deformations of an infinitesimal volume element dV in the xy -plane. Left: Changes caused by the normal strain in the x -direction. Right: Changes of the right angle caused by the shear strain.

2.2 Equilibria equations

In this section we establish basic equations of conservation in continuum mechanics to determine the motion of a body during external loading, see for instance [21, 10, 22].

Small strain deformations occurring from slowly displacements give rise to quasi-static considerations and therefore kinematic terms will be ignored here. The process proceeds so slowly that the state between two equilibria is infinitesimally close. The quasi-static equilibrium for a stationary object has no net force and is defined by Newton's first law of motion. So the balance of momentum is defined by the equilibrium

$$\int_{\Omega} \mathbf{b} \, dx + \int_{\Gamma_N} \mathbf{t}_N \, da = 0 \quad (2.1)$$

with body forces $\mathbf{b} : [0, T] \times \Omega \rightarrow \mathbb{R}^D$ and surface tractions $\mathbf{t}_N : [0, T] \times \Gamma_N \rightarrow \mathbb{R}^D$. It is well known by Cauchy's Theorem that there exists a second order tensor field $\boldsymbol{\sigma}$ called *Cauchy stress* such that the surface traction \mathbf{t}_N depends linear on the normal \mathbf{n} , i.e.

$$\mathbf{t}_N = \boldsymbol{\sigma} \mathbf{n} \quad \text{on } \Gamma_N, \quad (2.2)$$

see for instance [10, 21]. Now, inserting Cauchy's surface traction relation (2.2) into the second term of the global equilibrium (2.1) and subsequently applying the divergence theorem yields

$$\int_{\Gamma_N} \boldsymbol{\sigma} \mathbf{n} \, da = \int_{\Omega} \operatorname{div} \boldsymbol{\sigma} \, dx$$

and by inserting this into equation (2.1) we obtain the local equation of the equilibrium

$$\mathbf{b} + \operatorname{div} \boldsymbol{\sigma} = 0. \quad (2.3)$$

It is well known that the conservation of angular momentum

$$\int_{\Omega} (\mathbf{x} - \mathbf{x}_0) \times \mathbf{b} \, d\mathbf{x} + \int_{\Gamma_N} (\mathbf{x} - \mathbf{x}_0) \times \mathbf{t}_N \, da = 0$$

requires the symmetry of the Cauchy stress tensor

$$\boldsymbol{\sigma} = \boldsymbol{\sigma}^T.$$

In order to determine a complete material model we need a relation between the stress and strain to define a solvable boundary value problem as described in the following sections for the small strain elasticity and a material which is described by internal variables.

2.3 Constitutive theory

In this section, we follow thermodynamic principles to deduce constitutive relations for small strain elasticity. After that, we extend this to inelastic materials which are described by memory variables. For a more complete treatment, see for instance [55, 22].

2.3.1 Small deformations

In the continuous problem, the displacement vector $\mathbf{u} : [0, T] \times \Omega \rightarrow \mathbb{R}^D$ of the equilibrium equation (2.3) is characterized by minimizing (see Theorem 2.1) the *total strain energy*

$$\mathcal{E}(t, \mathbf{u}) = \int_{\Omega} W(\mathbf{x}, \boldsymbol{\varepsilon}(\mathbf{u})) \, d\mathbf{x} - \langle \ell(t), \mathbf{u} \rangle$$

subject to boundary conditions $\mathbf{u} = \mathbf{u}_D$ on $\Gamma_D \subset \partial\Omega$. Here, a *load functional*

$$\langle \ell(t), \mathbf{u} \rangle = \int_{\Omega} \mathbf{b} \cdot \mathbf{u} \, d\mathbf{x} + \int_{\Gamma_N} \mathbf{t}_N \cdot \mathbf{u} \, da,$$

with body forces $\mathbf{b} : [0, T] \times \Omega \rightarrow \mathbb{R}^D$ and surface tractions $\mathbf{t}_N : [0, T] \times \Gamma_N \rightarrow \mathbb{R}^D$ is applied, and the load dependency on the displacement \mathbf{u} is neglected by assuming dead loads, i.e. \mathbf{b} and \mathbf{t}_N do not depend on the time.

A fundamental concept in thermodynamics is the *conservation of energy* which is stated by the first law of thermodynamics. It stipulates that the rate of internal energy equals the rate of work done to the body by mechanical forces and is characterized by

$$\int_{\Omega} \dot{W}(\mathbf{x}, \boldsymbol{\varepsilon}(\mathbf{u})) \, d\mathbf{x} - \langle \ell(t), \dot{\mathbf{u}} \rangle = 0.$$

Another fundamental concept in thermodynamics describes the irreversibility of processes in type of randomness by the increase of entropy and is given by the second law of thermodynamics. In continuum mechanics, we typically express this law by the Clausius–Duhem inequality for an isothermal deformation process, i.e. temperature changes are neglected. The Clausius–Duhem inequality states that the rate of internal energy is bounded by the external power contribution

$$\int_{\Omega} \dot{W}(\mathbf{x}, \boldsymbol{\varepsilon}(\mathbf{u})) \, d\mathbf{x} \leq \langle \ell(t), \dot{\mathbf{u}} \rangle.$$

The work per unit time by the acting forces defines the *external power*

$$\langle \ell(t), \dot{\mathbf{u}} \rangle = \int_{\Omega} \mathbf{b} \cdot \dot{\mathbf{u}} \, d\mathbf{x} + \int_{\Gamma_N} \mathbf{t}_N \cdot \dot{\mathbf{u}} \, da.$$

Next, we demonstrate that the external power contribution can be expressed in terms of the *stress power*. Following the equation of the equilibrium (2.3) and Cauchy’s surface traction relation (2.2) yields

$$\langle \ell(t), \dot{\mathbf{u}} \rangle = \int_{\Omega} -\operatorname{div} \boldsymbol{\sigma} \cdot \dot{\mathbf{u}} \, d\mathbf{x} + \int_{\Gamma_N} \boldsymbol{\sigma} \mathbf{n} \cdot \dot{\mathbf{u}} \, da.$$

Focusing on the first term in combination with the identity $\operatorname{div}(\boldsymbol{\sigma} \mathbf{u}) = \operatorname{div} \boldsymbol{\sigma} \mathbf{u} + \boldsymbol{\sigma} : \nabla \mathbf{u}$ it follows that

$$\int_{\Omega} -\operatorname{div} \boldsymbol{\sigma} \cdot \dot{\mathbf{u}} \, d\mathbf{x} = \int_{\Omega} (\boldsymbol{\sigma} : \nabla(\dot{\mathbf{u}}) - \operatorname{div}(\boldsymbol{\sigma} \cdot \dot{\mathbf{u}})) \, d\mathbf{x}.$$

Inserting this expression into the external power equation together with the identity $\boldsymbol{\sigma} : \nabla \mathbf{u} = \boldsymbol{\sigma} : \boldsymbol{\varepsilon}(\mathbf{u})$ and applying the divergence theorem states that it is equivalent to the stress power

$$\langle \ell(t), \dot{\mathbf{u}} \rangle = \int_{\Omega} \boldsymbol{\sigma} : \dot{\boldsymbol{\varepsilon}}(\mathbf{u}) \, d\mathbf{x}$$

where the strain rate $\dot{\boldsymbol{\varepsilon}}(\mathbf{u}) = \boldsymbol{\varepsilon}(\dot{\mathbf{u}})$ was introduced in the last step. The *local dissipation* is then represented by the Clausius–Duhem inequality in the form that

$$\boldsymbol{\sigma} : \dot{\boldsymbol{\varepsilon}}(\mathbf{u}) - \dot{W}(\mathbf{x}, \boldsymbol{\varepsilon}(\mathbf{u})) \geq 0. \quad (2.4)$$

Now, we are able to determine thermodynamically admissible constitutive relations.

In order to describe a linear elastic material behavior it is assumed that the constitutive functions take the form that the *Helmholtz free energy* $W(\mathbf{x}, \boldsymbol{\varepsilon}(\mathbf{u}))$ and the stress $\boldsymbol{\sigma}(\mathbf{x}, \boldsymbol{\varepsilon}(\mathbf{u}))$ are only depending on the linearized strain $\boldsymbol{\varepsilon}(\mathbf{u}) = \operatorname{sym}(\nabla \mathbf{u})$ at each material point \mathbf{x} and therefore it follows, that the local dissipation in (2.4) takes the form

$$(\boldsymbol{\sigma} - \partial_{\boldsymbol{\varepsilon}} W(\mathbf{x}, \boldsymbol{\varepsilon}(\mathbf{u}))) : \dot{\boldsymbol{\varepsilon}}(\mathbf{u}) \geq 0.$$

The fact that the dissipation inequality holds true for any possible choice of the strain rate $\dot{\boldsymbol{\varepsilon}}$ states that the dissipation vanishes. This leads to the following correlation between the stress and the strain defined by

$$\boldsymbol{\sigma} = \partial_{\boldsymbol{\varepsilon}} W(\mathbf{x}, \boldsymbol{\varepsilon}(\mathbf{u})). \quad (2.5)$$

A body which is fulfilling the correlation of the stress and the strain by equation (2.5) is called *hyperelastic*. Introducing the *small strain isotropic elastic energy*

$$W(\mathbf{x}, \boldsymbol{\varepsilon}(\mathbf{u})) = \frac{1}{2} \mathbb{C}(\mathbf{x})[\boldsymbol{\varepsilon}(\mathbf{u})] : \boldsymbol{\varepsilon}(\mathbf{u}) \quad (2.6)$$

only depending on the linearized strain $\boldsymbol{\varepsilon}(\mathbf{u}) = \text{sym}(\nabla \mathbf{u})$ yields that *Hooke's law* holds true

$$\boldsymbol{\sigma} = \mathbb{C}(\mathbf{x})[\boldsymbol{\varepsilon}(\mathbf{u})]. \quad (2.7)$$

An isotropic material behavior is then described by

$$\mathbb{C}(\mathbf{x})[\boldsymbol{\varepsilon}(\mathbf{u})] = \lambda(\mathbf{x}) \text{trace}(\boldsymbol{\varepsilon}(\mathbf{u})) : \mathbf{I} + 2\mu(\mathbf{x})\boldsymbol{\varepsilon}(\mathbf{u})$$

with *Lamé constants* $\lambda(\mathbf{x}) \geq 0$ and $\mu(\mathbf{x}) > 0$. The Lamé constants describe the material specific elasticity at each material point of an isotropic medium.

The conservation of energy as well as linear and angular momentum in combination with the constitutive law and the Cauchy stress relation motivates the statement of the fundamental theorem of elasticity.

Theorem 2.1

Let $\Omega \subset \mathbb{R}^D$ be a Lipschitz domain and $\mathbf{b} \in L_2(\Omega, \mathbb{R}^D)$. Then exists a unique minimizer $\mathbf{u} \in H_0^1(\Omega; \mathbb{R}^D)$ of the total strain energy $\mathcal{E}(\cdot)$ with $\mathbf{u} = \mathbf{u}_D$ on the Dirichlet boundary $\Gamma_D \subset \partial\Omega$ with positive measure $|\Gamma_D|_{D-1} > 0$ satisfying the equations

$$\begin{aligned} -\text{div } \boldsymbol{\sigma}(\mathbf{x}, \boldsymbol{\varepsilon}(\mathbf{u})) &= \mathbf{b} && \text{in } \Omega, \\ \boldsymbol{\sigma}(\mathbf{x}, \boldsymbol{\varepsilon}(\mathbf{u}))\mathbf{n} &= \mathbf{t}_N && \text{on } \Gamma_N, \end{aligned}$$

for $\boldsymbol{\sigma} = \mathbb{C}(\mathbf{x})[\boldsymbol{\varepsilon}(\mathbf{u})]$ with $\boldsymbol{\sigma} = \boldsymbol{\sigma}^T$.

Proof. The assertion can be shown straightforwardly by establishing the weak formulation. For this purpose, multiply the local linear balance equation (2.3) with test functions in suitable spaces and integrate over the domain Ω . Because of the two identities $\boldsymbol{\varepsilon}(\mathbf{u}) : \boldsymbol{\sigma} = \nabla \mathbf{u} : \boldsymbol{\sigma}$ and $\text{div } \boldsymbol{\sigma} \cdot \mathbf{u} = \text{div}(\boldsymbol{\sigma} \cdot \mathbf{u}) - \boldsymbol{\sigma} : \nabla \mathbf{u}$ and subsequently applying

the divergence theorem, we derive a symmetric bilinearform defined by the quadratic small strain energy density (2.6), which allows an equivalent representation by the energy minimization. Due to Korn's inequality the total strain energy $\mathcal{E}(\cdot)$ is uniformly convex, which assures the existence and uniqueness of the minimizer in $H_0^1(\Omega; \mathbb{R}^D)$ for a positive measure $|\Gamma_D|_{D-1} > 0$. \square

Here, we used the Hilbert space $L_2(\Omega, \mathbb{R}^D)$ that contains all functions which are componentwise quadratically integrable over Ω and the Sobolev space $H_0^1(\Omega, \mathbb{R}^D)$ that contains all functions that vanishes on the boundary $\partial\Omega$ whose weak derivative belongs to the Hilbert space $L_2(\Omega, \mathbb{R}^D)$.

2.3.2 Small strain constitutive relations

For a linear elastic continuum the constitutive relation between stress and strain is a linear mapping which is defined by Hooke's law (2.7). A general fourth order stiffness tensor $\mathbb{C}(\mathbf{x})$ has 81 independent components and describes the mechanical strength of a medium at each material point \mathbf{x} . It reduces to 36 independent elastic material constants due to the symmetry of the Cauchy stress and the strain. Finally, the symmetry of the mixed partial derivative with respect to the strain of the quadratic small strain energy density (2.6) defines the stiffness tensor

$$\mathbb{C}(\mathbf{x}) = \partial_{\boldsymbol{\varepsilon}}^2 W(\mathbf{x}, \boldsymbol{\varepsilon}(\mathbf{u}))$$

and hence it reduces to 21 independent elastic constants to describe an anisotropic material behavior. Such a material law is called *triclinic* and exhibits in different orientations a different material behavior. Using Voigt notation it can be represented by a symmetric fourth order stiffness tensor

$$\mathbb{C} = \begin{pmatrix} C_{11} & C_{12} & C_{13} & C_{14} & C_{15} & C_{16} \\ C_{12} & C_{22} & C_{23} & C_{24} & C_{25} & C_{26} \\ C_{13} & C_{23} & C_{33} & C_{34} & C_{35} & C_{36} \\ C_{14} & C_{24} & C_{34} & C_{44} & C_{45} & C_{46} \\ C_{15} & C_{25} & C_{35} & C_{45} & C_{55} & C_{56} \\ C_{16} & C_{26} & C_{36} & C_{46} & C_{56} & C_{66} \end{pmatrix}.$$

These are all planes of symmetries which are exclusively defined by the mathematical continuum mechanical model. Further reductions can be found by studying specific material structures of a solid body.

The stiffness matrix for a unidirectional reinforced composite reduces to 5 independent elastic constants due to the isotropy in the plane orthogonally aligned to the rotational

axis. A continuum with this property is called *transversely isotropic* and is exemplarily defined for a preferable direction z as rotational axis by the symmetric fourth order tensor which can be written as

$$\mathbb{C} = \begin{pmatrix} C_{11} & C_{12} & C_{13} & 0 & 0 & 0 \\ C_{12} & C_{11} & C_{13} & 0 & 0 & 0 \\ C_{13} & C_{13} & C_{33} & 0 & 0 & 0 \\ 0 & 0 & 0 & C_{23} & 0 & 0 \\ 0 & 0 & 0 & 0 & C_{23} & 0 \\ 0 & 0 & 0 & 0 & 0 & \frac{1}{2}(C_{11} - C_{12}) \end{pmatrix}.$$

An isotropic medium possesses the same material behavior in all directions. It has the most symmetries and reduces to 2 independent elastic constants and is represented by a symmetric fourth order stiffness tensor of the form

$$\mathbb{C} = \begin{pmatrix} C_{11} & C_{12} & C_{12} & 0 & 0 & 0 \\ C_{12} & C_{11} & C_{12} & 0 & 0 & 0 \\ C_{12} & C_{12} & C_{11} & 0 & 0 & 0 \\ 0 & 0 & 0 & \frac{1}{2}(C_{11} - C_{12}) & 0 & 0 \\ 0 & 0 & 0 & 0 & \frac{1}{2}(C_{11} - C_{12}) & 0 \\ 0 & 0 & 0 & 0 & 0 & \frac{1}{2}(C_{11} - C_{12}) \end{pmatrix}.$$

To ensure that Theorem 2.1 remains valid for the various constitutive relations discussed in this section they have to fulfill that $\mathbb{C}[\boldsymbol{\varepsilon}(\mathbf{u})] : \boldsymbol{\varepsilon}(\mathbf{u}) \geq \alpha \|\boldsymbol{\varepsilon}(\mathbf{u})\|^2$ for a constant $\alpha > 0$.

2.3.3 Materials with memory

For the inelastic evolution of displacements $\mathbf{u}: [0, T] \times \Omega \rightarrow \mathbb{R}^D$ in the time interval $[0, T]$ of a material which is described by internal variables $\mathbf{z}: [0, T] \times \Omega \rightarrow \mathbb{R}^N$ the total energy functional takes the form

$$\mathcal{E}(t, \mathbf{u}, \mathbf{z}) = \int_{\Omega} W(\mathbf{x}, \boldsymbol{\varepsilon}(\mathbf{u}), \mathbf{z}) \, d\mathbf{x} - \langle \ell(t), \mathbf{u} \rangle$$

with local energy W only depending on the quantities $\boldsymbol{\varepsilon}(t, \mathbf{x})$ and $\mathbf{z}(t, \mathbf{x})$ at time t and material point \mathbf{x} and the load functional

$$\langle \ell(t), \mathbf{u} \rangle = \int_{\Omega} \mathbf{b}(t) \cdot \mathbf{u} \, d\mathbf{x} + \int_{\Gamma_N} \mathbf{t}_N(t) \cdot \mathbf{u} \, da$$

defined by volume forces $\mathbf{b}: [0, T] \times \Omega \rightarrow \mathbb{R}^D$ and body forces $\mathbf{t}_N: [0, T] \times \Gamma_N \rightarrow \mathbb{R}^D$ is applied.

Again, we follow the thermodynamic principles as introduced in the previous section. Then, the local dissipation requires that

$$(\boldsymbol{\sigma} - \partial_{\boldsymbol{\varepsilon}}W(\mathbf{x}, \boldsymbol{\varepsilon}(\mathbf{u}), \mathbf{z})) : \dot{\boldsymbol{\varepsilon}}(\mathbf{u}) - \partial_{\mathbf{z}}W(\mathbf{x}, \boldsymbol{\varepsilon}(\mathbf{u}), \mathbf{z}) : \dot{\mathbf{z}} \geq 0.$$

Since the first term holds for arbitrary strain rates $\dot{\boldsymbol{\varepsilon}}$, we derive for a material with memory Hooke's generalized law

$$\boldsymbol{\sigma} = \partial_{\boldsymbol{\varepsilon}}W(\mathbf{x}, \boldsymbol{\varepsilon}(\mathbf{u}), \mathbf{z})$$

and the Clausius–Duhem inequality for a material with memory collapses to

$$-\partial_{\mathbf{z}}W(\mathbf{x}, \boldsymbol{\varepsilon}(\mathbf{u}), \mathbf{z}) : \dot{\mathbf{z}} \geq 0.$$

This motivates to define the conjugate variable $\mathbf{y} = -\partial_{\mathbf{z}}W(\mathbf{x}, \boldsymbol{\varepsilon}(\mathbf{u}), \mathbf{z})$. In order to specify the inelastic material behavior, additional constitutive assumptions are necessary. A convenient assumption for a correlation of the conjugate pair \mathbf{y} and \mathbf{z} is the *principle of maximum dissipation*, e.g. see [68, 67], which is stated as follows:

$$\max_{\mathbf{y} \in \mathbb{R}^N} \mathbf{y} : \dot{\mathbf{z}} \quad \text{subject to } \mathcal{F}(\mathbf{y}) \leq 0. \quad (2.8)$$

In order to obtain an associative flow rule we assume in the following that the yield surface $\mathcal{F}(\mathbf{y}) = 0$ is convex and bounded. In what follows, this motivates to define the set of thermodynamically admissible states $\mathcal{C} = \{\mathbf{y} \in \mathbb{R}^N : \mathcal{F}(\mathbf{y}) \leq 0\}$. An irreversible material response takes place whenever the thermodynamic force \mathbf{y} lies on the yield surface $\partial\mathcal{C} = \{\mathbf{y} \in \mathbb{R}^N : \mathcal{F}(\mathbf{y}) = 0\}$. Otherwise, the response is elastic if the conjugate variable \mathbf{y} lies in the interior of the elastic region $\text{int}\mathcal{C} = \{\mathbf{y} \in \mathbb{R}^N : \mathcal{F}(\mathbf{y}) < 0\}$. By defining the *plastic potential*

$$\mathcal{R}^*(\mathbf{y}) = \begin{cases} 0 & \mathbf{y} \in \mathcal{C}, \\ +\infty & \text{otherwise,} \end{cases}$$

the principle of maximum dissipation defines a semi-smooth unconstrained optimization problem which can be expressed by the support function

$$\mathcal{R}(\dot{\mathbf{z}}) = \sup_{\mathbf{y} \in \mathbb{R}^N} (\langle \mathbf{y}, \dot{\mathbf{z}} \rangle - \mathcal{R}^*(\mathbf{y})) = \sup_{\mathbf{y} \in \mathcal{C}} \langle \mathbf{y}, \dot{\mathbf{z}} \rangle.$$

It is well known that the support function of an indicator function corresponding to a convex cone coincides with the indicator function of its convex polar cone, i.e.

$$\mathcal{R}(\dot{\mathbf{z}}) = \begin{cases} 0 & \dot{\mathbf{z}} \in \mathcal{C}^*, \\ +\infty & \text{otherwise.} \end{cases}$$

2.3.4 Evolution of the inelastic material behavior

The evaluation of the inelastic material behavior which is described by internal variables is as described in Appendix A. We aim for finding a critical point of the total energy functional with respect to the maximum dissipation principle that can be written as

$$\min (\mathcal{E}(t, \mathbf{u}, \mathbf{z}) + \mathcal{R}(\dot{\mathbf{z}})) . \quad (2.9)$$

According to Moreau and Rockafellar [16, Chap. I, Prop. 5.6], the flow rule is determined by

$$-\partial_{\mathbf{z}}\mathcal{E}(t, \mathbf{u}, \mathbf{z}) \in \partial\mathcal{R}(\dot{\mathbf{z}})$$

and by duality an alternative representation is defined by the differential inclusion

$$\dot{\mathbf{z}} \in \partial\mathcal{R}^*(-\partial_{\mathbf{z}}\mathcal{E}(t, \mathbf{u}, \mathbf{z})) ,$$

where $\mathbf{y} = -\partial_{\mathbf{z}}\mathcal{E}(t, \mathbf{u}, \mathbf{z}) = -\partial_{\mathbf{z}}W(\mathbf{x}, \boldsymbol{\varepsilon}(\mathbf{u}), \mathbf{z})$ applies. One can easily check that the subdifferential of the plastic potential $\partial\mathcal{R}^*(\mathbf{y}) = \{\mathbf{z} \in \mathbb{R}^N : \mathcal{R}^*(\mathbf{w}) \geq \mathcal{R}^*(\mathbf{y}) + \mathbf{z} \cdot (\mathbf{w} - \mathbf{y}) \text{ for all } \mathbf{w} \in \mathbb{R}^N\}$ is a normal cone $N_{\mathcal{C}}(\mathbf{x}) = \{\mathbf{z} \in \mathbb{R}^N : \mathbf{z} \cdot (\mathbf{w} - \mathbf{y}) \leq 0 \text{ for all } \mathbf{y} \in \mathcal{C}\}$ corresponding to the convex set of thermodynamically admissible states \mathcal{C} . Then, by studying optimality conditions the flow rule can be evaluated by the complementarity conditions

$$\lambda \geq 0, \quad \mathcal{F}(\mathbf{y}) \leq 0, \quad \mathcal{F}(\mathbf{y})\lambda = 0$$

and the normality rule

$$\dot{\mathbf{z}} = \lambda \partial\mathcal{F}(\mathbf{y}) ,$$

i.e. the flow rule is associative. However, the consistency parameter λ can be obtained from an equivalent formulation by a Lagrangian functional as the minimizer of (2.9) which also states the normality rule for a convex potential \mathcal{R} , cf. Appendix A. Here, we mention that the complementarity condition remains valid for perfect plasticity with hardening, otherwise dual spaces have to be defined.

2.3.5 Generalized standard materials

The construction of the dissipation functional by the principle of maximum dissipation defines the prototype for generalized standard materials, e.g. see [2]. Now, we assume

that history variables $\mathbf{z} : [0, T] \times \Omega \rightarrow \mathbb{R}^N$, a response function $\boldsymbol{\sigma}$, and a multi-valued evolution function Φ exist, satisfying

$$\begin{aligned} -\operatorname{div} \boldsymbol{\sigma}(\boldsymbol{\varepsilon}(\mathbf{u}), \mathbf{z}) &= \mathbf{b} && \text{in } \Omega, \\ \boldsymbol{\sigma}(\boldsymbol{\varepsilon}(\mathbf{u}), \mathbf{z})\mathbf{n} &= \mathbf{t}_N && \text{on } \Gamma_N, \\ \mathbf{u} &= \mathbf{u}_D && \text{on } \Gamma_D, \\ \dot{\mathbf{z}} &\in \Phi(\boldsymbol{\varepsilon}(\mathbf{u}), \mathbf{z}) && \text{in } \Omega. \end{aligned}$$

A simple possibility to obtain an admissible evolution function Φ is the introduction of a convex potential $\mathcal{R}^* : \mathbb{R}^N \rightarrow [0, \infty]$ with $\mathcal{R}^*(\mathbf{0}) = 0$ such that

$$\Phi(\boldsymbol{\varepsilon}(\mathbf{u}), \mathbf{z}) = \partial\mathcal{R}^*(\mathbf{y}) = \{\mathbf{z} \in \mathbb{R}^N : \mathcal{R}^*(\mathbf{w}) \geq \mathcal{R}^*(\mathbf{y}) + \mathbf{z} \cdot (\mathbf{w} - \mathbf{y}) \text{ for all } \mathbf{w} \in \mathbb{R}^N\}$$

depending on $\mathbf{y} = -\partial_{\mathbf{z}}W(\mathbf{x}, \boldsymbol{\varepsilon}(\mathbf{u}), \mathbf{z})$. This guarantees $\mathbf{y} \cdot \partial\mathcal{R}^*(\mathbf{y}) \geq 0$ and thus thermodynamic admissibility for all $\mathbf{y} \in \operatorname{dom}(\mathcal{R}^*) = \{\mathbf{y} \in \mathbb{R}^N : \mathcal{R}^*(\mathbf{y}) < \infty\}$. We postpone the discussion of the existence of an energetic solution to the following chapter.

Chapter 3

Two-scale homogenization for linear elasticity

This chapter introduces the framework of two-scale schemes for elasticity and the realization of a parallel two-scale algorithm using a classical homogenization methodology.

The goal of material modeling in continuum mechanics is to deduce constitutive laws sufficiently realistically. Mostly used in this treatment are two-scale modeling schemes.

The perspective of measure in two-scale modeling is divided in:

- Microscopic view: Treatment and formulation of elementary inelastic micromechanical phenomena like damage or plasticity within the framework of continuum mechanics in terms of constitutive relations.
- Macroscopic view: Treatment of global deformation due to inelastic material effects in terms of an upscaled effective material response.

Many inelastic material processes as damage or plasticity proceed on the micro-scale. An appropriate level that is small enough to describe micromechanical processes adequately is defined by the *representative volume element* (RVE). The RVE order of magnitude depends on the material's constitution. It is the smallest measure of the continuum to represent a sufficiently accurate constitutive response. The two-scale method relies on the following definitions:

- The definition of the RVE and the modeling of the heterogeneous microstructure.
- The definition of the continuum mechanics model to describe the material specific properties through a micro-scale boundary value problem.
- The definition of the scale-transition via an effective upscaled constitutive material response.
- The definition of the macro-scale boundary value problem through averaged physical quantities.

3.1 Asymptotic two-scale homogenization for linear elasticity

Here, we present the classical analytical concept of asymptotic homogenization [48, 52, 6] on the basis of small strain elasticity as introduced in Section 3.2.1. This concept will be extended in the following sections to define a numerical approach of homogenization, in particular, for rate-independent materials.

3.1.1 Oscillating small strain elasticity

We aim at finding a family of two-scale solutions $\mathbf{u}_\delta \in H_0^1(\Omega; \mathbb{R}^D)$ over a domain $\Omega \subset \mathbb{R}^D$ for $D = 2, 3$ of the variational equation

$$\int_{\Omega} \mathbb{C}_\delta(\mathbf{x})[\boldsymbol{\varepsilon}(\mathbf{u}_\delta)(\mathbf{x})] : \boldsymbol{\varepsilon}(\mathbf{v}_\delta) \, d\mathbf{x} = \langle \boldsymbol{\ell}, \mathbf{v}_\delta \rangle \quad \text{for all } \mathbf{v}_\delta \in H_0^1(\Omega; \mathbb{R}^D) \quad (3.1)$$

with a highly varying constitutive relation $\mathbb{C}_\delta(\mathbf{x})$. Here, we restrict to the case that the highly oscillating quantity can continuous periodically represented on a rescaled unit cell $\mathcal{Y} = (0, 1)^D$ for a very small period δ , i.e. $\mathbb{C}_\delta(\mathbf{x}) = \mathbb{C}(\mathbf{x}, \frac{\mathbf{x}}{\delta}) = \mathbb{C}(\mathbf{x}, \mathbf{y})$ where $\mathbb{C}(\mathbf{x}, \cdot)$ is \mathcal{Y} -periodic for each given $\mathbf{x} \in \Omega$.

3.1.2 Two-scale asymptotic expansion and convergence

In order to find a solution of equation (3.1) we follow the theory of asymptotic homogenization which rest upon the principle assumption of an existing asymptotic expansion for the two-scale solution

$$\mathbf{u}_\delta(\mathbf{x}) = \mathbf{u}_0\left(\mathbf{x}, \frac{\mathbf{x}}{\delta}\right) + \delta \mathbf{u}_1\left(\mathbf{x}, \frac{\mathbf{x}}{\delta}\right) + O(\delta^2), \quad (3.2)$$

with corresponding \mathcal{Y} -periodic functions $\mathbf{u}_0(\mathbf{x}, \cdot)$ and $\mathbf{u}_1(\mathbf{x}, \cdot)$ for each given $\mathbf{x} \in \Omega$. With the compact embedding $H_0^1(\Omega; \mathbb{R}^D) \subset L_2(\Omega; \mathbb{R}^D)$ and the uniformly boundedness of the asymptotic two-scale solution \mathbf{u}_δ , it is well known that the solution converges weakly in $H_0^1(\Omega; \mathbb{R}^D)$ against the coarse-scale solution which does not depend on \mathbf{y} , i.e. there exists a function $\mathbf{u} \in L_2(\Omega, \mathbb{R}^D)$ such that $\mathbf{u}_0(\mathbf{x}, \mathbf{y}) = \mathbf{u}(\mathbf{x})$, e.g. see [4, Chap. 2, Prop. 2.5]. Hence, the coarse-scale solution \mathbf{u} is independent of the multiscale character δ . With the same arguments, the asymptotic gradient $\nabla \mathbf{u}_\delta$ converges weakly in $H_0^1(\Omega; \mathbb{R}^D)$ against $\nabla \mathbf{u}(\mathbf{x}) + \nabla_{\mathbf{y}} \mathbf{u}_1(\mathbf{x}, \mathbf{y})$, again see [4, Chap. 2, Prop. 2.5].

3.1.3 Method of oscillating test functions

Tartar proposed, e.g. see [11], to use test functions oscillating with the same resonance

$$\mathbf{v}_\delta(\mathbf{x}) = \mathbf{v}(\mathbf{x}) + \delta \mathbf{v}_1\left(\mathbf{x}, \frac{\mathbf{x}}{\delta}\right) \quad (3.3)$$

for a \mathcal{Y} -periodic function $\mathbf{v}_1(\mathbf{x}, \cdot)$ at any given $\mathbf{x} \in \Omega$. Inserting the asymptotic two-scale expansion (3.2) and the oscillating test functions (3.3) into the initial problem (3.1) and subsequently applying the limit process $\delta \rightarrow 0$ results in finding a slowly varying and a rapidly oscillating solution $(\mathbf{u}, \mathbf{u}_1) \in H_0^1(\Omega; \mathbb{R}^D) \times L_2(\Omega, H_{\text{per}}^1(\mathcal{Y}; \mathbb{R}^D))$ of the two-scale weak form

$$\int_{\Omega} \int_{\mathcal{Y}} \mathbb{C}(\mathbf{y})[\boldsymbol{\varepsilon}(\mathbf{u})(\mathbf{x}) + \boldsymbol{\varepsilon}_{\mathbf{y}}(\mathbf{u}_1)(\mathbf{x}, \mathbf{y})] : (\boldsymbol{\varepsilon}(\mathbf{v})(\mathbf{x}) + \boldsymbol{\varepsilon}_{\mathbf{y}}(\mathbf{v}_1)(\mathbf{x}, \mathbf{y})) \, d\mathbf{y} \, d\mathbf{x} = \langle \boldsymbol{\ell}, \mathbf{v} \rangle \quad (3.4)$$

for test functions $(\mathbf{v}, \mathbf{v}_1) \in H_0^1(\Omega; \mathbb{R}^D) \times L_2(\Omega, H_{\text{per}}^1(\mathcal{Y}; \mathbb{R}^D))$ and $\boldsymbol{\varepsilon}_{\mathbf{y}}(\mathbf{u}) = \frac{1}{2}(\nabla_{\mathbf{y}}\mathbf{u} + (\nabla_{\mathbf{y}}\mathbf{u})^T)$, where $H_{\text{per}}^1(\mathcal{Y}, \mathbb{R}^D)$ denotes the restriction of periodic $H_{\text{loc}}^1(\mathbb{R}^D, \mathbb{R}^D)$ functions to \mathcal{Y} . Equation (3.4) can be decoupled into two variational equations with respect to their test functions. First we choose $\mathbf{v}_1 = 0$ and then $\mathbf{v} = 0$ which leads for finding a solution $(\mathbf{u}, \mathbf{u}_1) \in H_0^1(\Omega; \mathbb{R}^D) \times L_2(\Omega, H_{\text{per}}^1(\mathcal{Y}; \mathbb{R}^D))$ of the weak variational system

$$\int_{\Omega} \int_{\mathcal{Y}} \mathbb{C}(\mathbf{y})[\boldsymbol{\varepsilon}(\mathbf{u})(\mathbf{x}) + \boldsymbol{\varepsilon}_{\mathbf{y}}(\mathbf{u}_1)(\mathbf{x}, \mathbf{y})] : \boldsymbol{\varepsilon}(\mathbf{v})(\mathbf{x}) \, d\mathbf{y} \, d\mathbf{x} = \langle \boldsymbol{\ell}, \mathbf{v} \rangle, \quad (3.5)$$

$$\int_{\Omega} \int_{\mathcal{Y}} \mathbb{C}(\mathbf{y})[\boldsymbol{\varepsilon}(\mathbf{u})(\mathbf{x}) + \boldsymbol{\varepsilon}_{\mathbf{y}}(\mathbf{u}_1)(\mathbf{x}, \mathbf{y})] : \boldsymbol{\varepsilon}_{\mathbf{y}}(\mathbf{v}_1)(\mathbf{x}, \mathbf{y}) \, d\mathbf{y} \, d\mathbf{x} = 0, \quad (3.6)$$

for $\mathbf{v}_0 \in H_0^1(\Omega; \mathbb{R}^D)$ and $\mathbf{v}_1 \in L_2(\Omega, H_{\text{per}}^1(\mathcal{Y}; \mathbb{R}^D))$. An equivalent formulation of equation (3.6) is at finding a solution $\mathbf{u}_1(\mathbf{x}, \cdot) \in H_{\text{per}}^1(\mathcal{Y}; \mathbb{R}^D)$ for each given $\mathbf{x} \in \Omega$ of the \mathcal{Y} -periodic local form

$$\int_{\mathcal{Y}} \mathbb{C}(\mathbf{y})[\boldsymbol{\varepsilon}(\mathbf{u})(\mathbf{x}) + \boldsymbol{\varepsilon}_{\mathbf{y}}(\mathbf{u}_1)(\mathbf{x}, \mathbf{y})] : \boldsymbol{\varepsilon}_{\mathbf{y}}(\mathbf{v}_1)(\mathbf{x}, \mathbf{y}) \, d\mathbf{y} = 0 \quad \text{for } \mathbf{v}_1 \in H_{\text{per}}^1(\mathcal{Y}; \mathbb{R}^D). \quad (3.7)$$

3.1.4 The unit cell and the homogenized problem

By introducing a symmetric tensor basis $\boldsymbol{\eta}_1, \dots, \boldsymbol{\eta}_6$ of $\text{Sym}(3) = \mathbb{R}_{\text{sym}}^{3 \times 3}$ the strain on the coarse-scale can be written as $\boldsymbol{\varepsilon}(\mathbf{u}) = \sum_{j=1}^6 (\boldsymbol{\varepsilon}(\mathbf{u}) : \boldsymbol{\eta}_j) \boldsymbol{\eta}_j$ which defines the linearity relation of the strongly oscillating fine-scale solution

$$\mathbf{u}_1(\mathbf{x}, \mathbf{y}) = \sum_{j=1}^6 (\boldsymbol{\varepsilon}(\mathbf{u})(\mathbf{x}) : \boldsymbol{\eta}_j) \mathbf{w}_j(\mathbf{y}). \quad (3.8)$$

As a result of the strain representation and the relation (3.8) by substituting into (3.5) and (3.7), the coarse-scale solution $\mathbf{u} \in H_0^1(\Omega; \mathbb{R}^D)$ of the homogenized equation

$$\int_{\Omega} \mathbb{C}^*[\boldsymbol{\varepsilon}(\mathbf{u})(\mathbf{x})] : \boldsymbol{\varepsilon}(\mathbf{v})(\mathbf{x}) \, d\mathbf{x} = \langle \boldsymbol{\ell}, \mathbf{v} \rangle \quad \text{for all } \mathbf{v}_1 \in H_0^1(\Omega; \mathbb{R}^D) \quad (3.9)$$

is defined through the upscaled constant effective constitutive response

$$\mathbb{C}^* = \sum_{k,j=1}^6 \left(\frac{1}{|\mathcal{Y}|} \int_{\mathcal{Y}} \mathbb{C}(\mathbf{y})[\boldsymbol{\eta}_j + \boldsymbol{\varepsilon}(\mathbf{w}_j)(\mathbf{y})] : \boldsymbol{\eta}_k \, d\mathbf{y} \right) \boldsymbol{\eta}_j \otimes \boldsymbol{\eta}_k,$$

where the fluctuation $\mathbf{w}_j \in H_{\text{per}}^1(\mathcal{Y}; \mathbb{R}^D)$ is determined by solving local unit cell problems

$$\int_{\mathcal{Y}} \mathbb{C}(\mathbf{y})[\boldsymbol{\eta}_j + \boldsymbol{\varepsilon}(\mathbf{w}_j)(\mathbf{y})] : \boldsymbol{\varepsilon}_{\mathbf{y}}(\mathbf{v}_1)(\mathbf{x}, \mathbf{y}) \, d\mathbf{y} = 0 \quad \text{for each } \mathbf{v}_1 \in H_{\text{per}}^1(\mathcal{Y}; \mathbb{R}^D). \quad (3.10)$$

3.1.5 The numerical approach

The main advantage of asymptotic homogenization for developing a numerical approach is that the discretization of the coarse-scale weak formulation (3.9) is independent of the cost for the characteristic fine-scale δ through an upscaled effective material response. This is achieved by introducing some quadrature rules for evaluating the integrals of the coarse-scale problem (3.9) numerically and reformulating the local unit cell problems (3.10) by equivalent boundary value problems around each integration point $\xi \in \Xi_H$ through an RVE $\mathcal{Y}_{\xi} \subset \Omega$ as discussed in more detail in the following sections. The effective coarse response is then defined by an RVE averaged quantity at each material point. Figure 3.1 illustrates the approaches of the numerical and the analytical homogenization scheme whose solution $(\mathbf{u}, \mathbf{u}_1)$ lies in $\Omega \times \mathcal{Y} \subset \mathbb{R}^{2D}$.



Figure 3.1: Comparison of the numerical two-scale homogenization approach (left) with RVEs $\mathcal{Y}_{\xi} \subset \Omega$ around each integration point $\xi \in \Xi_H \subset \Omega$ and the analytical asymptotic homogenization scheme (right) with continuously distributed unit cell problems \mathcal{Y} for almost each $\mathbf{x} \in \Omega$.

3.2 Parallel heterogeneous two-scale FEM for linear elasticity

We introduce the two-scale FEM for elastic solids in $\Omega \subset \mathbb{R}^D$ with $D = 2, 3$ in the case of small deformations. The method aims at approximating the material's deformation with a coarse mesh size H in a heterogeneous medium with much smaller characteristic length scale δ .

3.2.1 Small strain elasticity

In the continuous problem the displacement vector $\mathbf{u} : \Omega \rightarrow \mathbb{R}^D$ is characterized by minimizing the total energy

$$\mathcal{E}(\mathbf{u}) = \int_{\Omega} W(\mathbf{x}, \boldsymbol{\varepsilon}(\mathbf{u})) \, d\mathbf{x} - \langle \ell, \mathbf{u} \rangle$$

subject to boundary conditions $\mathbf{u} = \mathbf{u}_D$ on $\Gamma_D \subset \partial\Omega$. Here, a load functional

$$\langle \ell, \mathbf{u} \rangle = \int_{\Omega} \mathbf{b} \cdot \mathbf{u} \, d\mathbf{x} + \int_{\Gamma_N} \mathbf{t}_N \cdot \mathbf{u} \, da,$$

with body forces $\mathbf{b} : \Omega \rightarrow \mathbb{R}^D$ and surface tractions $\mathbf{t}_N : \Gamma_N \rightarrow \mathbb{R}^D$ is applied, and the small strain isotropic elastic energy is of the form

$$W(\mathbf{x}, \boldsymbol{\varepsilon}) = \frac{1}{2} \mathbb{C}(\mathbf{x})[\boldsymbol{\varepsilon}(\mathbf{x})] : \boldsymbol{\varepsilon}(\mathbf{x})$$

only depending on the linearized strain $\boldsymbol{\varepsilon} = \boldsymbol{\varepsilon}(\mathbf{u})$ with $\boldsymbol{\varepsilon}(\mathbf{u}) = \text{sym}(\nabla \mathbf{u})$.

We consider the case that $\mathbb{C}(\cdot)$ is strongly inhomogeneous and cannot be resolved on coarse meshes of mesh size H . For example, we consider the case that $\mathbb{C}(\cdot)$ can be resolved only on a mesh size $h < \delta$ with $\delta \ll H$, so that it is not feasible to compute the full fine mesh solution in Ω .

In our model, we use the spaces for the displacements $V = H^1(\Omega, \mathbb{R}^N)$ and $V(\mathbf{0}) = \{\mathbf{v} \in V : \mathbf{v} = \mathbf{0} \text{ on } \Gamma_D\}$ including homogeneous boundary conditions on the Dirichlet boundary $\Gamma_D \subset \partial\Omega$.

Due to Korn's inequality the total strain energy $\mathcal{E} : V \rightarrow \mathbb{R}$ is uniformly convex, which assures the existence and uniqueness of an energetic solution in a suitable space $V(\mathbf{0})$ for a positive measure $|\Gamma_D|_{D-1} > 0$.

3.2.2 The multiscale idea

A multiscale method aims at approximating the exact solution \mathbf{u} on the coarse level in a finite element space with mesh size parameter $H > 0$, where the coarse approximation \mathbf{u}_H (referred to as *macro-solution*) is obtained by solving a suitable averaged problem. Therefore, we define a suitable averaged energy $\mathcal{E}_H(\cdot)$ so that the coarse approximation can be determined as minimizer of this energy.

The construction of the averaged energy relies on the solution of local problems in representative volume elements

$$\mathcal{Y}_\xi = \xi + \delta(-0.5, 0.5)^D \subset \Omega$$

at sample points $\xi \in \Xi_H \subset \Omega$. On the RVEs we locally define micro-solutions $\mathbf{u}_{\xi,h} = \mathbf{u}_{\xi,H} + \mathbf{v}_{\xi,h}$, where $\mathbf{u}_{\xi,H}$ is the linearization of the macro-solution and $\mathbf{v}_{\xi,h}$ is the so called *micro-fluctuation*. This is approximated in a finite element space with mesh size parameter $h > 0$.

The heterogeneous multiscale method extends the two-scale homogenization of periodic microstructures to applications, where the microstructure in every RVE is representative for at least a small neighborhood extending the RVE. It is a modeling assumption that a periodic continuation of the micro-fluctuation is appropriate. These assumptions are quite restrictive, but they allow for a full mathematical analysis of the homogenization error, which is enhanced by the modeling error due to the approximation of the heterogeneous microstructure (see [64]).

3.2.3 The discrete multiscale setting

Let $\Omega \subset \mathbb{R}^D$ be a Lipschitz domain and define the space $V = H^1(\Omega; \mathbb{R}^D)$. For given Dirichlet data \mathbf{u}_D , we define the affine space $V(\mathbf{u}_D) = \{\mathbf{v} \in V : \mathbf{v} = \mathbf{u}_D \text{ on } \Gamma_D \subset \partial\Omega\}$. The macro-solution is approximated in a finite element space $V_H \subset V$, and we set

$$V_H(\mathbf{u}_D) = \{\mathbf{v}_H \in V_H : \mathbf{v}_H(\mathbf{x}) = \mathbf{u}_D(\mathbf{x}) \text{ for all nodal points } \mathbf{x} \in \Gamma_D\}.$$

On the mesh corresponding to V_H , we select quadrature points $\Xi_H \subset \Omega$ with weights ω_ξ for $\xi \in \Xi_H$, and we introduce the notation

$$\int_{\Xi_H} f(\xi) = \sum_{\xi \in \Xi_H} \omega_\xi f(\xi) \approx \int_{\Omega} f(\mathbf{x}) \, d\mathbf{x}.$$

We assume that the quadrature is exact for $\varepsilon(\mathbf{u}_H)$. In every RVE, the micro-fluctuation is locally approximated in a finite element space $V_{\xi,h} \subset V_\xi$ with

$$V_\xi = \left\{ \mathbf{v}_\xi \in H_{\text{per}}^1(\mathcal{Y}_\xi, \mathbb{R}^D) : \int_{\mathcal{Y}_\xi} \mathbf{v}_\xi \, d\mathbf{x} = 0 \right\},$$

where $H_{\text{per}}^1(\mathcal{Y}_\xi, \mathbb{R}^D)$ denotes the restriction of periodic $H_{\text{loc}}^1(\mathbb{R}^D, \mathbb{R}^D)$ functions to \mathcal{Y}_ξ . On the micro-scale we set the global finite element approximation space as the product space $V_h = \prod_{\xi \in \Xi_H} V_{\xi,h}$. Furthermore, we assume that the elasticity tensor $\mathbb{C}(\mathbf{x})$ for $\mathbf{x} \in \mathcal{Y}_\xi$ is representative for the material properties in a neighborhood of any sample point $\xi \in \Xi_H$.

3.2.4 The multiscale problem

The multiscale approximation represented by the macro-solution and the micro-fluctuations in every RVE is defined as the minimizer $(\mathbf{u}_H, \mathbf{v}_h) \in V_H(\mathbf{u}_D) \times V_h$ of the two-scale energy

$$\mathcal{E}_H(\mathbf{u}_H, \mathbf{v}_h) = \int_{\Xi_H} W_\xi(\boldsymbol{\varepsilon}(\mathbf{u}_H), \mathbf{v}_{\xi,h}) - \langle \ell, \mathbf{u}_H \rangle,$$

where the micro-energy is evaluated on the RVEs by

$$W_\xi(\boldsymbol{\varepsilon}_H, \mathbf{v}_{\xi,h}) = \frac{1}{|\mathcal{Y}_\xi|} \int_{\mathcal{Y}_\xi} W(\mathbf{x}, \boldsymbol{\varepsilon}_H(\xi) + \boldsymbol{\varepsilon}(\mathbf{v}_{\xi,h})) \, d\mathbf{x}$$

depending on the strain $\boldsymbol{\varepsilon}_H = \boldsymbol{\varepsilon}(\mathbf{u}_H)$ of the macro-solution and micro-fluctuations $\mathbf{v}_{\xi,h}$. In the RVE we define the linear approximation of the macro-solution by $\mathbf{u}_{\xi,H}(\mathbf{x}) = \mathbf{u}_H(\xi) + \nabla \mathbf{u}_H(\xi)(\mathbf{x} - \xi)$. Together with the micro-fluctuation this defines the micro-solution $\mathbf{u}_{\xi,h} = \mathbf{u}_{\xi,H} + \mathbf{v}_{\xi,h}$, so that by construction $\mathbf{u}_{\xi,h} - \mathbf{u}_{\xi,H}$ is periodic, and the strain of the macro-solution $\boldsymbol{\varepsilon}_{\xi,H} = \boldsymbol{\varepsilon}(\mathbf{u}_{\xi,H}) \equiv \boldsymbol{\varepsilon}(\mathbf{u}_H)(\xi)$ is constant in the RVE \mathcal{Y}_ξ .

3.2.5 The two-scale problem and the multiscale tensor

The minimizer of the two-scale energy is characterized as the critical point of the two-scale energy: find $(\mathbf{u}_H, \mathbf{v}_h) \in V_H(\mathbf{u}_D) \times V_h$ satisfying

$$\text{Macro-Equilibrium} \quad 0 = \partial_{\mathbf{u}} \mathcal{E}_H(\mathbf{u}_H, \mathbf{v}_h), \quad (3.11a)$$

$$\text{Micro-Equilibrium} \quad 0 = \partial_{\mathbf{v}} \mathcal{E}_H(\mathbf{u}_H, \mathbf{v}_h). \quad (3.11b)$$

This means solving the coupled linear problems

$$\sum_{\xi} \frac{\omega_{\xi}}{|\mathcal{Y}_{\xi}|} \int_{\mathcal{Y}_{\xi}} \mathbb{C}(\mathbf{x})[\boldsymbol{\varepsilon}(\mathbf{u}_H)(\xi) + \boldsymbol{\varepsilon}(\mathbf{v}_{\xi,h})(\mathbf{x})] : \boldsymbol{\varepsilon}(\delta \mathbf{u}_H)(\xi) \, d\mathbf{x} = \langle \ell, \delta \mathbf{u}_H \rangle, \quad (3.12a)$$

$$\frac{1}{|\mathcal{Y}_{\xi}|} \int_{\mathcal{Y}_{\xi}} \mathbb{C}(\mathbf{x})[\boldsymbol{\varepsilon}(\mathbf{u}_H)(\xi) + \boldsymbol{\varepsilon}(\mathbf{v}_{\xi,h})(\mathbf{x})] : \boldsymbol{\varepsilon}(\delta \mathbf{v}_{\xi,h}) \, d\mathbf{x} = 0 \quad (3.12b)$$

for test functions $(\delta \mathbf{u}_H, \delta \mathbf{v}_{\xi,h}) \in V_H(\mathbf{0}) \times V_{\xi,h}$.

Now, we reduce this system to an averaged macro-problem. Therefore, we introduce an orthonormal basis $\boldsymbol{\eta}_1, \dots, \boldsymbol{\eta}_6$ of $\text{Sym}(3) = \mathbb{R}_{\text{sym}}^{3 \times 3}$. Corresponding to this basis we compute micro-fluctuations $\mathbf{w}_{\xi,h,1}, \dots, \mathbf{w}_{\xi,h,6} \in V_{\xi,h}$ that solve

$$\frac{1}{|\mathcal{Y}_\xi|} \int_{\mathcal{Y}_\xi} \mathbb{C}(\mathbf{x})[\boldsymbol{\eta}_j + \boldsymbol{\varepsilon}(\mathbf{w}_{\xi,h,j})] : \boldsymbol{\varepsilon}(\delta \mathbf{v}_{\xi,h}) \, d\mathbf{x} = 0, \quad \delta \mathbf{v}_{\xi,h} \in V_{\xi,h}. \quad (3.13)$$

Inserting the representation of the macro-strain $\boldsymbol{\varepsilon}_{\xi,H} = \boldsymbol{\varepsilon}(\mathbf{u}_H)(\xi)$ with respect to the basis

$$\boldsymbol{\varepsilon}_{\xi,H} = \sum_{j=1}^6 \left(\boldsymbol{\varepsilon}_{\xi,H} : \boldsymbol{\eta}_j \right) \boldsymbol{\eta}_j,$$

we obtain for the micro-fluctuation solving (3.12b)

$$\mathbf{v}_{\xi,h} = \sum_{j=1}^6 \left(\boldsymbol{\varepsilon}_{\xi,H} : \boldsymbol{\eta}_j \right) \mathbf{w}_{\xi,h,j}.$$

This is now inserted into the macro-equation (3.12a), which yields

$$\int_{\Xi_H} \mathbb{C}_{\xi,H}[\boldsymbol{\varepsilon}(\mathbf{u}_H)] : \boldsymbol{\varepsilon}(\delta \mathbf{u}_H) = \langle \ell, \delta \mathbf{u}_H \rangle, \quad \delta \mathbf{u}_H \in V_H(\mathbf{0})$$

with the two-scale elasticity tensor

$$\mathbb{C}_{\xi,H} = \sum_{j,k=1}^6 \left(\frac{1}{|\mathcal{Y}_\xi|} \int_{\mathcal{Y}_\xi} \mathbb{C}(\mathbf{x})[\boldsymbol{\eta}_j + \boldsymbol{\varepsilon}(\mathbf{w}_{\xi,h,j})(\mathbf{x})] : \boldsymbol{\eta}_k \, d\mathbf{x} \right) \boldsymbol{\eta}_j \otimes \boldsymbol{\eta}_k.$$

Together, we obtain the following result.

Lemma 3.1

The macro-solution $\mathbf{u}_H \in V_H(\mathbf{u}_D)$ of the heterogeneous multiscale method minimizes the averaged energy

$$\mathcal{E}_H^{\text{avg}}(\mathbf{u}_H) = \frac{1}{2} \int_{\Xi_H} \mathbb{C}_{\xi,H}[\boldsymbol{\varepsilon}(\mathbf{u}_H)] : \boldsymbol{\varepsilon}(\mathbf{u}_H) - \langle \ell, \mathbf{u}_H \rangle. \quad (3.14)$$

The definition of the micro-fluctuations $\mathbf{w}_{\xi,h,1}, \dots, \mathbf{w}_{\xi,h,6}$ by equation (3.13) ensures that the two-scale elasticity tensor $\mathbb{C}_{\xi,H}$ is symmetric. Due to Korn's inequality the averaged energy $\mathcal{E}_H^{\text{avg}}(\cdot)$ is uniformly convex, which assures the existence and uniqueness of the minimizer in (3.14).

3.2.6 The parallel two-scale model

In our parallel model we assume that the meshes to resolve the geometry in the RVEs can be distributed to all processes. On the other hand, we do expect that we do not need to compute a micro-fluctuation in all RVEs \mathcal{Y}_ξ , e.g., if the microstructure is identical. In the most simple case of two-scale homogenization, we compute the micro-problem only once, as it is now described for our first parallel two-scale FEM of the heterogeneous small strain elasticity problem.

For the implementation, the RVEs $\mathcal{Y}_\xi = \xi + \delta(-0.5, 0.5)^D \subset \Omega$ are mapped to the unit cube $\mathcal{Y} = (0, 1)^3$. In the simple case the microstructure described by \mathbb{C} is mapped to the same tensor for all $\xi \in \Xi_H$. Since this cannot be expected for general applications, we describe the parallel algorithm in a more general case, which allows for different microstructures but which is also flexible for cases where only some of the RVE computations are required.

For the parallel realization, we use a load balancing procedure for determining a domain decomposition $\bar{\Omega} = \bar{\Omega}^1 \cup \dots \cup \bar{\Omega}^P$ and a further decomposition for the reference RVE $\bar{\mathcal{Y}} = \bar{\mathcal{Y}}^1 \cup \dots \cup \bar{\mathcal{Y}}^P$. With respect to these decompositions, we use the programming model for parallel finite elements described in [65]: the finite element spaces V_H and $V_{\xi,h}$ are distributed to the processes $p \in \mathcal{P} = \{1, \dots, P\}$ which results into a consistent representation of the macro-deformation \mathbf{u}_H and the micro-fluctuations $\mathbf{w}_{\xi,h,1}, \dots, \mathbf{w}_{\xi,h,6}$ by local functions $\mathbf{u}_H^p = \mathbf{u}_H|_{\bar{\Omega}^p}$ and $\mathbf{w}_{\xi,h,j}^p = \mathbf{w}_{\xi,h,j}|_{\bar{\mathcal{Y}}^p}$ on process p .

For the elastic two-scale solution the multiscale tensor $\mathbb{C}_{\xi,H}$ is evaluated only for a subset Ξ_H^{active} with different microstructure, i.e., we assume that for all other points $\xi \in \Xi_H \setminus \Xi_H^{\text{active}}$ some active point $\xi' \in \Xi_H^{\text{active}}$ exists so that we can choose $\mathbb{C}_{\xi,H} = \mathbb{C}_{\xi',H}$.

Together, we obtain the following algorithm:

E1) For all points $\xi \in \Xi_H^{\text{active}}$ with different microstructure perform the following steps sequentially:

M1) Compute the micro-fluctuations $\mathbf{w}_{\xi,h,1}, \dots, \mathbf{w}_{\xi,h,6} \in V_{\xi,h}$ by solving

$$\frac{1}{|\mathcal{Y}_\xi|} \int_{\mathcal{Y}_\xi} \mathbb{C}(\mathbf{x})[\boldsymbol{\eta}_l + \boldsymbol{\varepsilon}(\mathbf{w}_{\xi,h,l})] : \boldsymbol{\varepsilon}(\delta \mathbf{v}_{\xi,h}) \, d\mathbf{x} = 0, \quad \delta \mathbf{v}_{\xi,h} \in V_{\xi,h}$$

with a parallel multigrid method.

M2) Evaluate the local contributions of the multiscale tensor

$$\mathbb{C}_{\xi,H}^p = \sum_{l,j=1}^6 \left(\frac{1}{|\mathcal{Y}_\xi|} \int_{\mathcal{Y}_\xi} \mathbb{C}(\mathbf{x})[\boldsymbol{\eta}_l + \boldsymbol{\varepsilon}(\mathbf{w}_{\xi,h,l}^p)] : \boldsymbol{\eta}_j \, d\mathbf{x} \right) \boldsymbol{\eta}_l \otimes \boldsymbol{\eta}_j, \quad p \in \mathcal{P}.$$

M3) On the process q with $\xi \in \Xi_H \cap \Omega^q$ collect the full multiscale tensor

$$\mathbb{C}_{\xi,H} = \sum_{p=1}^P \mathbb{C}_{\xi,H}^p.$$

E2) For all points $\xi \in \Xi_H \setminus \Xi_H^{\text{active}} \cap \Omega^p$ sequentially find $\xi' \in \Xi_H^{\text{active}}$ with $\mathbb{C}_{\xi,H} = \mathbb{C}_{\xi',H}$ and send the multiscale tensor to process p .

E3) Compute $\mathbf{u}_H \in V_H(\mathbf{u}_D)$ by solving

$$\int_{\Xi_H} \mathbb{C}_{\xi,H}[\boldsymbol{\varepsilon}(\mathbf{u}_H)] : \boldsymbol{\varepsilon}(\delta \mathbf{u}_H) = \langle \ell, \delta \mathbf{u}_H \rangle, \quad \delta \mathbf{u}_H \in V_H(0)$$

with a parallel multigrid method.

This applies in particular to materials described only by a single or a small number of characteristic microstructures. Moreover, this procedure easily extends to the case where the microstructure only changes by its orientation. Then, the multiscale tensor is also computed only once, distributed to all processes, and is then locally rotated with respect to the prescribed orientation of the RVE \mathcal{Y}_ξ .

Chapter 4

Numerical experiments for linear elastic two-scale models

After a brief introduction into uniaxial tensile testing in material science, experiments for the linear incremental two-scale material model are considered. First, we examine an investigation of the convergence behavior for the linear FE² method for various scales of heterogeneities on the micro-scale. After that we study the linear material behavior in a series of experiments for different fiber orientations and filler contents.

All the two-scale simulations have been implemented using the parallel finite element software M++ [65]. For efficiency reasons, a multigrid method with a V-cycle is used on both scales. It includes a highly scalable periodic parallel direct coarse grid solver with a Gauss-Seidel smoother as described in [35].

4.1 The experimental setting

Sophisticated materials are becoming increasingly important in the area of engineering and consumer applications. More and more conventional, unreinforced polymers and even metals become replaced by composite materials. This contribution is focused on two component composites with a thermoplastic engineering polymer as carrier matrix with firmly embedded glass fiber. As thermoplastic material, we consider *polybutylene terephthalate* (PBT) for the carrier matrix.

4.1.1 Tensile testing

A very basic concept for quality inspection in material science are standardized uniaxial tensile tests. In combination with optical measuring instruments and applying a controlled monotonic loading, material specific properties can be measured for selecting

and designing materials in engineering applications [51, 14]. Tensile testing machines are used, among other things for creating stress-strain curves through recording the applied traction with respect to the changes of the sprayed pattern within a centered region of the mounted test bar, see Figure 4.1. A further application field is the detection of a material's orientation dependencies due to the fiber reinforcement. For the test bar, a standardized specimen geometry DIN EN ISO 527-2 type 1A [25] is used, which is shown in Figure 4.1. The specimen has two shoulders and a reduced section in between. In order to guarantee that the failure will occur within the reduced section under an applied force, the reduced section is manufactured to be smaller than the enlarged shoulders. For a secure mounting of the specimen into the tensile testing machine the shoulders are gripped customarily.

In material science different types of tensile test are used. Monotonic uniaxial material tests are used to determine the yield strength, the elastic yield limit and other properties of a material. On the other hand uniaxial cyclic tensile tests are of great interest for determining the durability in material and failure analysis in order to simulate the long term endurance of permanent use. In these test sequences the specimen is repeatedly stretched and squeezed. After each complete unloading, the specimen undergoes a load in the opposite direction of the unloading. This allows observing further material specific dependencies.



Figure 4.1: Test bar of type 1A with spray patterns for the evaluation of material specific properties via optical measuring instruments.

4.1.2 Materialography

Since the mechanical properties of glass and thermoplastic differs by order of magnitudes, the combination of a polymer with glass fibers through the injection molding process leads to a composite with completely new features. A decisive influence on the newly grained features has the fiber distribution within the carrier matrix. Thus, the insight of the manufacturing process for a directly injected specimen is indispensable. The intruding of the melt through the gate into the mold cavity originates in thickness direction of the component a streaming and velocity profile, respectively. During this process, the melt front experiences an elongation transversal to the velocity of propagation and the fibers become aligned rectangular to the flow direction. On the other

hand, the melt volume gets turned around at the melt front through the adhesion at the cool wall. During this process, the velocity goes to zero and the melt is subjected to a shear, so thus the glass fiber gets aligned into the flow direction. Roughly speaking, the composition of a short fiber-reinforced material is structured in three different layers due to elongations and shears. In the shear layer at the boundary in the specimen the fibers are orientated in flow direction and in the mid layer they are aligned transversal to the flow direction. On the right hand side in Figure 4.2, this effect is illustrated by the cross sectional materialographic of a specimen type 1A with a fiber weight content of 30%. Such a specimen has a very small mid layer and is decisively dominated by the parallel aligned fiber orientation to the flow direction. However, such a fiber distribution even occurs for a polymer with minimum 10% fiber weight content. This effect is shown on the left hand side in Figure 4.2, by the materialographic of the cross sectional area for a polymer with 5% fiber weight content. It has an almost homogeneous fiber distribution aligned transversely with respect to the flow direction. The manufacturing process of an injection molded thin plate exhibit the same materialographic behavior like the directly injected specimen. These plates are used to examine the material behavior for various fiber orientations. For this purpose, specimens with different angles to the flow direction are milled out.

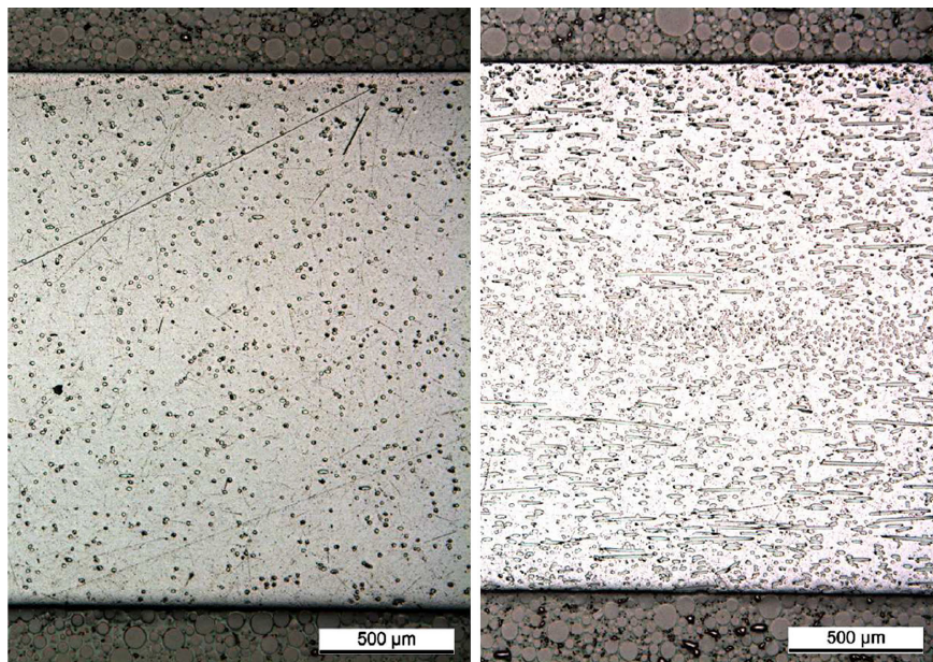


Figure 4.2: Microstructure for a test bar type 1A with 5% (left) and 30% (right) fiber weight content. Illustration from [51, Chap. 1, Fig. 1].

4.2 Numerical setting

We evaluate the two-scale method for two component composites with the thermoplastic polymer PBT as carrier matrix and embedded glass fibers, cf. Figure 4.3. We use isotropic linear elasticity with Lamé parameters $\lambda_M = 3571.43$ and $\mu_M = 892.857$ for the polymer¹ and $\lambda_F = 30000$ and $\mu_F = 20000$ for the glass fiber².

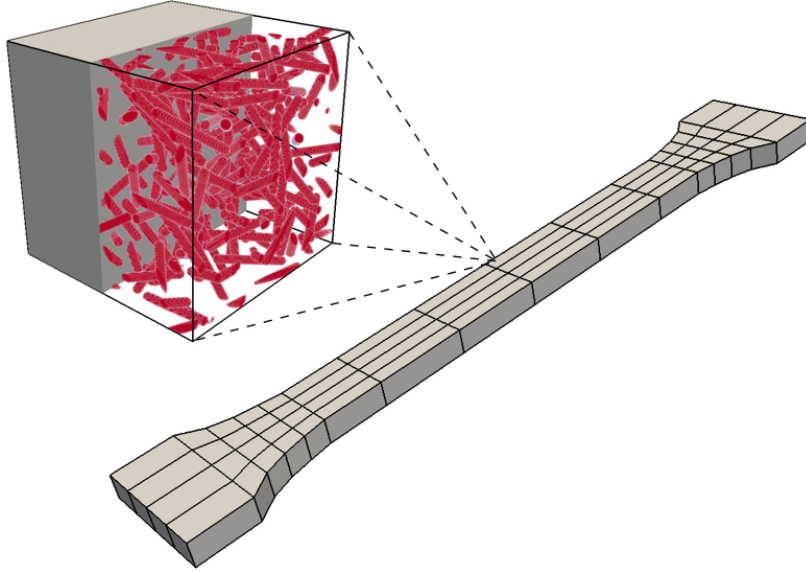


Figure 4.3: *Illustration of the two-scale model. The macroscopic test bar Ω has an isotropic short fiber-reinforced microstructure (here with 10% volume fraction) in the RVEs \mathcal{Y}_ξ .*

For the test scenario we use a standardized uniaxial tensile test configuration with a specimen ISO 527-2 type 1A. The computational domain $\Omega \subset (-0.2, 0.2) \times (-2, 2) \times (-6.5, 6.5)$ is approximated by a hexahedral mesh, cf. Figure 4.4, where the shoulders of the specimen are shortened in the length, corresponding to the area mounted into the tensile testing machine. On the boundary $\Gamma_D \cup \Gamma_N = \partial\Omega$ with $\Gamma_D = \{\mathbf{x} \in \partial\Omega : x_3 = -6.5 \text{ or } x_3 = 6.5\}$ and $\Gamma_N = \partial\Omega \setminus \Gamma_D$, we use at the end of the specimen an one sided displacement driven load as acting force which is described by

$$\mathbf{u}_D(t, \mathbf{x}) = \begin{pmatrix} 0 \\ 0 \\ u_0 t \end{pmatrix} \quad \text{for } x_3 = 6.5, \quad (4.1a)$$

$$\mathbf{u}_D(t, \mathbf{x}) = \mathbf{0} \quad \text{for } x_3 = -6.5, \quad (4.1b)$$

$$\boldsymbol{\sigma}(\boldsymbol{\varepsilon}(\mathbf{u}(t, \mathbf{x})))\mathbf{n} = \mathbf{0} \quad \text{for } \mathbf{x} \in \Gamma_N. \quad (4.1c)$$

¹ BASF data sheet on <http://www.plasticsportal.net>

² Data sheet on <http://www.matweb.com>

The scaling factor is set to $u_0 = 0.01$ and the linear model is tested for a time parameter $t = 1$. For the investigation of the convergence properties, we use one fourth of the geometry $\Omega_{\text{sym}} \subset (-0.2, 0.2) \times (0, 2) \times (0, 6.5) \subset \Omega$ and we use symmetry boundary conditions on $\Gamma_{\text{sym}} = \{\mathbf{x} \in \partial\Omega_{\text{sym}} : x_3 = 0 \text{ or } x_2 = 0\}$ corresponding to a two sided loading which is defined by (4.1a) and (4.1c).

In V_H and $V_{\xi,h}$ we use conforming hexahedral \mathbb{Q}_1 finite elements. The space \mathbb{Q}_1 denotes all polynomials of degree less than or equal to 1 in each variable on each cell.

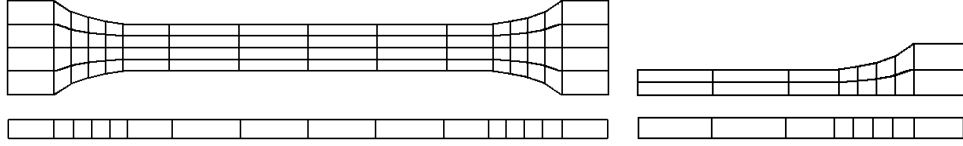


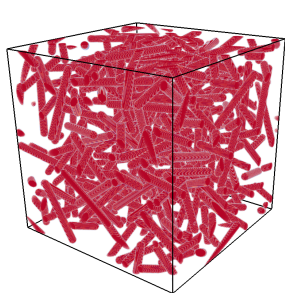
Figure 4.4: Approximation on the coarse scale of the geometry of the standardized specimen ISO 527-2:1996 type 1A with 20mm shortened shoulders and reduction to one fourth.

4.3 Numerical convergence analysis

In our first experiment, the convergence of the classical two-scale homogenization for various resolutions of the microstructure in the RVE is tested. Because we use the same microstructure in every RVE, the effective material response is only once computed and used at all integration points. Within the RVE we extract various length scales of a complex microstructure. Each extraction corresponds to one eighth of its previously microstructure by employing a bisection method and is mapped to the unite cube. This preserves the ratio of volume fraction, fiber length and thickness. We emphasize the scale of heterogeneity by $\delta/2^n$ and each RVE which is linked with this scale by $\mathcal{Y}_\xi^{\delta/2^n}$. For the investigation of the convergence properties we consider the macro-stress in the Frobenius-norm $\sigma_{H,h}^{\delta/2^n} = \|\sigma_{H,h}^{\delta/2^n}\|_F$ for uniform mesh refinements on the macro and micro-scale, where the macro-stress $\sigma_{H,h}^{\delta/2^n} = \int_{\Xi_H} \sigma_{\xi,H}^{\delta/2^n}$ is defined at each integration point by the averaged micro-stress $\sigma_{\xi,H}^{\delta/2^n} = \frac{1}{|\mathcal{Y}_\xi^{\delta/2^n}|} \int_{\mathcal{Y}_\xi^{\delta/2^n}} \mathbb{C}(\mathbf{x})[\varepsilon_{\xi,H} + \varepsilon(\mathbf{v}_{\xi,h})] d\mathbf{x}$.

Results of the convergence analysis for the numerically determined value $\sigma_{H,h}^{\delta/2^n}$ in Table 4.1, 4.2 and 4.3 confirm the apprehension that the total error of the elastic two-scale method is dominated by the error on the micro-scale and therefore that it is strongly linked to the varying material phases in the microstructure.

In Figure 4.5, 4.7 and 4.9 we can see the stress-states $\sigma_{\xi,h}^{\delta/2^n}(\mathbf{w}_{\xi,h,k}^{\delta/2^n})$ with respect to the deformation corresponding to the 6 micro-fluctuations $\mathbf{w}_{\xi,h,k}^{\delta/2^n}$ for a microstructure $\mathcal{Y}_\xi^{\delta/2^n}$ with a scale of heterogeneity $\delta/2^n$ as shown in Table 4.1, 4.2 and 4.3.



DoFs	765	4 455	29 835	217 107	1 653 795
375	9.85312	9.81881	9.80574	9.80098	9.79927
2 187	8.63429	8.59902	8.58547	8.58050	8.57870
14 739	7.81376	7.77798	7.76413	7.75904	7.75720
107 811	5.83399	5.79482	5.77930	5.77350	5.77139
823 875	4.97443	4.93357	4.91718	4.91102	4.90876
6 440 067	4.60743	4.56594	4.54920	4.54287	4.54056
50 923 779	4.38415	4.34254	4.32568	4.31931	4.31697

Table 4.1: Left: Isotropic microstructure with 10% fiber volume fraction in every RVE \mathcal{Y}_ξ^δ . Right: Numerical results of $\sigma_{H,h}^\delta$ in V_H on the macro-scale (row) and in $V_{\xi,h}$ on the micro-scale (column) for the classical two-scale homogenization in elasticity.

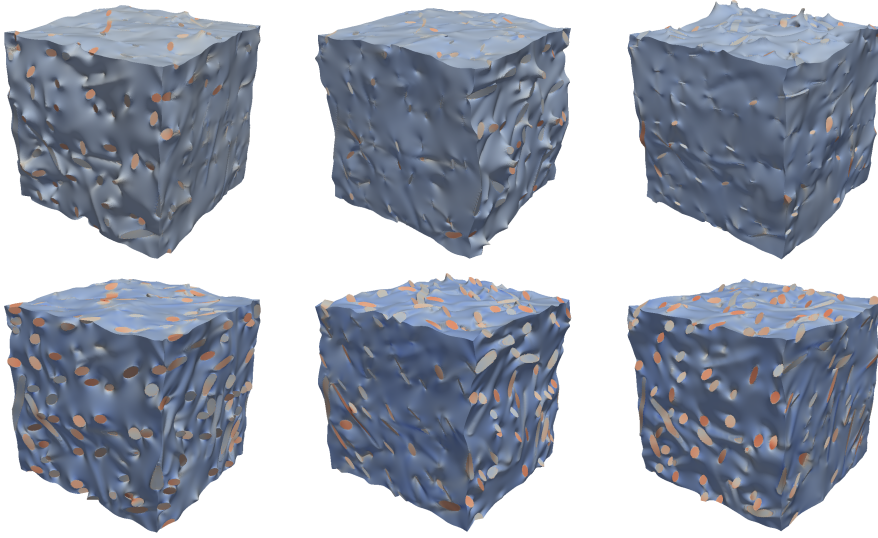


Figure 4.5: Stress states $\sigma_{\xi,h}^\delta(\mathbf{w}_{\xi,h,k}^\delta)$ with respect to the deformation of the 6 micro-fluctuations $\mathbf{w}_{\xi,h,k}^\delta$ in $V_{\xi,h} \subset H_{per}^1(\mathcal{Y}_\xi^\delta, \mathbb{R}^D)$ corresponding to the 6 basis tensors $\boldsymbol{\eta}_k$ in $\text{Sym}(3)$ (increasing values from blue to red).

$$\mathbb{C}_{\xi,H}^\delta = \begin{pmatrix} 6813.80 & 4103.21 & 4091.94 & -31.98 & -1.78 & -30.04 \\ 4103.21 & 6746.60 & 4090.62 & -1.78 & 26.43 & -3.04 \\ 4091.94 & 4090.62 & 6750.23 & 9.39 & 2.72 & -22.82 \\ -31.98 & -1.78 & 9.39 & 2630.59 & -7.91 & -1.96 \\ -1.78 & 26.43 & 2.72 & -7.91 & 2598.52 & 10.04 \\ -30.04 & -3.04 & 22.82 & -1.96 & 10.04 & 2597.09 \end{pmatrix}$$

Figure 4.6: Elastic two-scale tensor $\mathbb{C}_{\xi,H}^\delta$ of the convergence analysis for an isotropic short fiber-reinforced microstructure with 10% fiber volume fraction and a characteristic length scale δ in every RVE \mathcal{Y}_ξ^δ .

DoFs	765	4 455	29 835	217 107	1 653 795
375	7.56932	7.53591	7.52304	7.51833	7.51663
2 187	7.97383	7.93835	7.92463	7.91960	7.91778
14 739	5.96454	5.92619	5.91105	5.90543	5.90339
107 811	5.06637	5.02650	5.01055	5.00456	5.00239
823 875	4.68158	4.64109	4.62479	4.61865	4.61641
6 440 067	4.50784	4.46708	4.45061	4.44440	4.44214
50 923 779	4.38927	4.34845	4.33192	4.32568	4.32341

Table 4.2: Left: Isotropic microstructure with 10% fiber volume fraction in every RVE $\mathcal{Y}_\xi^{\delta/2}$. Right: Numerical results of $\sigma_{H,h}^{\delta/2}$ in V_H on the macro-scale (row) and in $V_{\xi,h}$ on the micro-scale (column) for the classical two-scale homogenization in elasticity.

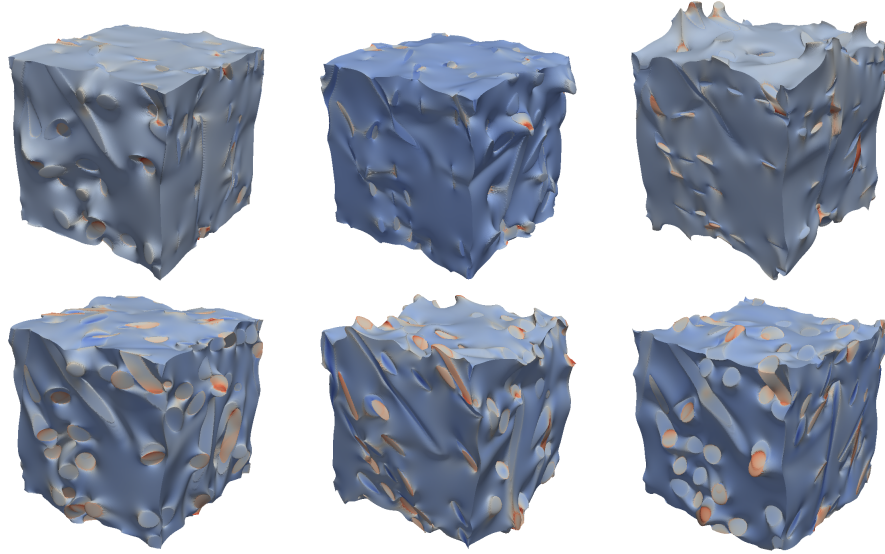
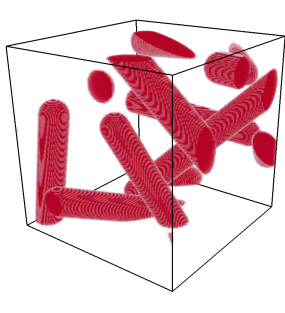


Figure 4.7: Stress states $\sigma_{\xi,h}^{\delta/2}(\mathbf{w}_{\xi,h,k}^{\delta/2})$ with respect to the deformation of the 6 micro-fluctuations $\mathbf{w}_{\xi,h,k}^{\delta/2}$ in $V_{\xi,h} \subset H_{per}^1(\mathcal{Y}_\xi^{\delta/2}, \mathbb{R}^D)$ corresponding to the 6 basis tensors $\boldsymbol{\eta}_k$ in $\text{Sym}(3)$ (increasing values from blue to red).

$$\mathbb{C}_{\xi,H}^{\delta/2} = \begin{pmatrix} 6617.51 & 4083.62 & 3999.64 & -4.18 & -9.59 & 20.36 \\ 4083.62 & 6601.07 & 4036.44 & 49.80 & -80.31 & -0.16 \\ 3999.64 & 4036.44 & 6705.41 & 25.44 & -52.32 & -23.35 \\ -4.18 & 49.80 & 25.44 & 2558.39 & -13.07 & -18.14 \\ -9.59 & -80.31 & -52.32 & -13.07 & 2474.23 & 20.77 \\ 20.36 & -0.16 & -23.35 & -18.14 & 20.77 & 2388.42 \end{pmatrix}$$

Figure 4.8: Elastic two-scale tensor $\mathbb{C}_{\xi,H}^{\delta/2}$ of the convergence analysis for an isotropic short fiber-reinforced microstructure with 10% fiber volume fraction and a characteristic length scale $\delta/2$ in every RVE $\mathcal{Y}_\xi^{\delta/2}$.



DoFs	765	4 455	29 835	217 107	1 653 795
375	7.16115	7.12588	7.11215	7.10708	7.10525
2 187	5.52903	5.49100	5.47591	5.47028	5.46823
14 739	4.66845	4.62866	4.61271	4.60672	4.60454
107 811	4.29373	4.25314	4.23677	4.23059	4.22834
823 875	4.14409	4.10322	4.08669	4.08044	4.07816
6 440 067	4.04104	4.00008	3.98348	3.97720	3.97491
50 923 779	3.99777	3.95676	3.94012	3.93383	3.93153

Table 4.3: Left: Isotropic microstructure with 10% fiber volume fraction in every RVE $\mathcal{Y}_\xi^{\delta/4}$. Right: Numerical results of $\sigma_{H,h}^{\delta/4}$ in V_H on the macro-scale (row) and in $V_{\xi,h}$ on the micro-scale (column) for the classical two-scale homogenization in elasticity.

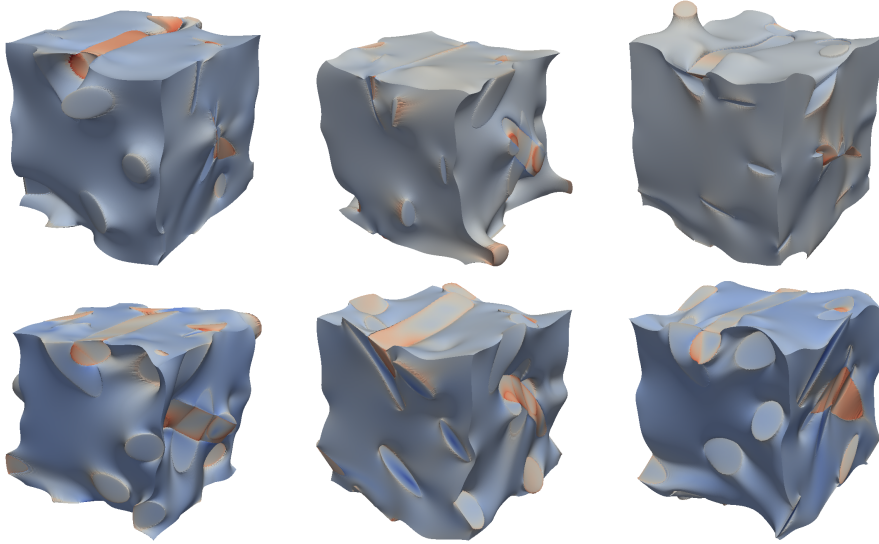


Figure 4.9: Stress states $\sigma_{\xi,h}^{\delta/4}(\mathbf{w}_{\xi,h,k}^{\delta/4})$ with respect to the deformation of the 6 micro-fluctuations $\mathbf{w}_{\xi,h,k}^{\delta/4}$ in $V_{\xi,h} \subset H_{per}^1(\mathcal{Y}_\xi^{\delta/4}, \mathbb{R}^D)$ corresponding to the 6 basis tensors $\boldsymbol{\eta}_k$ in $\text{Sym}(3)$ (increasing values from blue to red).

$$\mathbb{C}_{\xi,H}^{\delta/4} = \begin{pmatrix} 6822.72 & 4057.25 & 3966.77 & -39.89 & 25.10 & -75.43 \\ 4057.25 & 6614.21 & 3968.56 & -87.04 & -54.28 & -91.65 \\ 3966.77 & 3968.56 & 6277.37 & 22.82 & -61.34 & -73.23 \\ -39.89 & -87.04 & 22.82 & 2547.21 & -131.88 & 22.10 \\ 25.10 & -54.28 & -61.34 & -131.88 & 2316.83 & 25.30 \\ -75.43 & -91.65 & -73.23 & 22.10 & 25.30 & 2367.72 \end{pmatrix}$$

Figure 4.10: Elastic two-scale tensor $\mathbb{C}_{\xi,H}^{\delta/4}$ of the convergence analysis for an isotropic short fiber-reinforced microstructure with 10% fiber volume fraction and a characteristic length scale $\delta/4$ in every RVE $\mathcal{Y}_\xi^{\delta/4}$.

To enable a qualitative statement about the accuracy for the classical elastic two-scale homogenization method, we investigate the asymptotic behavior for $h \rightarrow 0$ through an expansion of an extrapolation. Therefore, we compute a sequence of solutions $\sigma_{H,h}^{\delta/2^n}$, $\sigma_{H,h/2}^{\delta/2^n}$, $\sigma_{H,h/4}^{\delta/2^n}$, $\sigma_{H,h/8}^{\delta/2^n}$, ... with uniform mesh refinements on the micro-scale. The assumption that the error behaves asymptotically like

$$\sigma_{H,2h}^{\delta/2^n} - \sigma_{H,h}^{\delta/2^n} = Ch^p + O(h^{p+1}) \quad (4.2)$$

with constants $C, p > 0$, defines the experimental order of convergence

$$p \approx \log_2 \frac{\sigma_{H,2h}^{\delta/2^n} - \sigma_{H,h}^{\delta/2^n}}{\sigma_{H,h}^{\delta/2^n} - \sigma_{H,h/2}^{\delta/2^n}}, \quad (4.3)$$

and we obtain $\sigma_{H,h}^{\delta/2^n} - \sigma_{H,h/2}^{\delta/2^n} = 2^{-p} (\sigma_{H,2h}^{\delta/2^n} - \sigma_{H,h}^{\delta/2^n}) + O(h^{p+1})$. Then, from

$$\begin{aligned} \lim_{k \rightarrow \infty} \sigma_{H,h/2^k}^{\delta/2^n} &= \sigma_{H,h}^{\delta/2^n} - \sum_{k=1}^{\infty} (\sigma_{H,h/2^{k+1}}^{\delta/2^n} - \sigma_{H,h/2^{k+2}}^{\delta/2^n}) \\ &\approx \sigma_{H,h}^{\delta/2^n} - (\sigma_{H,2h}^{\delta/2^n} - \sigma_{H,h}^{\delta/2^n}) \sum_{k=1}^{\infty} 2^{-kp} \end{aligned}$$

we derive the expression for the extrapolated value

$$\sigma_{H,\text{ex}_h}^{\delta/2^n} = \sigma_{H,h}^{\delta/2^n} - \frac{\sigma_{H,2h}^{\delta/2^n} - \sigma_{H,h}^{\delta/2^n}}{2^p - 1}. \quad (4.4)$$

With the expression of the extrapolated value (4.4) the relative error for a mesh refinement in h respective to the heterogeneity length scale $\delta/2^n$ can be determined by

$$e_{H,\text{rel}_h}^{\delta/2^n} = \frac{|\sigma_{H,h}^{\delta/2^n} - \sigma_{H,\text{ex}_h}^{\delta/2^n}|}{\sigma_{H,\text{ex}_h}^{\delta/2^n}}. \quad (4.5)$$

Analogously, we define for a computed sequence of solutions $\sigma_{H,h}^{\delta/2^n}$, $\sigma_{H/2,h}^{\delta/2^n}$, $\sigma_{H/4,h}^{\delta/2^n}$, $\sigma_{H/8,h}^{\delta/2^n}$, ... with respect to a uniform mesh refinement on the macro-scale and an RVE with a scale of heterogeneity $\delta/2^n$, the extrapolated value $\sigma_{\text{ex}_H,h}^{\delta/2^n}$ in the same way as on the micro-scale, which determines the relative error $e_{\text{rel}_H,h}^{\delta/2^n}$.

From Table 4.1, 4.2 and 4.3 we observe that the results of the numerical error on the micro-scale $\sigma_{H,h}^{\delta/2^n} - \sigma_{H,h/2}^{\delta/2^n}$ and on the macro-scale $\sigma_{H,h}^{\delta/2^n} - \sigma_{H/2,h}^{\delta/2^n}$ behaves asymptotically similar for each fixed resolution on the macro-scale and the micro-scale, respectively. Therefore, it is sufficient to consider for the investigation on the micro-scale a fixed resolution $\dim V_H = 1\,653\,795$ for the macro-scale and for the investigation on the macro-scale a fixed resolution $\dim V_{\xi,h} = 50\,923\,779$ for the micro-scale.

Figure 4.11 shows a double logarithmic scale plot of the numerically determined error $e_h^{\delta/2^n} = \sigma_{H,h}^{\delta/2^n} - \sigma_{H,\text{ex}_h}^{\delta/2^n}$ on the micro-scale against the micro grid size h on the left hand side and the error $e_H^{\delta/2^n} = \sigma_{H,h}^{\delta/2^n} - \sigma_{\text{ex}_{H,h}}^{\delta/2^n}$ on the macro-scale against the macro grid size H on the right hand side. The better the microstructure is sampled by some quadrature rule the better converges the two-scale method. We observe the same effect for a larger scale of the heterogeneity for the representation of the RVE on the micro-scale. For the convergence on the macro-scale one can say that it is independent of the choice of the scale of the heterogeneity, but with the addition that this affects the result with regard to the modeling error, see [64]. Table 4.6 lists the relative errors $e_{H,\text{rel}_h}^{\delta/2^n}$ corresponding to the extrapolated values $\sigma_{H,\text{ex}_h}^\delta = 4.10819$, $\sigma_{H,\text{ex}_h}^{\delta/2} = 4.21254$ and $\sigma_{H,\text{ex}_h}^{\delta/4} = 3.89088$ on the micro-scale or rather in Table 4.7 the relative errors $e_{\text{rel}_{H,h}}^{\delta/2^n}$ corresponding to the extrapolated values $\sigma_{\text{ex}_{H,h}}^\delta = 4.31538$, $\sigma_{\text{ex}_{H,h}}^{\delta/2} = 4.32179$ and $\sigma_{\text{ex}_{H,h}}^{\delta/4} = 3.92995$ on the macro-scale which underlines the conclusions of the above. For the evaluation of the extrapolated values $\sigma_{H,\text{ex}_h}^{\delta/2^n}$ and $\sigma_{\text{ex}_{H,h}}^{\delta/2^n}$ we used the mean value for all determined experimental orders of convergence (4.3) within the asymptotic area of convergence. To get back to Figure 4.11, we get out of the double logarithmic scale plot the asymptotic rate of convergence as the slope evaluated between the errors in relation to the grid size. Here, we observe for all heterogeneity scales $\delta/2^n$ an almost linear convergence behavior on the micro-scale. On the other hand, for uniform mesh refinements on the macro-scale to a fixed resolution on the micro-scale the asymptotic rate of convergence behaves approximately linear with values between 1.30 and 1.40. One can see that the asymptotic area of convergence shifts for a larger scale of heterogeneity to a finer discretization which is due to the fact that the applied quadrature rule subsamples the highly oscillating material phases in the RVE, see Table 4.6 and the plot on the left hand side in Figure 4.11.

The corresponding upscaled linear elastic two-scale material response $\mathbb{C}_{\xi,H}^{\delta/2^n}$ evaluated by the 6 micro-fluctuations $\mathbf{w}_{\xi,h,k}^{\delta/2^n}$ is represented in Figure 4.6, 4.8 and 4.10. Each elastic material response shows an approximately isotropic material behavior, cf. Section 2.3.2.

Attributable to the superposition of the error respective to the geometry and the linear approximation in each cell it is mentioned that the results for the convergence behavior are only asymptotically. All the computations for the convergence investigation were performed on a single node with 64 cores of the DELTA B.1 cluster.

DoFs	2 187	14 739	107 811	823 875	6 440 067
δ			1.20291	1.22825	0.71963
$\delta/2$		1.16074	1.22300	1.14720	0.55364
$\delta/4$	0.92249	1.19901	1.32481	0.54055	1.25103

Table 4.4: Experimental order of convergence p in (4.3) for uniform mesh refinements on the micro-scale for a fixed macro-scale discretization with $\dim V_H = 1\,653\,795$ corresponding to various scales of heterogeneities $\delta/2^n$ for $n \in \{0, 1, 2\}$.

DoFs	4 455	29 835	217 107
δ	1.30333	1.40424	1.44478
$\delta/2$	1.30419	1.40547	1.45885
$\delta/4$	1.30132	1.40352	1.45143

Table 4.5: Experimental order of convergence p like in (4.3) but for uniform mesh refinements on the macro-scale for a fixed micro-scale discretization with $\dim V_{\xi,h} = 50\,923\,779$ corresponding to various scales of heterogeneities $\delta/2^n$ for $n \in \{0, 1, 2\}$.

DoFs	375	2 187	14 739	107 811	823 875	6 440 067	50 923 779
$e_{H,\text{rel}_h}^\delta$	138.53	108.82	88.82	40.49	19.49	10.52	5.08
$e_{H,\text{rel}_h}^{\delta/2}$	78.43	87.96	40.14	18.75	9.59	5.45	2.63
$e_{H,\text{rel}_h}^{\delta/4}$	82.61	40.54	18.34	8.67	4.81	2.16	1.04

Table 4.6: Relative error $e_{H,\text{rel}_h}^{\delta/2^n}$ in (4.5) in percentage for uniform mesh refinements on the micro-scale for a fixed macro-scale discretization with $\dim V_H = 1\,653\,795$ corresponding to various scales of heterogeneities $\delta/2^n$ for $n \in \{0, 1, 2\}$.

DoFs	765	4 455	29 835	217 107	1 653 795
$e_{\text{rel}_H,h}^\delta$	1.59	0.63	0.24	0.09	0.04
$e_{\text{rel}_H,h}^{\delta/2}$	1.56	0.62	0.23	0.09	0.04
$e_{\text{rel}_H,h}^{\delta/4}$	1.73	0.68	0.26	0.10	0.04

Table 4.7: Relative error $e_{\text{rel}_H,h}^{\delta/2^n}$ in (4.5) in percentage for uniform mesh refinements on the macro-scale for a fixed discretization on the micro-scale with $\dim V_{\xi,h} = 50\,923\,779$ corresponding to various scales of heterogeneities $\delta/2^n$ for $n \in \{0, 1, 2\}$.

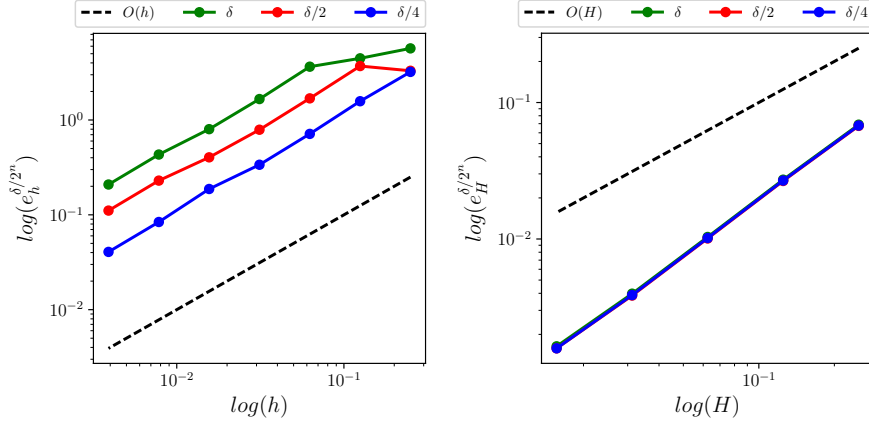


Figure 4.11: Asymptotic rate of convergence for various scales of heterogeneities $\delta/2^n$ for $n \in \{0, 1, 2\}$ on the micro-scale (left) and macro-scale (right) for uniform mesh refinements. The dashed lines $O(h)$ and $O(H)$ indicate the slope of a linear rate on the micro-scale and macro-scale, respectively.

4.4 Experiments for various fiber orientations and filler contents

The following experiment compares the material specific properties of a monotonic uniaxial tensile test for the linear elastic material behavior for a microstructure with 10%, 20% and 30% fiber volume fraction and 0° , 45° , 60° and 90° fiber orientation. In each numerical simulation we use a fine discretization with $\dim V_{\xi,h} = 6\,440\,067$ for the computation of the elastic material response $\mathbb{C}_{\xi,H}$ in every RVE and $\dim V_H = 6\,551\,523$ for the representation of the macro-solution \mathbf{u}_H . Because we use the same microstructure in every RVE, the effective material response is only once computed and used at each integration point. Each computation was performed on a single node of the DELTA B.1 cluster using 64 cores for approximately one hour.

Within a centered region $\Omega_{\text{ctr}} = (-0.2, 0.2) \times (0, 1) \times (0, 2) \subset \Omega$, the stress and strain in tensile direction are numerically computed by

$$\sigma_z = \frac{1}{|\Omega_{\text{ctr}}|} \int_{\Xi_H \cap \Omega_{\text{ctr}}} (\mathbb{C}_{\xi,H}[\boldsymbol{\varepsilon}(\mathbf{u}_H)])_{zz} \quad \text{and} \quad \varepsilon_z = \frac{1}{|\Omega_{\text{ctr}}|} \int_{\Xi_H \cap \Omega_{\text{ctr}}} (\boldsymbol{\varepsilon}(\mathbf{u}_H))_{zz}$$

to approximate Young's modulus $E_z = \frac{\sigma_z}{\varepsilon_z}$. Analogously, the strain averages ε_x and ε_y are defined to determine Poisson's ratio $\nu_{zx} = -\frac{\varepsilon_x}{\varepsilon_z}$ and $\nu_{zy} = -\frac{\varepsilon_y}{\varepsilon_z}$.

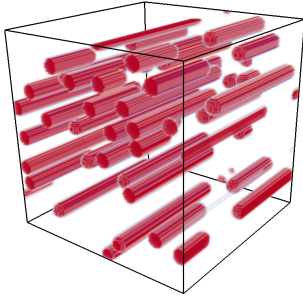
Young's modulus: The investigation of Young's modulus E_z shows for a fixed fiber filler content the most stiffest material behavior for a parallel aligned fiber and

load direction, cf. Table 4.8. All other fiber orientations have a nearly equal stiffness character. From this it can be inferred, that for a fiber orientation of 0° to tensile direction the mechanical properties of the fibers dominate. Otherwise, the mechanical properties of the carrier matrix dominate for all different fiber orientations. If the situation is regarded for fixed fiber orientations, then we observe for a rising fiber filler content an increase in stiffness due to the mechanical properties of the reinforcement by the fibers. However, the overall most stiffest behavior for a short fiber-reinforced composite is achieved for the highest fiber filler content and a parallel aligned fiber orientation to the acting force.

Anisotropy: For the investigation of the isotropy we compare in the plane rectangular to the applied force, the transversal Poisson's ratio ν_{zx} and ν_{zy} , see Table 4.8. In the case of parallel fiber and tensile alignment we observe very accurate transverse isotropy, i.e. $\nu_{zx} = \nu_{zy}$. This corresponds to the symmetry of the rotational axis along the fiber direction. For each different fiber alignment to the acting force the material behaves strongly anisotropic. In Figure 4.12, this effect can be verified for a short fiber-reinforced composite with 10% fiber volume fraction by the symmetry planes of the elastic two-scale tensor, see Section 2.3.2. The two-scale tensor for a parallel fiber tensile alignment has a transversal isotropic material response. For each fiber orientation of 45° , 60° and 90° the elastic two-scale tensor shows a strong anisotropic behavior.

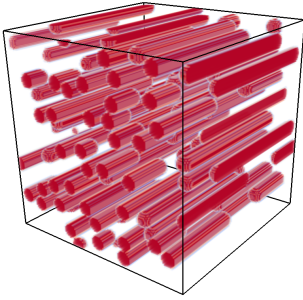
Specimen: Figure 4.13 shows the stress states of a short fiber-reinforced specimen with 10% fiber volume filler content for 0° , 45° , 60° and 90° fiber orientation to the applied force. Within the reduced section we observe the highest stress values. At the end of the reduced section we recognize stress peaks which are probably caused by the coarse hexahedral mesh approximation, see Figure 4.4.

Conclusions: Comparing with experimental data [51] we observe that the results fit well. For a directly extruded specimen of type 1A with parallel aligned load fiber orientation and fiber volume content of 11.3% a Young's modulus of $E_z^{0^\circ} = 5\,960$ and for 17.9% a modulus of $E_z^{0^\circ} = 8\,240$ is measured, see [51, Chap. 2.3, Tab. 1]. For fiber orientations with angle 0° , 45° , 60° and 90° measurements of Young's modulus of a specimen type 5A was personally communicated by C. Röhrig at the MuSiKo workshop in February 2016 as the secant for the increasing stress from 0 to 1% nominal strain of the stress-strain curves in [51, Chap. 2.3, Fig. 10] and gives $E_z^{0^\circ} = 6\,050$, $E_z^{45^\circ} = 4\,300$, $E_z^{60^\circ} = 3\,485$ and $E_z^{90^\circ} = 3\,840$ for a volume filler content of 11.3% and $E_z^{0^\circ} = 7\,910$, $E_z^{45^\circ} = 4\,500$, $E_z^{60^\circ} = 4\,550$ and $E_z^{90^\circ} = 4\,430$ for 17.3% fiber volume content.



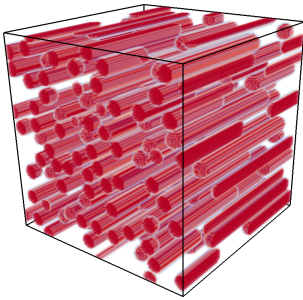
	PBT	0°	45°	60°	90°
E_z	2 500	6 116	3 333	3 167	3 338
ν_{zy}	0.40	0.38	0.44	0.36	0.21
ν_{zx}	0.40	0.38	0.36	0.41	0.51
σ_z	2.19371	5.30179	2.94166	2.78511	2.91609
ε_x	-3.50e-4	-3.32e-4	-3.15e-4	-3.56e-4	-4.47e-4
ε_y	-3.50e-4	-3.33e-4	-3.86e-4	-3.20e-4	-1.83e-4
ε_z	8.77e-4	8.66e-4	8.82e-4	8.79e-4	8.73e-4

(a) volume filler content 10%



	PBT	0°	45°	60°	90°
E_z	2 500	10 229	4 460	4 257	4 440
ν_{zy}	0.40	0.37	0.44	0.33	0.16
ν_{zx}	0.40	0.36	0.33	0.40	0.51
σ_z	2.19371	8.82239	3.94199	3.74542	3.8748
ε_x	-3.50e-4	-3.09e-4	-2.93e-4	-3.53e-4	-4.44e-4
ε_y	-3.50e-4	-3.19e-4	-3.89e-4	-2.92e-4	-1.40e-4
ε_z	8.77e-4	8.62e-4	8.83e-4	8.79e-4	8.72e-4

(b) volume filler content 20%



	PBT	0°	45°	60°	90°
E_z	2 500	15 443	6 621	6 032	5 973
ν_{zy}	0.40	0.34	0.39	0.31	0.13
ν_{zx}	0.40	0.34	0.33	0.38	0.50
σ_z	2.19371	13.293	5.83694	5.30212	5.21301
ε_x	-3.50e-4	-2.92e-4	-2.89e-4	-3.38e-4	-4.34e-4
ε_y	-3.50e-4	-2.93e-4	-3.45e-4	-2.68e-4	-1.15e-4
ε_z	8.77e-4	8.60e-4	8.81e-4	8.78e-4	8.72e-4

(c) volume filler content 30%

Table 4.8: Material characteristic values of a uniaxial tensile test with a unidirectional short fiber-reinforced specimen with (a) 10%, (b) 20% and (c) 30% (from top to bottom) fiber volume content respective to various fiber orientations.

$$\mathbb{C}_{\xi,H}^{0^\circ} = \begin{pmatrix} 6163.41 & 3976.58 & 3892.40 & 4.50 & -1.13 & 0.57 \\ 3976.58 & 6196.71 & 3906.77 & -0.17 & 0.46 & -0.44 \\ 3892.40 & 3906.77 & 9111.38 & 1.43 & 22.37 & 1.56 \\ 4.50 & -0.17 & 1.43 & 2219.04 & -0.62 & -0.70 \\ -1.13 & 0.46 & 22.37 & -0.62 & 2292.83 & 2.92 \\ 0.57 & -0.44 & 1.56 & -0.70 & 2.92 & 2253.73 \end{pmatrix}$$

(a) fiber orientation 0°

$$\mathbb{C}_{\xi,H}^{45^\circ} = \begin{pmatrix} 6189.56 & 3937.77 & 3936.04 & -7.96 & -43.41 & 13.41 \\ 3937.76 & 6886.21 & 4576.09 & 18.34 & 972.98 & 12.24 \\ 3936.04 & 4576.09 & 6897.24 & 25.26 & 977.65 & 27.33 \\ -7.96 & 18.34 & 25.26 & 2249.63 & 30.39 & 41.09 \\ -43.41 & 972.98 & 977.65 & 30.39 & 3642.92 & 29.38 \\ 13.41 & 12.24 & 27.33 & 41.09 & 29.38 & 2245.24 \end{pmatrix}$$

(b) fiber orientation 45°

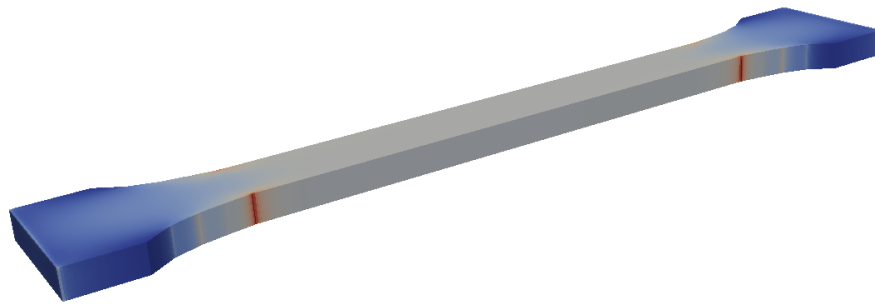
$$\mathbb{C}_{\xi,H}^{60^\circ} = \begin{pmatrix} 6228.65 & 3938.61 & 3960.34 & -0.28 & -24.83 & 0.74 \\ 3938.61 & 7439.97 & 4308.67 & 13.45 & 972.09 & 4.08 \\ 3960.34 & 4308.67 & 6343.00 & 0.95 & 342.82 & -10.06 \\ -0.28 & 13.45 & 0.95 & 2303.75 & -0.30 & 42.82 \\ -24.83 & 972.09 & 342.82 & -0.30 & 3051.25 & 6.31 \\ 0.74 & 4.08 & -10.06 & 42.82 & 6.31 & 2246.48 \end{pmatrix}$$

(c) fiber orientation 60°

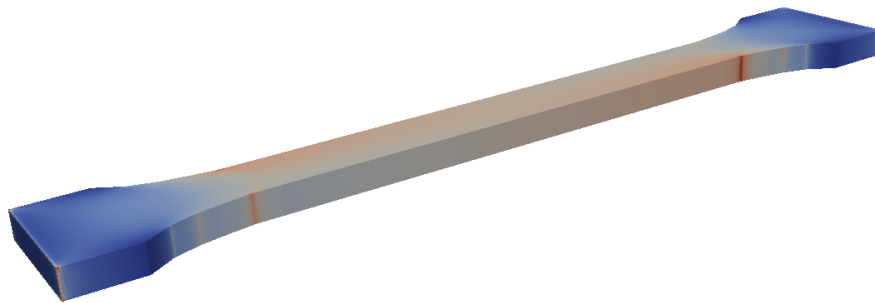
$$\mathbb{C}_{\xi,H}^{90^\circ} = \begin{pmatrix} 6163.41 & 3892.40 & 3976.58 & 0.57 & 1.13 & -4.50 \\ 3892.40 & 9111.38 & 3906.77 & 1.56 & -22.37 & -1.43 \\ 3976.58 & 3906.77 & 6196.71 & -0.44 & -0.46 & 0.17 \\ 0.57 & 1.56 & -0.44 & 2253.73 & -2.92 & 0.70 \\ 1.13 & -22.37 & -0.46 & -2.92 & 2292.83 & -0.62 \\ -4.50 & -1.43 & 0.17 & 0.70 & -0.62 & 2219.04 \end{pmatrix}$$

(d) fiber orientation 90°

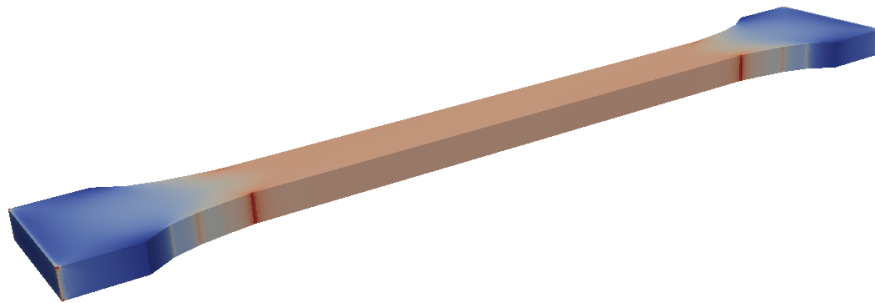
Figure 4.12: Elastic two-scale tensors with (a) 0° , (b) 45° , (c) 60° and (d) 90° fiber orientation to the applied force for a short fiber-reinforced microstructure with 10% fiber volume fraction.



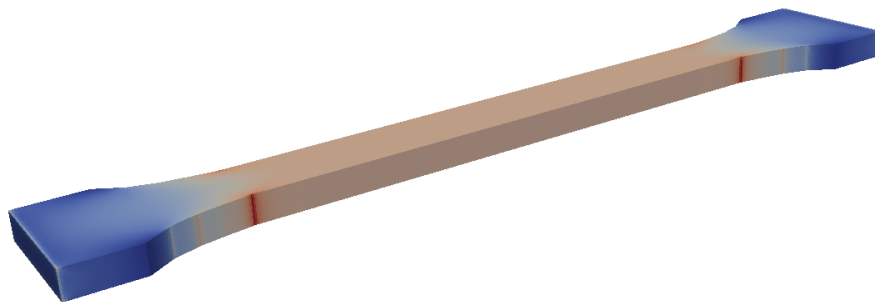
(a) fiber orientation 0°



(b) fiber orientation 45°



(c) fiber orientation 60°



(d) fiber orientation 90°

Figure 4.13: Specimen stress states for different aligned uniaxial fiber orientations (a) 0° , (b) 45° , (c) 60° and (d) 90° under uniaxial tensile of a short fiber-reinforced solid with 10% fiber volume fraction (increasing values from blue to red).

Chapter 5

Rate-independent material models with memory

This chapter introduces the energetic framework in solids $\Omega \subset \mathbb{R}^D$ with $D = 2, 3$ for some rate-independent material models and their incremental formulation. Inelastic effects like small strain damage and plasticity can be described by material models with history variables.

5.1 Materials with memory

We aim at finding displacements $\mathbf{u}: [0, T] \times \Omega \rightarrow \mathbb{R}^D$ in the time interval $[0, T]$ of a material which is described by internal variables $\mathbf{z}: [0, T] \times \Omega \rightarrow \mathbb{R}^N$ and where the evolution is determined by the total energy and dissipation functionals

$$\begin{aligned}\mathcal{E}(t, \mathbf{u}, \mathbf{z}) &= \int_{\Omega} W(\mathbf{x}, \boldsymbol{\varepsilon}(\mathbf{u}), \mathbf{z}) \, d\mathbf{x} - \langle \ell(t), \mathbf{u} \rangle, \\ \mathcal{R}(\dot{\mathbf{z}}) &= \int_{\Omega} R(\mathbf{x}, \dot{\mathbf{z}}) \, d\mathbf{x}.\end{aligned}$$

The load functional is given by

$$\langle \ell(t), \mathbf{u} \rangle = \int_{\Omega} \mathbf{b}(t) \cdot \mathbf{u} \, d\mathbf{x} + \int_{\Gamma_N} \mathbf{t}_N(t) \cdot \mathbf{u} \, da$$

with volume forces $\mathbf{b}: [0, T] \times \Omega \rightarrow \mathbb{R}^D$ and body forces $\mathbf{t}_N: [0, T] \times \Gamma_N \rightarrow \mathbb{R}^D$.

We assume that the material is rate-independent, i.e., the inelastic deformation is independent from scaling in time. This is achieved, if the dissipative function R is 1-homogeneous.

In our models, we only consider small strains $\boldsymbol{\varepsilon} = \boldsymbol{\varepsilon}(\mathbf{u})$ with $\boldsymbol{\varepsilon}(\mathbf{u}) = \text{sym}(\nabla \mathbf{u})$, and we use the spaces for the displacements $V = H^1(\Omega, \mathbb{R}^N)$ and $V(\mathbf{0}) = \{\mathbf{v} \in V : \mathbf{v} =$

0 on Γ_D } including homogeneous boundary conditions on the Dirichlet boundary $\Gamma_D \subset \partial\Omega$. For the internal variable we use the space $L_2(\Omega, \mathbb{R}^N)$. If the total energy functional $\mathcal{E}: [0, T] \times V \times Z \rightarrow \mathbb{R}$ is bounded and uniformly convex in suitable spaces $V(\mathbf{0}) \times Z$, and if the dissipation functional $\mathcal{R}: Z \rightarrow \mathbb{R} \cup \{\infty\}$ is convex, proper and lower semi-continuous, an energetic solution

$$(\mathbf{u}, \mathbf{z}): [0, T] \longrightarrow V \times Z$$

exists which is characterized by

$$\begin{aligned} \textbf{Equilibrium} \quad 0 &= \partial_{\mathbf{u}} \mathcal{E}(t, \mathbf{u}(t), \mathbf{z}(t)), \\ \textbf{Flow Rule} \quad 0 &\in \partial_{\mathbf{z}} \mathcal{E}(t, \mathbf{u}(t), \mathbf{z}(t)) + \partial \mathcal{R}(\dot{\mathbf{z}}(t)) \end{aligned}$$

and boundary conditions for the displacement $\mathbf{u}(t) = \mathbf{u}_D(t)$ on the Dirichlet boundary $\Gamma_D \subset \partial\Omega$, see [38].

Different inelastic models for damage and plasticity are obtained by specifying the local energy W and the local dissipation R , only depending on the quantities $\boldsymbol{\varepsilon}(t, \mathbf{x})$, $\mathbf{z}(t, \mathbf{x})$ and $\dot{\mathbf{z}}(t, \mathbf{x})$ at time t and the material point \mathbf{x} .

5.1.1 A simple damage model

Continuum damage mechanics phenomenologically describes the expansion of micro cracks and cavities by an additional state variable. Therefore, we consider around a continuum mechanics material point a volume element intersected by a cross sectional area which is running through inhomogeneous distributed fracture. The proportion of a representative cross sectional area A_0 and damaged area A_d express the damage evolution by the variable

$$d = \frac{A_d}{A_0} \in [0, 1].$$

This measure of micromechanical damage processes was first proposed by Kachanov [28]. A material point is undamaged for $d = 0$ and fully damaged if $d = 1$. Robotnov's idea, e.g. see [49], uses the effective cross sectional area

$$\tilde{A} = A_0 - A_d$$

to define an effective stress response

$$\tilde{\boldsymbol{\sigma}} = \frac{F}{\tilde{A}} = \frac{F}{A_0(1-d)} = \frac{\boldsymbol{\sigma}}{1-d}.$$

By the hypothesis of the equivalent strain $\tilde{\boldsymbol{\varepsilon}} = \boldsymbol{\varepsilon}$, e.g. see Ju [27] and Lemaitre [32], we derive the following stress relation

$$\boldsymbol{\sigma} = (1 - d)\mathbb{C}[\boldsymbol{\varepsilon}].$$

This relation describes phenomenologically the isotropic damage behavior of a material by an effective material response. Instead of using the equivalent strain hypothesis, anisotropic damage material behavior can be modeled by introducing a fourth order tensor, e.g. see [8, 46], in combination with the equivalence energy hypothesis, see [54].

Within the energetic framework we set $N = 1$ and the internal variable is denoted by $\mathbf{z} = d$. This phenomenological setting is determined by the free energy

$$W(\mathbf{x}, \boldsymbol{\varepsilon}, d) = (1 - d)W_{\text{elastic}}(\mathbf{x}, \boldsymbol{\varepsilon}) + W_{\text{damage}}(d)$$

and the dissipation functional

$$R_{\text{damage}}(\mathbf{x}, \dot{d}) = \begin{cases} 0 & \dot{d} \geq 0, \\ +\infty & \text{otherwise.} \end{cases} \quad (5.1)$$

The damage variable simply scales the elastic energy

$$W_{\text{elastic}}(\mathbf{x}, \boldsymbol{\varepsilon}) = \frac{1}{2}\boldsymbol{\varepsilon}(\mathbf{x}) : \mathbb{C}(\mathbf{x})[\boldsymbol{\varepsilon}(\mathbf{x})] \quad (5.2)$$

by the factor $1 - d$, so that $d = 0$ corresponds to the undamaged elastic material. The dissipation just ensures the irreversibility of the damage process, and $d \in (0, 1)$ describes the fraction of damage.

The additional term W_{damage} determines the evolution of the damage variable and guarantees $d < 1$. It is constructed in analogy to isotropic plasticity. We assume that the damage evolution is locally controlled by a strictly monotone function Φ depending on the local elastic energy $Y = W_{\text{elastic}}(\mathbf{x}, \boldsymbol{\varepsilon}(\mathbf{u}))$ and the complementarity conditions

$$\dot{d} \geq 0, \quad \Phi(Y) - d \leq 0, \quad (\Phi(Y) - d)\dot{d} = 0, \quad (5.3)$$

i.e., d can only increase and not decrease and the material remains elastic, if the local elastic energy is small satisfying $\Phi(Y) < d$. Here, the choice

$$\Phi(Y) = 1 - \exp(-H(\sqrt{2Y} - Y_0))$$

with damping and yielding point material parameters $H, Y_0 \geq 0$ is designed such that the material responds elastically for $\Phi(Y) < 0$, i.e., $\sqrt{2Y} < Y_0$, and $\Phi(Y) \rightarrow 1$ for large Y . Nevertheless, since $\Phi(Y) < 1$ for all Y , the damage variable will not reach $d = 1$ which prevents fracture in this model.

Since Φ is assumed to be strictly monotone, its inverse is uniquely defined and the complementarity conditions (5.3) take the form

$$\dot{d} \geq 0, \quad Y - \Phi^{-1}(d) \leq 0, \quad (Y - \Phi^{-1}(d))\dot{d} = 0.$$

Due to our choice of the dissipation this is equivalent to $Y - \Phi^{-1}(d) \in \partial R_{\text{damage}}(\mathbf{x}, \dot{d})$. This motivates the definition of the defect energy

$$W_{\text{damage}}(d) = \int_0^d \Phi^{-1}(\delta) \, d\delta, \quad (5.4)$$

i.e., $\Phi^{-1}(d) = \partial_d W_{\text{damage}}(d)$ and $Y - \Phi^{-1}(d) = -\partial_d W(\mathbf{x}, \boldsymbol{\varepsilon}, d)$.

For fixed strain $\boldsymbol{\varepsilon}$ the flow rule $0 \in \partial_d W(\mathbf{x}, \boldsymbol{\varepsilon}, d) + \partial R_{\text{damage}}(\mathbf{x}, \dot{d})$ characterizes the minimum of $f(\boldsymbol{\varepsilon}; d) = W(\mathbf{x}, \boldsymbol{\varepsilon}, d) + R_{\text{damage}}(\mathbf{x}, \dot{d})$. Together, we observe that the minimizer is characterized by (5.3).

For our choice of Φ we observe $\Phi^{-1}(d) = \frac{1}{2} (Y_0 - \frac{1}{H} \log(1-d))^2$, so that $W_{\text{damage}}(d) \rightarrow \infty$ for $d \rightarrow 1$ prevents reaching a fully damaged material in this model. Nevertheless, we will see below that the inelastic energy is not uniformly convex, so that a well-defined evolution is only determined for sufficiently small loads or displacements.

Remark 5.1

This simple model does not allow computing the transition to fracture. Due to the choice of Φ , the energy in this model is only convex for sufficiently small damage, and the consistent tangent gets indefinite for d close to 1, so that one cannot expect convergence for the Newton method for large loads. Therefore, simulations for larger loads need an extension of the model.

5.1.2 Small strain elasto-plasticity

For the elasto-plastic model with hardening we set $N = 6$, and the internal variables $\mathbf{z} = (\boldsymbol{\varepsilon}_p, r)$ are the plastic strain $\boldsymbol{\varepsilon}_p$ with trace $\boldsymbol{\varepsilon}_p = 0$ and the isotropic hardening parameter r . The strain is decomposed into elastic and plastic part $\boldsymbol{\varepsilon}(\mathbf{u}) = \boldsymbol{\varepsilon}_e + \boldsymbol{\varepsilon}_p$, and the free energy is given by

$$W(\mathbf{x}, \boldsymbol{\varepsilon}, \boldsymbol{\varepsilon}_p, r) = W_{\text{elastic}}(\mathbf{x}, \boldsymbol{\varepsilon}(\mathbf{u}) - \boldsymbol{\varepsilon}_p) + W_{\text{plastic}}(\boldsymbol{\varepsilon}_p, r)$$

with the elastic energy (5.2) and defect energy

$$W_{\text{plastic}}(\boldsymbol{\varepsilon}_p, r) = W_{\text{kin}}(\boldsymbol{\varepsilon}_p) + W_{\text{iso}}(r) \quad (5.5)$$

combining kinematic and isotropic hardening. The translation of the yield surface is described by kinematic hardening with

$$W_{\text{kin}}(\boldsymbol{\varepsilon}_p) = \frac{1}{2}K\boldsymbol{\varepsilon}_p : \boldsymbol{\varepsilon}_p$$

depending on the hardening parameter $K \geq 0$. The expansion of the yield surface is described by isotropic hardening determined by the yield function

$$\Psi(r) = \sigma_y + H_0 r + (K_\infty - K_0)(1 - \exp(\delta r))$$

for given material parameters $\sigma_y, H_0, \delta \geq 0$ and $K_\infty \geq K_0 \geq 0$. Now we construct the remaining energy contribution and the dissipation such that the plastic evolution satisfies the yield condition $|\text{dev } \boldsymbol{\sigma} - \boldsymbol{\beta}| + \Psi(r) \leq 0$.

The energy definition corresponds to the constitutive stress-stain relation

$$\boldsymbol{\sigma} = \partial_{\boldsymbol{\varepsilon}} W(\mathbf{x}, \boldsymbol{\varepsilon}, \boldsymbol{\varepsilon}_p, r) = \partial_{\boldsymbol{\varepsilon}} W_{\text{elastic}}(\mathbf{x}, \boldsymbol{\varepsilon}(\mathbf{u}) - \boldsymbol{\varepsilon}_p) = \mathbb{C}[\boldsymbol{\varepsilon}(\mathbf{u}) - \boldsymbol{\varepsilon}_p].$$

It defines the back stress $\boldsymbol{\beta} = \partial_{\boldsymbol{\varepsilon}_p} W_{\text{kin}}(\boldsymbol{\varepsilon}_p) = K\boldsymbol{\varepsilon}_p$, and the conjugate variables $\mathbf{y} = (\boldsymbol{\alpha}, \zeta) = -\partial_{\mathbf{z}} W(\mathbf{x}, \boldsymbol{\varepsilon}, \mathbf{z})$ with

$$\begin{aligned} \boldsymbol{\alpha} &= \partial_{\boldsymbol{\varepsilon}_p} W_{\text{elastic}}(\mathbf{x}, \boldsymbol{\varepsilon}(\mathbf{u}) - \boldsymbol{\varepsilon}_p) - \partial_{\boldsymbol{\varepsilon}_p} W_{\text{kin}}(\boldsymbol{\varepsilon}_p) = \text{dev } \boldsymbol{\sigma} - \boldsymbol{\beta}, \\ \zeta &= -\partial_r W_{\text{iso}}(r). \end{aligned}$$

This yields the constitutive relation $\zeta = -\partial_r W_{\text{iso}}(r) = -\Psi(r)$ by defining

$$W_{\text{iso}}(r) = \int_0^r \Psi(\rho) \, d\rho.$$

The plastic evolution is determined by the plastic potential

$$R_{\text{plastic}}^*(\mathbf{x}, \boldsymbol{\alpha}, \zeta) = \begin{cases} 0 & |\boldsymbol{\alpha}| + \zeta \leq 0 \text{ and } \zeta \leq 0, \\ +\infty & \text{otherwise,} \end{cases}$$

which is by duality equivalent to the dissipation functional

$$R_{\text{plastic}}(\mathbf{x}, \dot{\boldsymbol{\varepsilon}}_p, \dot{r}) = \begin{cases} 0 & \dot{r} \geq |\dot{\boldsymbol{\varepsilon}}_p|, \\ +\infty & \text{otherwise.} \end{cases} \quad (5.6)$$

The flow rule $(\boldsymbol{\alpha}, \zeta) \in \partial R_{\text{plastic}}(\mathbf{x}, \dot{\boldsymbol{\varepsilon}}_p, \dot{r})$ in every material point is evaluated by duality, i.e. $(\dot{\boldsymbol{\varepsilon}}_p, \dot{r}) \in \partial R_{\text{plastic}}^*(\mathbf{x}, \boldsymbol{\alpha}, \zeta)$. Introducing a consistency parameter λ_p this is equivalent to the normality rule

$$\dot{\boldsymbol{\varepsilon}}_p = \lambda_p \frac{\boldsymbol{\alpha}}{|\boldsymbol{\alpha}|}, \quad \dot{r} = \lambda_p, \quad (5.7)$$

and the complementarity conditions

$$\lambda_p \geq 0, \quad |\boldsymbol{\alpha}| + \zeta \leq 0, \quad \lambda_p(|\boldsymbol{\alpha}| + \zeta) = 0. \quad (5.8)$$

In particular, this implies $|\dot{\boldsymbol{\varepsilon}}_p| = \dot{r}$, and assuming $\boldsymbol{\varepsilon}_p(0) = \mathbf{0}$ and $r(0) = 0$ at initial time $t = 0$, we obtain

$$r(t) = \int_0^t \dot{r} \, dt = \int_0^t |\dot{\boldsymbol{\varepsilon}}_p| \, dt,$$

i.e., r is the equivalent plastic strain.

5.1.3 Damage and elasto-plasticity

For the model combining damage and elasto-plasticity we use the internal variables $\mathbf{z} = (d, \boldsymbol{\varepsilon}_p, r)$ with $N = 7$ components and the free energy

$$\begin{aligned} W(\mathbf{x}, \boldsymbol{\varepsilon}, d, \boldsymbol{\varepsilon}_p, r) &= (1 - d)W_{\text{elastic}}(\mathbf{x}, \boldsymbol{\varepsilon}(\mathbf{u}) - \boldsymbol{\varepsilon}_p) + W_{\text{defect}}(\mathbf{z}) \\ &= (1 - d)(W_{\text{elastic}}(\mathbf{x}, \boldsymbol{\varepsilon}(\mathbf{u}) - \boldsymbol{\varepsilon}_p) + W_{\text{plastic}}(\boldsymbol{\varepsilon}_p, r)) + W_{\text{damage}}(d) \end{aligned}$$

with the elastic energy (5.2) and defect energy components (5.4) and (5.5). The dissipation combines (5.1) and (5.6) to

$$\mathcal{R}(\mathbf{x}, \dot{d}, \dot{\boldsymbol{\varepsilon}}_p, \dot{r}) = \int_{\Omega} R(\mathbf{x}, \dot{d}, \dot{\boldsymbol{\varepsilon}}_p, \dot{r}) \, d\mathbf{x}, \quad R(\mathbf{x}, \dot{d}, \dot{\boldsymbol{\varepsilon}}_p, \dot{r}) = R_{\text{damage}}(\mathbf{x}, \dot{d}) + R_{\text{plastic}}(\mathbf{x}, \dot{\boldsymbol{\varepsilon}}_p, \dot{r}).$$

The flow rule $(0, \mathbf{0}, 0) \in \partial_{(d, \boldsymbol{\varepsilon}_p, r)} W(\mathbf{x}, \boldsymbol{\varepsilon}, d, \boldsymbol{\varepsilon}_p, r) + \partial R(\mathbf{x}, \dot{d}, \dot{\boldsymbol{\varepsilon}}_p, \dot{r})$ in every material point is evaluated by duality, i.e. first evaluate $(\dot{\boldsymbol{\varepsilon}}_p, \dot{r}) \in \partial R_{\text{plastic}}^*(\mathbf{x}, \boldsymbol{\alpha}, \zeta)$ by (5.8) and (5.7); and then $\dot{d} \in \partial R_{\text{damage}}^*(\mathbf{x}, y)$ by (5.3), corresponding to the conjugate variables $\mathbf{y} = (y, \boldsymbol{\alpha}, \zeta) = -\partial_{\mathbf{z}} W(\mathbf{x}, \boldsymbol{\varepsilon}, \mathbf{z})$.

5.2 The incremental problem

The evolution in time is approximated by a series of incremental problems. Let $0 = t_0 < t_1 < \dots < t_{N_{\max}} = T$ be a time series with $\Delta t_n = t_n - t_{n-1}$. Starting with $(\mathbf{u}^0, \mathbf{z}^0)$ we define for $n = 1, \dots, N_{\max}$ the following incremental problems depending on the given history variable \mathbf{z}^{n-1} , the load functional $\ell^n = \ell(t_n)$ and the Dirichlet data $\mathbf{u}_D^n = \mathbf{u}_D(t_n)$: find a minimizer $(\mathbf{u}^n, \mathbf{z}^n) \in V(\mathbf{u}_D^n) \times Z$ of the incremental functional

$$\mathcal{J}_n(\mathbf{u}^n, \mathbf{z}^n) = \mathcal{E}(t_n, \mathbf{u}^n, \mathbf{z}^n) + \mathcal{R}(\mathbf{z}^n - \mathbf{z}^{n-1}).$$

In our applications $\mathcal{J}_n(\cdot)$ is uniformly convex, so that a unique minimizer exists. It is determined by computing a critical point of $\mathcal{J}_n(\cdot)$ characterized by the nonlinear system

$$\mathbf{Equilibrium} \quad 0 = \partial_{\mathbf{u}}\mathcal{E}(t_n, \mathbf{u}^n, \mathbf{z}^n), \quad (5.9a)$$

$$\mathbf{Flow Rule} \quad 0 \in \partial_{\mathbf{z}}\mathcal{E}(t_n, \mathbf{u}^n, \mathbf{z}^n) + \partial\mathcal{R}(\Delta\mathbf{z}^n). \quad (5.9b)$$

Since we consider rate-independent materials, the flow rule is 1-homogeneous satisfying $\Delta t_n \mathcal{R}((\Delta t_n)^{-1}(\mathbf{z}^n - \mathbf{z}^{n-1})) = \mathcal{R}(\mathbf{z}^n - \mathbf{z}^{n-1})$ and thus depending only on the increment $\Delta\mathbf{z}^n = \mathbf{z}^n - \mathbf{z}^{n-1}$.

We specify the constitutive settings of these models, and we derive the return mapping and the corresponding consistent tangent operators. For this treatment we forgo the dependency on the material point \mathbf{x} of the local energy W and the local dissipation R .

5.2.1 The incremental flow rule for the damage model

In the first step, we consider the semi-discrete problem in time. For given history variable d^{n-1} , the incremental problem (5.9) determines $(\mathbf{u}^n, d^n) \in V(\mathbf{u}_D^n) \times L_2(\Omega)$ with

$$0 = \int_{\Omega} \partial_{\varepsilon}W(\varepsilon(\mathbf{u}^n), d^n) : \varepsilon(\delta\mathbf{u}) \, d\mathbf{x} - \langle \ell^n, \delta\mathbf{u} \rangle, \quad \delta\mathbf{u} \in V(\mathbf{0}), \quad (5.10a)$$

$$0 \in \partial_d W(\varepsilon(\mathbf{u}^n), d^n) + \partial R_{\text{damage}}(d^n - d^{n-1}). \quad (5.10b)$$

The solution (\mathbf{u}^n, d^n) of (5.10) is a critical point of the functional

$$J_n(\mathbf{u}, d) = \int_{\Omega} W(\varepsilon(\mathbf{u}), d) \, d\mathbf{x} - \langle \ell^n, \mathbf{u} \rangle + \int_{\Omega} R_{\text{damage}}(d - d^{n-1}) \, d\mathbf{x} \quad (5.11)$$

subject to the essential boundary conditions $\mathbf{u} = \mathbf{u}_D$ on Γ_D .

The incremental damage problem can be reduced to a nonlinear problem for the displacement by inserting the local solution of the incremental flow rule depending on the strain. This is based on the following result.

lemma 5.2

For given history variable d^{n-1} and fixed strain ε the unique solution Δd of the local incremental flow rule in every material point

$$0 \in \partial_d W(\varepsilon, d^{n-1} + \Delta d) + \partial R_{\text{damage}}(\Delta d)$$

is given by

$$\Delta d = \max \{0, \Phi(Y(\varepsilon)) - d^{n-1}\}, \quad Y(\varepsilon) = W_{\text{elastic}}(\varepsilon).$$

Proof. Evaluating $\partial_d W(\boldsymbol{\varepsilon}, d^{n-1} + \Delta d) = -Y(\boldsymbol{\varepsilon}) + \Phi^{-1}(d^{n-1} + \Delta d)$ in the incremental flow rule yields

$$Y(\boldsymbol{\varepsilon}) - \Phi^{-1}(d^{n-1} + \Delta d) \in \partial R_{\text{damage}}^*(\Delta d) = \begin{cases} \{0\} & \Delta d > 0, \\ (-\infty, 0] & \Delta d = 0, \\ \emptyset & \Delta d < 0. \end{cases}$$

This is equivalent to the complementarity condition

$$\Delta d \geq 0, \quad \Phi(Y(\boldsymbol{\varepsilon})) - d^{n-1} - \Delta d \leq 0, \quad (\Phi(Y(\boldsymbol{\varepsilon})) - d^{n-1} - \Delta d) \Delta d = 0$$

which directly implies $\Delta d = \max\{0, \Phi(Y(\boldsymbol{\varepsilon})) - d^{n-1}\}$. \square

The evaluation of the flow rule defines the update of the damage variable

$$d_n(\boldsymbol{\varepsilon}) = d^{n-1} + \Delta d = d^{n-1} + \max\{0, \Phi(Y(\boldsymbol{\varepsilon})) - d^{n-1}\}$$

and the incremental stress response

$$\boldsymbol{\sigma}_n(\boldsymbol{\varepsilon}) = (1 - d_n(\boldsymbol{\varepsilon}))\mathbb{C}[\boldsymbol{\varepsilon}].$$

Choosing $\text{sgn}(s) \in \partial \max\{0, s\}$ with

$$\text{sgn}(s) = \begin{cases} 1 & s > 0, \\ 0 & \text{otherwise} \end{cases}$$

defines the consistent tangent $\mathbb{C}_n(\boldsymbol{\varepsilon}) \in \partial \boldsymbol{\sigma}_n(\boldsymbol{\varepsilon})$ by

$$\begin{aligned} \mathbb{C}_n(\boldsymbol{\varepsilon})[\delta \boldsymbol{\varepsilon}] &= (1 - d_n(\boldsymbol{\varepsilon}))\mathbb{C}(\boldsymbol{\varepsilon})[\delta \boldsymbol{\varepsilon}] \\ &\quad - \text{sgn}\left(\max\{0, \Phi(Y(\boldsymbol{\varepsilon})) - d^{n-1}\}\right) \Phi'(Y(\boldsymbol{\varepsilon}))(\mathbb{C}[\boldsymbol{\varepsilon}] : \delta \boldsymbol{\varepsilon})\mathbb{C}[\boldsymbol{\varepsilon}] \end{aligned}$$

with $\Phi'(Y) = \frac{H}{\sqrt{2Y}} \exp(-H(\sqrt{2Y} - Y_0))$.

The incremental problem can be solved by minimizing the reduced functional for the displacement

$$\begin{aligned} J_n^{\text{red}}(\mathbf{u}) &= \int_{\Omega} W(\boldsymbol{\varepsilon}(\mathbf{u}), d_n(\boldsymbol{\varepsilon}(\mathbf{u}))) \, d\mathbf{x} - \langle \boldsymbol{\ell}^n, \mathbf{u} \rangle \\ &= \int_{\Omega} \left(\int_0^{Y(\boldsymbol{\varepsilon}(\mathbf{u}))} (1 - d^{n-1} - \max\{0, \Phi(y) - d^{n-1}\}) \, dy \right) d\mathbf{x} - \langle \boldsymbol{\ell}^n, \mathbf{u} \rangle. \end{aligned}$$

Within a generalized Newton method, the consistent tangent defines the second variation

$$\partial^2 J_n^{\text{red}}(\mathbf{u})[\Delta \mathbf{u}, \delta \mathbf{u}] = \int_{\Omega} \mathbb{C}_n(\boldsymbol{\varepsilon}(\mathbf{u}))[\boldsymbol{\varepsilon}(\Delta \mathbf{u})] : \boldsymbol{\varepsilon}(\delta \mathbf{u}) \, d\mathbf{x}.$$

For our choice Φ determining the damage evolution we observe for the consistent tangent $\mathbb{C}_n(\boldsymbol{\varepsilon})[\boldsymbol{\varepsilon}] : \boldsymbol{\varepsilon} < 0$ for large $\boldsymbol{\varepsilon}$, so that the second variation of J_n^{red} is not positive and thus J_n^{red} is only convex for sufficiently small strains. This restricts the application of this damage model to moderate loads. An extended damage model with convex energy can be obtained by including gradient terms, see, e.g., [62].

5.2.2 The incremental flow rule for elasto-plasticity

For the incremental problem the local computation of the stress response and the consistent tangent in every material point in the RVEs is reduced to a scalar nonlinear problem for the equivalent plastic strain increment.

lemma 5.3

For given history variables $(\boldsymbol{\varepsilon}_p^{n-1}, r^{n-1})$ and strain $\boldsymbol{\varepsilon}$ a unique solution $(\Delta\boldsymbol{\varepsilon}_p, \Delta r)$ of the local flow rule in every material point

$$(\mathbf{0}, 0) \in \partial_{(\boldsymbol{\varepsilon}_p, r)} W(\boldsymbol{\varepsilon}, \boldsymbol{\varepsilon}_p^{n-1} + \Delta\boldsymbol{\varepsilon}_p, r^{n-1} + \Delta r) + \partial R_{\text{plastic}}(\Delta\boldsymbol{\varepsilon}_p, \Delta r)$$

exists.

Proof. For fixed history and given strain $\boldsymbol{\varepsilon}$, the increment is a minimizer of

$$\Phi(\Delta\boldsymbol{\varepsilon}_p, \Delta r; \boldsymbol{\varepsilon}) = W(\boldsymbol{\varepsilon}, \boldsymbol{\varepsilon}_p^{n-1} + \Delta\boldsymbol{\varepsilon}_p, r^{n-1} + \Delta r) + R_{\text{plastic}}(\Delta\boldsymbol{\varepsilon}_p, \Delta r).$$

Since the functional is uniformly convex in \mathbb{R}^6 , the minimizer exists and it is unique. For the evaluation we define the conjugated variables

$$(\boldsymbol{\alpha}, \zeta) = -\partial_{(\boldsymbol{\varepsilon}_p, r)} W(\boldsymbol{\varepsilon}, \boldsymbol{\varepsilon}_p^{n-1} + \Delta\boldsymbol{\varepsilon}_p, r^{n-1} + \Delta r)$$

we obtain $\boldsymbol{\alpha} = \text{dev } \boldsymbol{\sigma} - K(\boldsymbol{\varepsilon}_p^{n-1} + \Delta\boldsymbol{\varepsilon}_p)$ from the stress $\boldsymbol{\sigma} = \mathbb{C}[\boldsymbol{\varepsilon} - \boldsymbol{\varepsilon}_p^{n-1} - \Delta\boldsymbol{\varepsilon}_p]$, and $\zeta = -\Psi(r^{n-1} + \Delta r)$. Evaluating

$$(\Delta\boldsymbol{\varepsilon}_p, \Delta r) \in \partial R_{\text{plastic}}^*(\boldsymbol{\alpha}, \zeta) = \begin{cases} \{0\} & |\boldsymbol{\alpha}| + \zeta < 0, \\ [0, \infty) \begin{pmatrix} \frac{\boldsymbol{\alpha}}{|\boldsymbol{\alpha}|} \\ 1 \end{pmatrix} & |\boldsymbol{\alpha}| + \zeta = 0, \\ \emptyset & |\boldsymbol{\alpha}| + \zeta > 0 \end{cases}$$

yields the normality rule

$$\begin{pmatrix} \Delta\boldsymbol{\varepsilon}_p \\ \Delta r \end{pmatrix} = \lambda_p \begin{pmatrix} \frac{\boldsymbol{\alpha}}{|\boldsymbol{\alpha}|} \\ 1 \end{pmatrix}$$

and the complementarity conditions for the consistency parameter λ_p

$$\lambda_p \geq 0, \quad |\boldsymbol{\alpha}| + \zeta \leq 0, \quad \lambda_p(|\boldsymbol{\alpha}| + \zeta) = 0.$$

This yields $\Delta r = \lambda_p$ and, in the isotropic case, the deviatoric stress $\text{dev } \boldsymbol{\sigma} = 2\mu(\text{dev } \boldsymbol{\varepsilon} - \boldsymbol{\varepsilon}_p)$ and for the flow direction

$$\frac{\Delta \boldsymbol{\varepsilon}}{|\Delta \boldsymbol{\varepsilon}|} = \frac{\boldsymbol{\alpha}}{|\boldsymbol{\alpha}|} = \frac{2\mu \text{dev } \boldsymbol{\varepsilon} - (2\mu + K)\boldsymbol{\varepsilon}_p}{|2\mu \text{dev } \boldsymbol{\varepsilon} - (2\mu + K)\boldsymbol{\varepsilon}_p|} = \frac{\boldsymbol{\alpha}_n^{\text{tr}}(\boldsymbol{\varepsilon})}{|\boldsymbol{\alpha}_n^{\text{tr}}(\boldsymbol{\varepsilon})|}$$

with the relative trial stress $\boldsymbol{\alpha}_n^{\text{tr}}(\boldsymbol{\varepsilon}) = 2\mu \text{dev } \boldsymbol{\varepsilon} - (2\mu + K)\boldsymbol{\varepsilon}_p^{n-1}$. Thus, defining the flow function

$$F_n(\Delta r; \boldsymbol{\varepsilon}) = |\boldsymbol{\alpha}_n^{\text{tr}}(\boldsymbol{\varepsilon})| - (2\mu + K)\Delta r - \Psi(r^{n-1} + \Delta r)$$

we observe $|\boldsymbol{\alpha}| + \zeta = F_n(\Delta r; \boldsymbol{\varepsilon})$. Now, for the given strain $\boldsymbol{\varepsilon}$ we have to distinguish two cases. If $F_n(0; \boldsymbol{\varepsilon}) \leq 0$, we set $\Delta r = 0$. Otherwise, since $F_n(\cdot; \boldsymbol{\varepsilon})$ is strictly monotone and negative for large Δr , the equation $F_n(\Delta r; \boldsymbol{\varepsilon}) = 0$ uniquely determines $\Delta r > 0$. Then, we obtain

$$\Delta \boldsymbol{\varepsilon}_p = \Delta r \frac{\boldsymbol{\alpha}_n^{\text{tr}}(\boldsymbol{\varepsilon})}{|\boldsymbol{\alpha}_n^{\text{tr}}(\boldsymbol{\varepsilon})|}.$$

□

Evaluating the increment $\Delta r_n(\boldsymbol{\varepsilon})$ defines the update of the history variables

$$\begin{aligned} r_n(\boldsymbol{\varepsilon}) &= r^{n-1} + \Delta r_n(\boldsymbol{\varepsilon}), \\ \boldsymbol{\varepsilon}_{p,n}(\boldsymbol{\varepsilon}) &= \boldsymbol{\varepsilon}_p^{n-1} + \Delta r_n(\boldsymbol{\varepsilon}) \frac{\boldsymbol{\alpha}_n^{\text{tr}}(\boldsymbol{\varepsilon})}{|\boldsymbol{\alpha}_n^{\text{tr}}(\boldsymbol{\varepsilon})|}, \end{aligned}$$

the incremental stress response

$$\boldsymbol{\sigma}_n(\boldsymbol{\varepsilon}) = \mathbb{C}[\boldsymbol{\varepsilon} - \boldsymbol{\varepsilon}_{p,n}(\boldsymbol{\varepsilon})],$$

and the consistent tangent $\mathbb{C}_n(\boldsymbol{\varepsilon}) \in \partial \boldsymbol{\sigma}_n(\boldsymbol{\varepsilon})$ by

$$\begin{aligned} \mathbb{C}_n(\boldsymbol{\varepsilon})[\delta \boldsymbol{\varepsilon}] &= \mathbb{C}[\delta \boldsymbol{\varepsilon}] - \frac{4\mu^2 \Delta r_n(\boldsymbol{\varepsilon})}{|\boldsymbol{\alpha}_n^{\text{tr}}(\boldsymbol{\varepsilon})|} \text{dev}(\delta \boldsymbol{\varepsilon}) \\ &+ \left(\frac{4\mu^2 \Delta r_n(\boldsymbol{\varepsilon})}{|\boldsymbol{\alpha}_n^{\text{tr}}(\boldsymbol{\varepsilon})|} - \frac{4\mu^2}{2\mu + K + \Psi'(r_n(\boldsymbol{\varepsilon}))} \right) \frac{\boldsymbol{\alpha}_n^{\text{tr}}(\boldsymbol{\varepsilon}) : \delta \boldsymbol{\varepsilon}}{|\boldsymbol{\alpha}_n^{\text{tr}}(\boldsymbol{\varepsilon})|} \frac{\boldsymbol{\alpha}_n^{\text{tr}}(\boldsymbol{\varepsilon})}{|\boldsymbol{\alpha}_n^{\text{tr}}(\boldsymbol{\varepsilon})|}, \end{aligned}$$

cf. [55, Sect. 3.3.2].

5.2.3 The incremental flow rule for damage and elasto-plasticity

For the incremental problem the local computation of the stress response and the consistent tangent in every material point in the RVEs is evaluated first for the plasticity variables and then for the damage variable.

lemma 5.4

For given history variables $(d^{n-1}, \boldsymbol{\varepsilon}_p^{n-1}, r^{n-1})$ and strain $\boldsymbol{\varepsilon}$ a unique solution $(\Delta d, \Delta \boldsymbol{\varepsilon}_p, \Delta r)$ of the local flow rule in every material point

$$(0, \mathbf{0}, 0) \in \partial_{(d, \boldsymbol{\varepsilon}_p, r)} W(\boldsymbol{\varepsilon}, d^{n-1} + \Delta d, \boldsymbol{\varepsilon}_p^{n-1} + \Delta \boldsymbol{\varepsilon}_p, r^{n-1} + \Delta r) + \partial R(\Delta d, \Delta \boldsymbol{\varepsilon}_p, \Delta r)$$

exists.

Proof. Inserting the conjugated variables

$$\begin{aligned} & -\partial_{(d, \boldsymbol{\varepsilon}_p, r)} W(\boldsymbol{\varepsilon}, d^{n-1} + \Delta d, \boldsymbol{\varepsilon}_p^{n-1} + \Delta \boldsymbol{\varepsilon}_p, r^{n-1} + \Delta r) \\ &= \begin{pmatrix} Y - \Phi^{-1}(d^{n-1} + \Delta d) \\ (1 - d^{n-1} + \Delta d)(\operatorname{dev}(\boldsymbol{\sigma}) - K(\boldsymbol{\varepsilon}_p^{n-1} + \Delta \boldsymbol{\varepsilon}_p)) \\ -(1 - d^{n-1} + \Delta d)\Psi(r^{n-1} + \Delta r) \end{pmatrix} = \begin{pmatrix} Y - \Phi^{-1}(d^{n-1} + \Delta d) \\ (1 - d^{n-1} + \Delta d)\boldsymbol{\alpha} \\ (1 - d^{n-1} + \Delta d)\zeta \end{pmatrix} \end{aligned}$$

with $Y = W_{\text{elastic}}(\boldsymbol{\varepsilon} - \boldsymbol{\varepsilon}_p^{n-1} - \Delta \boldsymbol{\varepsilon}_p)$, the back stress $\boldsymbol{\alpha} = \operatorname{dev} \boldsymbol{\sigma} - K(\boldsymbol{\varepsilon}_p^{n-1} + \Delta \boldsymbol{\varepsilon}_p)$, $\zeta = -\Psi(r^{n-1} + \Delta r)$, and $\boldsymbol{\sigma} = \mathbb{C}[\boldsymbol{\varepsilon} - \boldsymbol{\varepsilon}_p^{n-1} - \Delta \boldsymbol{\varepsilon}_p]$ into the flow rule yields

$$Y - \Phi^{-1}(d^{n-1} + \Delta d) \in \partial R_{\text{damage}}(\Delta d),$$

and, since $R_{\text{plastic}}^*(\cdot)$ is 1-homogeneous,

$$(\Delta \boldsymbol{\varepsilon}_p, \Delta r) \in \partial R_{\text{plastic}}^*(\boldsymbol{\alpha}, \zeta) = \partial R_{\text{plastic}}^*((1 - d^{n-1} + \Delta d)(\boldsymbol{\alpha}, \zeta)).$$

This shows that in the first step, the plastic increment can be evaluated from the plastic flow rule independent from the damage variable. We proceed as in Lem. 5.3. The plastic flow rule is equivalent to the normality rule

$$\begin{pmatrix} \Delta \boldsymbol{\varepsilon}_p \\ \Delta r \end{pmatrix} = \lambda_p \begin{pmatrix} \frac{\boldsymbol{\alpha}}{|\boldsymbol{\alpha}|} \\ 1 \end{pmatrix}$$

and the complementarity conditions for the consistency parameter λ_p

$$\lambda_p \geq 0, \quad |\boldsymbol{\alpha}| + \zeta \leq 0, \quad \lambda_p(|\boldsymbol{\alpha}| + \zeta) = 0.$$

This yields $\Delta r = \lambda_p$ and, in the isotropic case, for the flow direction

$$\frac{\Delta \boldsymbol{\varepsilon}}{|\Delta \boldsymbol{\varepsilon}|} = \frac{\boldsymbol{\alpha}}{|\boldsymbol{\alpha}|} = \frac{2\mu \operatorname{dev} \boldsymbol{\varepsilon} - (2\mu + K)\boldsymbol{\varepsilon}_p}{|2\mu \operatorname{dev} \boldsymbol{\varepsilon} - (2\mu + K)\boldsymbol{\varepsilon}_p|} = \frac{\boldsymbol{\alpha}_n^{\operatorname{tr}}(\boldsymbol{\varepsilon})}{|\boldsymbol{\alpha}_n^{\operatorname{tr}}(\boldsymbol{\varepsilon})|}$$

with the relative trial stress $\boldsymbol{\alpha}_n^{\operatorname{tr}}(\boldsymbol{\varepsilon}) = 2\mu \operatorname{dev} \boldsymbol{\varepsilon} - (2\mu + K)\boldsymbol{\varepsilon}_p^{n-1}$. Thus, defining

$$F_n(\Delta r; \boldsymbol{\varepsilon}) = |\boldsymbol{\alpha}_n^{\operatorname{tr}}(\boldsymbol{\varepsilon})| - (2\mu + K)\Delta r - \Psi(r^{n-1} + \Delta r)$$

we observe $|\boldsymbol{\alpha}| + \zeta = F_n(\Delta r; \boldsymbol{\varepsilon})$. Now, for the given $\boldsymbol{\varepsilon}$ we have to distinguish two cases. If $F_n(0; \boldsymbol{\varepsilon}) \leq 0$, we set $\Delta r = 0$. Otherwise, $\Delta r > 0$ is uniquely determined by the equation $F_n(\Delta r; \boldsymbol{\varepsilon}) = 0$. Then, we obtain

$$\Delta \boldsymbol{\varepsilon}_p = \Delta r \frac{\boldsymbol{\alpha}_n^{\operatorname{tr}}(\boldsymbol{\varepsilon})}{|\boldsymbol{\alpha}_n^{\operatorname{tr}}(\boldsymbol{\varepsilon})|}$$

which also defines $Y_n(\boldsymbol{\varepsilon}) = W_{\text{elastic}}(\boldsymbol{\varepsilon} - \boldsymbol{\varepsilon}_p^{n-1} - \Delta \boldsymbol{\varepsilon}_p)$. Now, the increment of the damage variable is computed as in Lem. 5.2 depending on $Y_n(\boldsymbol{\varepsilon})$, i.e., $\Delta d = \max\{0, \Phi(Y_n(\boldsymbol{\varepsilon})) - d^{n-1}\}$. \square

The evaluation of the flow rule defines the update of the history variables

$$\begin{aligned} d_n(\boldsymbol{\varepsilon}) &= d^{n-1} + \Delta d, \\ \boldsymbol{\varepsilon}_{p,n}(\boldsymbol{\varepsilon}) &= \boldsymbol{\varepsilon}_p^{n-1} + \Delta \boldsymbol{\varepsilon}_p, \\ r_n(\boldsymbol{\varepsilon}) &= r^{n-1} + \Delta r, \end{aligned}$$

the incremental stress response $\boldsymbol{\sigma}_n(\boldsymbol{\varepsilon}) = (1 - d_n(\boldsymbol{\varepsilon}))\mathbb{C}[\boldsymbol{\varepsilon} - \boldsymbol{\varepsilon}_{p,n}(\boldsymbol{\varepsilon})]$, and the consistent tangent $\mathbb{C}_n(\boldsymbol{\varepsilon}) \in \partial \boldsymbol{\sigma}_n(\boldsymbol{\varepsilon})$

$$\begin{aligned} \mathbb{C}_n(\boldsymbol{\varepsilon})[\delta \boldsymbol{\varepsilon}] &= (1 - d_n(\boldsymbol{\varepsilon}))\mathbb{C}_n^{\text{plastic}}(\boldsymbol{\varepsilon})[\delta \boldsymbol{\varepsilon}] \\ &\quad - \operatorname{sgn}\left(\max\{0, \Phi(Y_n(\boldsymbol{\varepsilon})) - d^{n-1}\}\right) (\mathbb{C}[\boldsymbol{\varepsilon} - \boldsymbol{\varepsilon}_{p,n}(\boldsymbol{\varepsilon})] : \delta \boldsymbol{\varepsilon}) \mathbb{C}[\boldsymbol{\varepsilon}] \end{aligned}$$

with

$$\begin{aligned} \mathbb{C}_n^{\text{plastic}}(\boldsymbol{\varepsilon})[\delta \boldsymbol{\varepsilon}] &= \mathbb{C}[\delta \boldsymbol{\varepsilon}] - \frac{4\mu^2 \Delta r}{|\boldsymbol{\alpha}_n^{\operatorname{tr}}(\boldsymbol{\varepsilon})|} \operatorname{dev}(\delta \boldsymbol{\varepsilon}) \\ &\quad + \left(\frac{4\mu^2 \Delta r}{|\boldsymbol{\alpha}_n^{\operatorname{tr}}(\boldsymbol{\varepsilon})|} - \frac{4\mu^2}{2\mu + K + \Psi'(r_n(\boldsymbol{\varepsilon}))} \right) \frac{\boldsymbol{\alpha}_n^{\operatorname{tr}}(\boldsymbol{\varepsilon}) : \delta \boldsymbol{\varepsilon}}{|\boldsymbol{\alpha}_n^{\operatorname{tr}}(\boldsymbol{\varepsilon})|} \frac{\boldsymbol{\alpha}_n^{\operatorname{tr}}(\boldsymbol{\varepsilon})}{|\boldsymbol{\alpha}_n^{\operatorname{tr}}(\boldsymbol{\varepsilon})|}. \end{aligned}$$

Chapter 6

Heterogeneous two-scale FEM for inelasticity

The inelastic material behavior for short fiber-reinforced polymers is modeled by a two-scale infinitesimal elasto-plastic damage material [60, 59]. This model is reformulated in the framework of generalized standard materials, which directly defines the corresponding algorithmic realization within the FE² framework.

6.1 Two-scale models with memory

The energetic framework extends to the two-scale setting as follows. We consider macro-displacements $\mathbf{u}_H: [0, T] \rightarrow V_H$ satisfying the Dirichlet boundary conditions, i.e., $\mathbf{u}_H(t) \in V_H(\mathbf{u}_D(t))$. In every RVE \mathcal{Y}_ξ the micro-fluctuations $\mathbf{v}_{\xi,h}: [0, T] \rightarrow V_{\xi,h}$ and the internal variables describing the material history $\mathbf{z}_{\xi,h}(t): [0, T] \rightarrow Z_{\xi,h}$ have to be determined locally. For the internal variables we use piecewise constant vectors in $Z_{\xi,h} \subset L_2(\mathcal{Y}_\xi, \mathbb{R}^N)$ represented by $z_{\xi,h}(\nu) \in \mathbb{R}^N$ at the integration points $\nu \in \Xi_{\xi,h} \subset \mathcal{Y}_\xi$ in the RVE. As a result, we define the product space $Z_h = \prod_{\xi \in \Xi_H} Z_{\xi,h}$.

The model is specified through the corresponding two-scale energy and dissipation functionals

$$\begin{aligned}\mathcal{E}_H(t, \mathbf{u}_H, \mathbf{v}_h, \mathbf{z}_h) &= \int_{\Xi_H} W_\xi(\boldsymbol{\varepsilon}(\mathbf{u}_H), \mathbf{v}_{\xi,h}, \mathbf{z}_{\xi,h}) - \langle \ell(t), \mathbf{u}_H \rangle, \\ \mathcal{R}_H(\dot{\mathbf{z}}_h) &= \int_{\Xi_H} R_\xi(\dot{\mathbf{z}}_{\xi,h}),\end{aligned}$$

where the contributions at every sample point $\xi \in \Xi_H$ are evaluated in the RVEs \mathcal{Y}_ξ by the locally averaged two-scale micro-energy and micro-dissipation

$$W_\xi(\boldsymbol{\varepsilon}_H, \mathbf{v}_{\xi,h}, \mathbf{z}_{\xi,h}) = \frac{1}{|\mathcal{Y}_\xi|} \int_{\mathcal{Y}_\xi} W(\mathbf{x}, \boldsymbol{\varepsilon}_{\xi,H} + \boldsymbol{\varepsilon}(\mathbf{v}_{\xi,h}), \mathbf{z}_{\xi,h}) \, d\mathbf{x},$$

$$R_\xi(\dot{\mathbf{z}}_h) = \frac{1}{|\mathcal{Y}_\xi|} \int_{\mathcal{Y}_\xi} R(\mathbf{x}, \dot{\mathbf{z}}_{\xi,h}) \, d\mathbf{x},$$

depending on the macro-strain $\boldsymbol{\varepsilon}_{\xi,H} = \boldsymbol{\varepsilon}(\mathbf{u}_H)(\xi)$. Again, the micro-solution $\mathbf{u}_{\xi,h} = \mathbf{u}_{\xi,H} + \mathbf{v}_{\xi,h}$ is defined by the linearized macro-solution $\mathbf{u}_{\xi,H}(\mathbf{x}) = \mathbf{u}_H(\xi) + \nabla \mathbf{u}_H(\xi)(\mathbf{x} - \xi)$, meaning that by construction the micro-fluctuation is periodic and the strain of the macro-solution $\boldsymbol{\varepsilon}(\mathbf{u}_{\xi,H}) \equiv \boldsymbol{\varepsilon}_{\xi,H}$ is constant in \mathcal{Y}_ξ .

6.2 The incremental two-scale problem

Let $0 = t_0 < t_1 < \dots < t_{N_{\max}} = T$ be a time series with $\Delta t_n = t_n - t_{n-1}$. Starting with $(\mathbf{u}_H^0, \mathbf{v}_h^0, \mathbf{z}_h^0)$ we solve for $n = 1, \dots, N_{\max}$ the following incremental problems depending on the given history variable \mathbf{z}_h^{n-1} , the load functional $\ell^n = \ell(t_n)$ and the Dirichlet data $\mathbf{u}_D^n = \mathbf{u}_D(t_n)$: find a minimizer $(\mathbf{u}_H^n, \mathbf{v}_h^n, \mathbf{z}_h^n) \in V_H(\mathbf{u}_D^n) \times V_h \times Z_h$ of the two-scale incremental functional

$$\mathcal{J}_{h,n}(\mathbf{u}_H^n, \mathbf{v}_h^n, \mathbf{z}_h^n) = \mathcal{E}_H(t_n, \mathbf{u}_H^n, \mathbf{v}_h^n, \mathbf{z}_h^n) + \mathcal{R}_H(\mathbf{z}_h^n - \mathbf{z}_h^{n-1}).$$

The minimizer is determined by computing a critical point of $\mathcal{J}_{h,n}(\cdot)$. This is characterized by the nonlinear system

$$\text{Macro-Equilibrium} \quad 0 = \partial_{\mathbf{u}} \mathcal{E}_H(t_n, \mathbf{u}_H^n, \mathbf{v}_h^n, \mathbf{z}_h^n), \quad (6.1a)$$

$$\text{Micro-Equilibrium} \quad 0 = \partial_{\mathbf{v}} \mathcal{E}_H(t_n, \mathbf{u}_H^n, \mathbf{v}_h^n, \mathbf{z}_h^n), \quad (6.1b)$$

$$\text{Flow Rule} \quad 0 \in \partial_{\mathbf{z}} \mathcal{E}_H(t_n, \mathbf{u}_H^n, \mathbf{v}_h^n, \mathbf{z}_h^n) + \partial \mathcal{R}_H(\Delta \mathbf{z}_h^n). \quad (6.1c)$$

Since we consider rate-independent materials, the flow rule is 1-homogeneous satisfying $\Delta t_n \mathcal{R}((\Delta t_n)^{-1}(\mathbf{z}_h^n - \mathbf{z}_h^{n-1})) = \mathcal{R}(\mathbf{z}_h^n - \mathbf{z}_h^{n-1})$ and thus depending only on the increment $\Delta \mathbf{z}_h^n = \mathbf{z}_h^n - \mathbf{z}_h^{n-1}$.

The **Macro-Equilibrium** $0 = \partial_{\mathbf{u}} \mathcal{E}_H(t_n, \mathbf{u}_H^n, \mathbf{v}_h^n, \mathbf{z}_h^n)$ reads in variational form

$$\int_{\Xi_H} \frac{1}{|\mathcal{Y}_\xi|} \int_{\mathcal{Y}_\xi} \partial_{\boldsymbol{\varepsilon}} W(\mathbf{x}, \boldsymbol{\varepsilon}_{\xi,H}^n + \boldsymbol{\varepsilon}(\mathbf{v}_{\xi,h}^n), \mathbf{z}_{\xi,h}^n) : \boldsymbol{\varepsilon}(\delta \mathbf{u}_H) \, d\mathbf{x} = \langle \ell^n, \delta \mathbf{u}_H \rangle$$

for $\delta \mathbf{u}_H \in V_H(0)$, where $\boldsymbol{\varepsilon}_{\xi,H}^n = \boldsymbol{\varepsilon}(\mathbf{u}_H^n)(\xi)$ denotes the macro-strain. We define the micro-stress

$$\boldsymbol{\sigma}_{\xi,h}^n = \partial_{\boldsymbol{\varepsilon}} W(\mathbf{x}, \boldsymbol{\varepsilon}_{\xi,H}^n + \boldsymbol{\varepsilon}(\mathbf{v}_{\xi,h}^n), \mathbf{z}_{\xi,h}^n)$$

depending on the macro-strain and the micro-fluctuation $\mathbf{v}_{\xi,h}^n \in V_{\xi,h}$ and then by averaging in the RVE the macro-stress

$$\boldsymbol{\sigma}_{\xi,H}^n = \frac{1}{|\mathcal{Y}_\xi|} \int_{\mathcal{Y}_\xi} \boldsymbol{\sigma}_{\xi,h}^n \, d\mathbf{x},$$

which together yields the macro-equilibrium in the form

$$\int_{\Xi_H} \boldsymbol{\sigma}_{\xi,H}^n : \boldsymbol{\varepsilon}(\delta \mathbf{u}_H) = \langle \ell^n, \delta \mathbf{u}_H \rangle, \quad \delta \mathbf{u}_H \in V_H(0).$$

The **Micro-Equilibrium** $0 = \partial_{\mathbf{v}} \mathcal{E}_H(t_n, \mathbf{u}_H^n, \mathbf{v}_h^n, \mathbf{z}_h^n)$ reads in variational form

$$\frac{1}{|\mathcal{Y}_\xi|} \int_{\mathcal{Y}_\xi} \boldsymbol{\sigma}_{\xi,h}^n : \boldsymbol{\varepsilon}(\delta \mathbf{v}_{\xi,h}) \, d\mathbf{x} = 0, \quad \delta \mathbf{v}_{\xi,h} \in V_{\xi,h}.$$

The **Flow Rule** $0 \in \partial_{\mathbf{z}} \mathcal{E}_H(t_n, \mathbf{u}_H^n, \mathbf{v}_h^n, \mathbf{z}_h^n) + \partial \mathcal{R}_H(\Delta \mathbf{z}_h^n)$ determines the history variable \mathbf{z}_h^n from the macro-solution \mathbf{u}_H^n and the micro-fluctuation $\mathbf{v}_{\xi,h}^n$. It is evaluated in every integration point of the RVE \mathcal{Y}_ξ and can be expressed by duality

$$\mathbf{y}_{\xi,h}^n \in \partial R(\mathbf{x}, \Delta \mathbf{z}_{\xi,h}^n) \quad \Longleftrightarrow \quad \Delta \mathbf{z}_{\xi,h}^n \in \partial R^*(\mathbf{x}, \mathbf{y}_{\xi,h}^n)$$

depending on the conjugate variable $\mathbf{y}_{\xi,h}^n = -\partial_{\mathbf{z}} W(\mathbf{x}, \boldsymbol{\varepsilon}_{\xi,H}^n + \boldsymbol{\varepsilon}(\mathbf{v}_{\xi,h}^n), \mathbf{z}_{\xi,h}^n)$.

Altogether, this results in a coupled nonlinear system which can be solved by a generalized Newton method. This is realized by a return mapping procedure [55, 22] and determines a Newton linearization for the evaluation of a consistent tangent operator on the micro-scale. Altogether this method defines a new multi-scale tensor for every Newton step by collecting the results in the RVEs. This procedure is now studied in detail for specific examples.

For damage and plasticity, we specify the internal variables \mathbf{z} , the local energy W and the dissipation R and we derive solution methods for the nonlinear incremental problems.

6.2.1 The incremental two-scale damage problem

We specify the incremental two-scale problem (6.1) for the damage model and we derive a generalized Newton method by inserting the results in Lemma 5.2. For a given damage history d_h^{n-1} and time t_n , the incremental two-scale problem aims to compute the unique minimizer $(\mathbf{u}_H^n, \mathbf{v}_h^n, d_h^n) \in V_H(\mathbf{u}_D^n) \times V_h \times Z_h$ of the functional

$$\mathcal{J}_{h,n}(\mathbf{u}_H^n, \mathbf{v}_h^n, d_h^n) = \mathcal{E}_H(t_n, \mathbf{u}_H^n, \mathbf{v}_h^n, d_h^n) + \mathcal{R}_H(d_h^n - d_h^{n-1})$$

by solving the nonlinear system

$$0 = \partial_{\mathbf{u}} \mathcal{E}_H(t_n, \mathbf{u}_H^n, \mathbf{v}_h^n, d_h^n), \quad (6.2a)$$

$$0 = \partial_{\mathbf{v}} \mathcal{E}_H(t_n, \mathbf{u}_H^n, \mathbf{v}_h^n, d_h^n), \quad (6.2b)$$

$$0 \in \partial_d \mathcal{E}_H(t_n, \mathbf{u}_H^n, \mathbf{v}_h^n, d_h^n) + \partial \mathcal{R}_H(\Delta d_h^n). \quad (6.2c)$$

For this purpose, we define a return mapping procedure which evaluates the variational inequality (6.2c) which then allows determining a suitable Newton linearization.

The flow rule (6.2c) is evaluated at every integration point in the RVE \mathcal{Y}_ξ . Inserting $Y(\boldsymbol{\varepsilon}_{\xi,h}) = \frac{1}{2}\boldsymbol{\varepsilon}_{\xi,h} : \mathbb{C}[\boldsymbol{\varepsilon}_{\xi,h}]$, we obtain from Lemma 5.2 for the damage variable

$$d_{\xi,h,n}(\boldsymbol{\varepsilon}_{\xi,h}) = d_{\xi,h}^{n-1} + \max \{0, \Phi(Y(\boldsymbol{\varepsilon}_{\xi,h})) - d_{\xi,h}^{n-1}\}$$

and the stress response $\boldsymbol{\sigma}_{\xi,h}^n = \boldsymbol{\sigma}_{\xi,h,n}(\boldsymbol{\varepsilon}_{\xi,h}^n)$ with

$$\boldsymbol{\sigma}_{\xi,h,n}(\boldsymbol{\varepsilon}_{\xi,h}) = (1 - d_{\xi,h,n}(\boldsymbol{\varepsilon}_{\xi,h}))\mathbb{C}[\boldsymbol{\varepsilon}_{\xi,h}].$$

Inserting this result in (6.2) yields the reduced nonlinear problem to compute a critical point $(\mathbf{u}_H^n, \mathbf{v}_h^n) \in V_H(\mathbf{u}_D^n) \times V_h$ of

$$\begin{aligned} \langle \mathcal{F}_{h,n}(\mathbf{u}_H, \mathbf{v}_h), (\delta \mathbf{u}_H, \delta \mathbf{v}_h) \rangle = \\ \int_{\Xi_H} \frac{1}{|\mathcal{Y}_\xi|} \int_{\mathcal{Y}_\xi} \boldsymbol{\sigma}_{\xi,h,n}(\boldsymbol{\varepsilon}_{\xi,h}) : (\boldsymbol{\varepsilon}(\delta \mathbf{u}_H) + \boldsymbol{\varepsilon}(\delta \mathbf{v}_{\xi,h})) \, d\mathbf{x} - \langle \ell^n, \delta \mathbf{u}_H \rangle \end{aligned}$$

for all $(\delta \mathbf{u}_H, \delta \mathbf{v}_h) \in V_H(\mathbf{0}) \times V_h$. The consistent tangent operator

$$\begin{aligned} \mathbb{C}_{\xi,h,n}(\boldsymbol{\varepsilon}_{\xi,h}) = (1 - d_{\xi,h,n}(\boldsymbol{\varepsilon}_{\xi,h}))\mathbb{C} \\ - \operatorname{sgn} \left(\max \{0, \Phi(Y(\boldsymbol{\varepsilon}_{\xi,h})) - d_{\xi,h}^{n-1}\} \right) \Phi'(Y(\boldsymbol{\varepsilon}_{\xi,h}))\mathbb{C}[\boldsymbol{\varepsilon}_{\xi,h}] \otimes \mathbb{C}[\boldsymbol{\varepsilon}_{\xi,h}] \end{aligned}$$

yields a Newton linearization

$$\begin{aligned} \langle \mathcal{F}'_{h,n}(\mathbf{u}_H, \mathbf{v}_h)(\Delta \mathbf{u}_H, \Delta \mathbf{v}_h), (\delta \mathbf{u}_H, \delta \mathbf{v}_h) \rangle = \\ \int_{\Xi_H} \frac{1}{|\mathcal{Y}_\xi|} \int_{\mathcal{Y}_\xi} \mathbb{C}_{\xi,h,n}(\boldsymbol{\varepsilon}_{\xi,h})[\boldsymbol{\varepsilon}(\Delta \mathbf{u}_H) + \boldsymbol{\varepsilon}(\Delta \mathbf{v}_{\xi,h})] : (\boldsymbol{\varepsilon}(\delta \mathbf{u}_H) + \boldsymbol{\varepsilon}(\delta \mathbf{v}_{\xi,h})) \, d\mathbf{x} \end{aligned}$$

for $(\Delta \mathbf{u}_H, \Delta \mathbf{v}_h), (\delta \mathbf{u}_H, \delta \mathbf{v}_h) \in V_H(\mathbf{0}) \times V_h$.

The two-scale residual $\mathcal{F}_{h,n}$ and its linearization $\mathcal{F}'_{h,n}$ allows for the construction of a generalized Newton method of the incremental problem. This can be formulated as follows: starting with $(\mathbf{u}_H^{n,0}, \mathbf{v}_h^{n,0}) \in V_H(\mathbf{u}_D^n) \times V_h$, for $k = 1, 2, \dots$ the Newton increment $(\Delta \mathbf{u}_H^{n,k}, \Delta \mathbf{v}_h^{n,k}) \in V_H(\mathbf{0}) \times V_h$ is determined by solving

$$\begin{aligned} \langle \mathcal{F}'_{h,n}(\mathbf{u}_H^{n,k-1}, \mathbf{v}_h^{n,k-1})(\Delta \mathbf{u}_H^{n,k}, \Delta \mathbf{v}_h^{n,k}), (\delta \mathbf{u}_H, \delta \mathbf{v}_h) \rangle = \\ - \langle \mathcal{F}_{h,n}(\mathbf{u}_H^{n,k-1}, \mathbf{v}_h^{n,k-1}), (\delta \mathbf{u}_H, \delta \mathbf{v}_h) \rangle \end{aligned}$$

for all $(\delta \mathbf{u}_H, \delta \mathbf{v}_h) \in V_H(\mathbf{0}) \times V_h$. The next iteration is given by

$$(\mathbf{u}_H^{n,k}, \mathbf{v}_h^{n,k}) = (\mathbf{u}_H^{n,k-1}, \mathbf{v}_h^{n,k-1}) + s_{n,k}(\Delta \mathbf{u}_H^{n,k}, \Delta \mathbf{v}_h^{n,k}).$$

with a suitable damping parameter $s_{n,k} \in (0, 1]$. The iteration stops, if the residual $\mathcal{F}_{h,n}(\mathbf{u}_H^{n,k}, \mathbf{v}_h^{n,k})$ is small enough.

It turns out that this monolithic Newton method for the combined two-scale problem is not efficient, since for every Newton step a full micro-macro problem has to be solved. Therefore, we use an alternative approach to compute the Newton increment first on the micro-scale and then on the macro-scale.

In the first time step $n = 0$, we compute for every $\xi \in \Xi_h^{\text{active}}$ the micro-fluctuations $\mathbf{w}_{\xi,h,1}^0, \dots, \mathbf{w}_{\xi,h,6}^0 \in V_{\xi,h}$ with respect to the basis $\boldsymbol{\eta}_1, \dots, \boldsymbol{\eta}_6$ solving (3.13).

In every time step $n \geq 1$ we set $\mathbf{w}_{\xi,h,l}^{n,0} = \mathbf{w}_{\xi,h,l}^{n-1}$ and we start with selecting $\mathbf{u}_H^{n,0} \in V_H(\mathbf{u}_D^n)$. For every macro-Newton step $k \geq 1$ and for every $\xi \in \Xi_h$, the micro-residual at $\boldsymbol{\varepsilon}_{\xi,H}^{n,k-1} = \boldsymbol{\varepsilon}(\mathbf{u}_H^{n,k-1})(\xi)$ is given by

$$\langle \mathcal{F}_{\xi,h,n,k}(\mathbf{v}_{\xi,h}), \delta \mathbf{v}_{\xi,h} \rangle = \int_{\mathcal{Y}_\xi} \boldsymbol{\sigma}_{\xi,h,n}(\boldsymbol{\varepsilon}_{\xi,H}^{n,k-1} + \boldsymbol{\varepsilon}(\mathbf{v}_{\xi,h})) : \boldsymbol{\varepsilon}(\delta \mathbf{v}_{\xi,h}) \, d\mathbf{x}.$$

The micro-fluctuation $\mathbf{v}_{\xi,h}^{n,k}$ is computed by a micro-Newton method solving approximately the nonlinear problem $\mathcal{F}_{\xi,h,n,k}(\mathbf{v}_{\xi,h}) = 0$. Starting with

$$\mathbf{v}_{\xi,h}^{n,k,0} = \sum_{j=1}^6 \left(\boldsymbol{\varepsilon}_{\xi,H}^{n,k-1} : \boldsymbol{\eta}_j \right) \mathbf{w}_{\xi,h,j}^{n,k-1},$$

we compute for $m = 1, 2, \dots$ the strain $\boldsymbol{\varepsilon}_{\xi,h}^{n,k,m-1} = \boldsymbol{\varepsilon}_{\xi,H}^{n,k-1} + \boldsymbol{\varepsilon}(\mathbf{v}_{\xi,h}^{n,k,m-1})$, the stress response $\boldsymbol{\sigma}_{\xi,h}^{n,k,m-1} = \boldsymbol{\sigma}_{\xi,h,n}(\boldsymbol{\varepsilon}_{\xi,h}^{n,k,m-1})$, the consistent tangent operator $\mathbb{C}_{\xi,h}^{n,k,m-1} = \mathbb{C}_{\xi,h,n}(\boldsymbol{\varepsilon}_{\xi,h}^{n,k,m-1})$ and then the increment $\Delta \mathbf{v}_{\xi,h}^{n,k,m} \in V_{\xi,h}$ by solving

$$\int_{\mathcal{Y}_\xi} \mathbb{C}_{\xi,h}^{n,k,m-1}[\boldsymbol{\varepsilon}(\Delta \mathbf{v}_{\xi,h}^{n,k,m})] : \boldsymbol{\varepsilon}(\delta \mathbf{v}_{\xi,h}) \, d\mathbf{x} = - \int_{\mathcal{Y}_\xi} \boldsymbol{\sigma}_{\xi,h}^{n,k,m-1} : \boldsymbol{\varepsilon}(\delta \mathbf{v}_{\xi,h}) \, d\mathbf{x}$$

for all $\delta \mathbf{v}_{\xi,h} \in V_{\xi,h}$; then set $\mathbf{v}_h^{n,k,m} = \mathbf{v}_h^{n,k,m-1} + s_{\xi,n,k,m} \Delta \mathbf{v}_h^{n,k,m}$ with $s_{\xi,n,k,m} \in (0, 1]$. If the micro-residual is small enough, we set $\mathbf{v}_{\xi,h}^{n,k} = \mathbf{v}_{\xi,h}^{n,k,m}$, $\boldsymbol{\sigma}_{\xi,h}^{n,k} = \boldsymbol{\sigma}_{\xi,h}^{n,k,m}$,

$$\boldsymbol{\sigma}_{\xi,H}^{n,k} = \frac{1}{|\mathcal{Y}_\xi|} \int_{\mathcal{Y}_\xi} \boldsymbol{\sigma}_{\xi,h}^{n,k} \, d\mathbf{x}$$

and $\mathbb{C}_{\xi,h}^{n,k} = \mathbb{C}_{\xi,h}^{n,k,m}$. If $\mathbf{v}_{\xi,h}^{n,k}$ is sufficiently close to the previous iterate, we use $\mathbf{w}_{\xi,h,l}^{n,k} = \mathbf{w}_{\xi,h,l}^{n,k-1}$ and $\mathbb{C}_{\xi,H}^{n,k} = \mathbb{C}_{\xi,H}^{n,k-1}$ from the previous iteration, otherwise we compute $\mathbf{w}_{\xi,h,l}^{n,k} \in V_{\xi,h}$ solving

$$\frac{1}{|\mathcal{Y}_\xi|} \int_{\mathcal{Y}_\xi} \mathbb{C}(\mathbf{x})[\boldsymbol{\eta}_l + \boldsymbol{\varepsilon}(\mathbf{w}_{\xi,h,l})] : \boldsymbol{\varepsilon}(\delta \mathbf{v}_{\xi,h}) \, d\mathbf{x} = 0, \quad \delta \mathbf{v}_{\xi,h} \in V_{\xi,h}$$

for $l = 1, \dots, 6$ and the multiscale tensor

$$\mathbb{C}_{\xi, H}^{n, k} = \sum_{l, j=1}^6 \left(\frac{1}{|\mathcal{Y}_\xi|} \int_{\mathcal{Y}_\xi} \mathbb{C}_{\xi, h}^{n, k} [\boldsymbol{\eta}_l + \boldsymbol{\varepsilon}(\mathbf{w}_{\xi, h, l})] : \boldsymbol{\eta}_j \, d\mathbf{x} \right) \boldsymbol{\eta}_l \otimes \boldsymbol{\eta}_j.$$

The macro-update $\Delta \mathbf{u}_H^{n, k} \in V_H(\mathbf{0})$ is computed by solving

$$\int_{\Xi_H} \mathbb{C}_{\xi, H}^{n, k} [\boldsymbol{\varepsilon}(\Delta \mathbf{u}_H^{n, k})] : \boldsymbol{\varepsilon}(\delta \mathbf{u}_H) = - \int_{\Xi_H} \boldsymbol{\sigma}_{\xi, H}^{n, k} : \boldsymbol{\varepsilon}(\delta \mathbf{u}_H) + \langle \ell^n, \delta \mathbf{u}_H \rangle$$

for all $\delta \mathbf{u}_H \in V_H(\mathbf{0})$; then set $\mathbf{u}_H^{n, k} = \mathbf{u}_h^{n, k-1} + s_{n, k} \Delta \mathbf{u}_H^{n, k}$ with $s_{n, k} \in (0, 1]$. If the macro-residual is small enough, we set $\mathbf{u}_H^n = \mathbf{u}_H^{n, k}$, $\mathbf{v}_{\xi, h}^n = \mathbf{v}_{\xi, h}^{n, k}$, update the damage variable $d_{\xi, h}^n = d_{\xi, h}^{n-1} + \max \{0, \Phi(Y_\xi(\boldsymbol{\varepsilon}_{\xi, h}^n)) - d_{\xi, h}^{n-1}\}$ and then proceed to the next time step.

6.2.2 The incremental two-scale elasto-plasticity model

Specifying the incremental two-scale problem (6.1) for elasto-plasticity yields

$$0 = \partial_{\mathbf{u}} \mathcal{E}(t_n, \mathbf{u}_H^n, \mathbf{v}_h^n, \boldsymbol{\varepsilon}_{p, h}^n, r_h^n), \quad (6.3a)$$

$$0 = \partial_{\mathbf{v}} \mathcal{E}(t_n, \mathbf{u}_H^n, \mathbf{v}_h^n, \boldsymbol{\varepsilon}_{p, h}^n, r_h^n), \quad (6.3b)$$

$$0 \in \partial_{(\boldsymbol{\varepsilon}_p, r)} \mathcal{E}(t_n, \mathbf{u}_H^n, \mathbf{v}_h^n, \boldsymbol{\varepsilon}_{p, h}^n, r_h^n) + \partial \mathcal{R}(\Delta \boldsymbol{\varepsilon}_{p, h}^n, \Delta r_h^n). \quad (6.3c)$$

For a given material history $(\boldsymbol{\varepsilon}_{p, \xi, h}^{n-1}, r_{\xi, h}^{n-1})$ and a strain $\boldsymbol{\varepsilon}_{\xi, h}^n = \boldsymbol{\varepsilon}(\mathbf{u}_H^n)(\xi) + \boldsymbol{\varepsilon}(\mathbf{v}_{\xi, h}^n)$, the stress $\boldsymbol{\sigma}_{\xi, h}^n = \boldsymbol{\sigma}_{\xi, h, n}(\boldsymbol{\varepsilon}_{\xi, h}^n)$ is determined from the flow rule, cf. Lemma 5.3. Therefore, we define the relative trial stress

$$\boldsymbol{\alpha}_{\xi, h, n}^{\text{tr}}(\boldsymbol{\varepsilon}_{\xi, h}) = 2\mu \operatorname{dev} \boldsymbol{\varepsilon}_{\xi, h} - (2\mu + K) \boldsymbol{\varepsilon}_{p, \xi, h}^{n-1},$$

and the flow function

$$F_{\xi, h, n}(\boldsymbol{\varepsilon}_{\xi, h}, \Delta r_{\xi, h}) = |\boldsymbol{\alpha}_{\xi, h, n}^{\text{tr}}(\boldsymbol{\varepsilon}_{\xi, h})| - (2\mu + K) \Delta r_{\xi, h} - \Psi(r_{\xi, h}^{n-1} + \Delta r_{\xi, h}).$$

If $F_{\xi, h, n}(\boldsymbol{\varepsilon}_{\xi, h}, 0) \leq 0$, we set $\Delta r_{\xi, h, n}(\boldsymbol{\varepsilon}_{\xi, h}) = 0$, otherwise the increment is defined by solving the nonlinear problem $F_{\xi, h, n}(\boldsymbol{\varepsilon}_{\xi, h}, \Delta r_{\xi, h, n}(\boldsymbol{\varepsilon}_{\xi, h})) = 0$. This defines the update

$$r_{\xi, h, n}(\boldsymbol{\varepsilon}_{\xi, h}) = r_{\xi, h}^{n-1} + \Delta r_{\xi, h, n}(\boldsymbol{\varepsilon}_{\xi, h})$$

and the response for the plastic strain and the stress, and the consistent tangent operator

$$\boldsymbol{\varepsilon}_{p, \xi, h}(\boldsymbol{\varepsilon}_{\xi, h}) = \boldsymbol{\varepsilon}_{p, \xi, h}^{n-1} + \Delta r_{\xi, h, n}(\boldsymbol{\varepsilon}_{\xi, h}) \frac{\boldsymbol{\alpha}_{\xi, h, n}^{\text{tr}}(\boldsymbol{\varepsilon}_{\xi, h})}{|\boldsymbol{\alpha}_{\xi, h, n}^{\text{tr}}(\boldsymbol{\varepsilon}_{\xi, h})|},$$

$$\boldsymbol{\sigma}_{\xi, h, n}(\boldsymbol{\varepsilon}_{\xi, h}) = \mathbb{C}[\boldsymbol{\varepsilon}_{\xi, h} - \boldsymbol{\varepsilon}_{p, \xi, h}(\boldsymbol{\varepsilon}_{\xi, h})],$$

$$\begin{aligned} \mathbb{C}_{\xi,h,n}(\boldsymbol{\varepsilon}_{\xi,h}) &= \mathbb{C} - \frac{4\mu^2 \Delta r_{\xi,h,n}(\boldsymbol{\varepsilon}_{\xi,h})}{|\boldsymbol{\alpha}_{\xi,h,n}(\boldsymbol{\varepsilon}_{\xi,h})|} \left(\text{dev} - \frac{\boldsymbol{\alpha}_{\xi,h,n}(\boldsymbol{\varepsilon}_{\xi,h})}{|\boldsymbol{\alpha}_{\xi,h,n}(\boldsymbol{\varepsilon}_{\xi,h})|} \otimes \frac{\boldsymbol{\alpha}_{\xi,h,n}(\boldsymbol{\varepsilon}_{\xi,h})}{|\boldsymbol{\alpha}_{\xi,h,n}(\boldsymbol{\varepsilon}_{\xi,h})|} \right) \\ &\quad - \frac{4\mu^2}{2\mu + K + \Psi'(r_{\xi,h,n}(\boldsymbol{\varepsilon}_{\xi,h}))} \frac{\boldsymbol{\alpha}_{\xi,h,n}(\boldsymbol{\varepsilon}_{\xi,h})}{|\boldsymbol{\alpha}_{\xi,h,n}(\boldsymbol{\varepsilon}_{\xi,h})|} \otimes \frac{\boldsymbol{\alpha}_{\xi,h,n}(\boldsymbol{\varepsilon}_{\xi,h})}{|\boldsymbol{\alpha}_{\xi,h,n}(\boldsymbol{\varepsilon}_{\xi,h})|}. \end{aligned}$$

Now, the residual, $\mathcal{F}_{n,h}$, the linearization $\mathcal{F}'_{n,h}$, and the generalized Newton method for the macro-problem can be defined as in Section 5.1.1.

6.2.3 The incremental two-scale elasto-plastic damage model

We specify the incremental two-scale problem (6.1) for elasto-plasticity coupled with damage by

$$0 = \partial_{\mathbf{u}} \mathcal{E}_H(t_n, \mathbf{u}_H^n, \mathbf{v}_h^n, d_h^n, \boldsymbol{\varepsilon}_{p,h}^n, r_h^n), \quad (6.4a)$$

$$0 = \partial_{\mathbf{v}} \mathcal{E}_H(t_n, \mathbf{u}_H^n, \mathbf{v}_h^n, d_h^n, \boldsymbol{\varepsilon}_{p,h}^n, r_h^n), \quad (6.4b)$$

$$0 \in \partial_{(d,\boldsymbol{\varepsilon}_p,r)} \mathcal{E}_H(t_n, \mathbf{u}_H^n, \mathbf{v}_h^n, d_h^n, \boldsymbol{\varepsilon}_{p,h}^n, r_h^n) + \partial \mathcal{R}_H(\Delta d_h^n, \Delta \boldsymbol{\varepsilon}_{p,h}^n, \Delta r_h^n). \quad (6.4c)$$

For a given material history $(d_{\xi,h}^{n-1}, \boldsymbol{\varepsilon}_{p,\xi,h}^{n-1}, r_{\xi,h}^{n-1})$ and a strain $\boldsymbol{\varepsilon}_{\xi,h}^n = \boldsymbol{\varepsilon}(\mathbf{u}_H^n)(\xi) + \boldsymbol{\varepsilon}(\mathbf{v}_h^n)$, the stress $\boldsymbol{\sigma}_{\xi,h}^n = \boldsymbol{\sigma}_{\xi,h,n}(\boldsymbol{\varepsilon}_{\xi,h}^n)$ is determined from the flow rule, cf. Lemma 5.4. Therefore, the plastic strain increment $\Delta \boldsymbol{\varepsilon}_{p,\xi,h,n}$ is determined by the update

$$r_{\xi,h}^n = r_{\xi,h}^{n-1} + \Delta r_{\xi,h,n},$$

which can be evaluated independently from the damage variable by the 1-homogeneous dissipation functional as in Section 5.1.2. This depends on $Y(\boldsymbol{\varepsilon}_{\xi,h}^n) = W_{\text{elastic}}(\boldsymbol{\varepsilon}_{\xi,h}^n - \boldsymbol{\varepsilon}_{p,\xi,h}^{n-1} - \Delta \boldsymbol{\varepsilon}_{p,\xi,h,n})$, and the damage variable

$$d_{\xi,h,n}(\boldsymbol{\varepsilon}_{\xi,h}^n) = d_{\xi,h}^{n-1} + \max\{0, \Phi(Y(\boldsymbol{\varepsilon}_{\xi,h}^n) - d_{\xi,h}^{n-1})\}$$

is computed as in Section 5.1.1. Now, this defines the incremental response of the stress and the consistent tangent operator

$$\begin{aligned} \boldsymbol{\sigma}_{\xi,h,n}(\boldsymbol{\varepsilon}_{\xi,h}^n) &= (1 - d_{\xi,h,n}(\boldsymbol{\varepsilon}_{\xi,h}^n)) \mathbb{C}[\boldsymbol{\varepsilon}_{\xi,h}^n - \boldsymbol{\varepsilon}_{p,\xi,h,n}(\boldsymbol{\varepsilon}_{\xi,h}^n)], \\ \mathbb{C}_{\xi,h,n}(\boldsymbol{\varepsilon}_{\xi,h}^n) &= (1 - d_{\xi,h,n}(\boldsymbol{\varepsilon}_{\xi,h}^n)) \mathbb{C}_{\xi,h,n}^{\text{plastic}}(\boldsymbol{\varepsilon}_{\xi,h}^n) \\ &\quad - \text{sgn}\left(\max\{0, \Phi(Y(\boldsymbol{\varepsilon}_{\xi,h}^n)) - d_{\xi,h}^{n-1}\}\right) \mathbb{C}[\boldsymbol{\varepsilon}_{\xi,h}^n - \boldsymbol{\varepsilon}_{p,\xi,h,n}(\boldsymbol{\varepsilon}_{\xi,h}^n)] \otimes \mathbb{C}[\boldsymbol{\varepsilon}_{\xi,h}^n] \end{aligned}$$

with

$$\begin{aligned} \mathbb{C}_{\xi,h,n}^{\text{plastic}}(\boldsymbol{\varepsilon}_{\xi,h}^n) &= \mathbb{C} - \frac{4\mu^2 \Delta r_{\xi,h}^n}{|\boldsymbol{\alpha}_{\xi,h,n}^{\text{tr}}(\boldsymbol{\varepsilon}_{\xi,h}^n)|} \left(\text{dev} - \frac{\boldsymbol{\alpha}_{\xi,h,n}^{\text{tr}}(\boldsymbol{\varepsilon}_{\xi,h}^n)}{|\boldsymbol{\alpha}_{\xi,h,n}^{\text{tr}}(\boldsymbol{\varepsilon}_{\xi,h}^n)|} \otimes \frac{\boldsymbol{\alpha}_{\xi,h,n}^{\text{tr}}(\boldsymbol{\varepsilon}_{\xi,h}^n)}{|\boldsymbol{\alpha}_{\xi,h,n}^{\text{tr}}(\boldsymbol{\varepsilon}_{\xi,h}^n)|} \right) \\ &\quad - \frac{4\mu^2}{2\mu + K + \Psi'(r_{\xi,h,n}(\boldsymbol{\varepsilon}_{\xi,h}^n))} \frac{\boldsymbol{\alpha}_{\xi,h,n}^{\text{tr}}(\boldsymbol{\varepsilon}_{\xi,h}^n)}{|\boldsymbol{\alpha}_{\xi,h,n}^{\text{tr}}(\boldsymbol{\varepsilon}_{\xi,h}^n)|} \otimes \frac{\boldsymbol{\alpha}_{\xi,h,n}^{\text{tr}}(\boldsymbol{\varepsilon}_{\xi,h}^n)}{|\boldsymbol{\alpha}_{\xi,h,n}^{\text{tr}}(\boldsymbol{\varepsilon}_{\xi,h}^n)|}. \end{aligned}$$

This is now inserted in the nonlinear iteration to solve the incremental problem (6.1) for the model combining damage and elasto-plasticity.

6.3 The parallel nonlinear two-scale algorithm

We extend the parallel algorithm from Section 3.2 to inelastic applications. Every Newton iteration in the incremental problem has the structure of the linear two-scale model, provided that the residual and the consistent tangent is evaluated in every RVE. For a suitable and precise material response in the inelastic material zone a complete inelastic computation has to be performed in order to determine a new effective response. Stability requirements for the evaluation of the internal variable by the subdifferentiable flow rule enforces implicit time integration schemes. This leads to a semi-smooth Newton approach for each inelastic material point.

The full algorithm uses a preprocessing step for the initialization of the elastic responses and is realized in three loops (see Figure 6.1 for an overview): the outer loop for the time stepping, the loop for the Newton iteration for the macro-problem for every incremental problem, and in the inner loop the Newton iterations for the micro-problem for every RVE evaluating the local stress response.

Together, the algorithm is described in detail in the following:

- T0) For all points $\xi \in \Xi_H$ with representative microstructure compute the micro-fluctuations $\mathbf{w}_{\xi,h,1}^0, \dots, \mathbf{w}_{\xi,h,6}^0 \in V_{\xi,h}$ in parallel, by solving

$$\int_{\mathcal{Y}_\xi} \mathbb{C}(\mathbf{x})[\boldsymbol{\eta}_l + \boldsymbol{\varepsilon}(\mathbf{w}_{\xi,h,l}^0)] : \boldsymbol{\varepsilon}(\delta \mathbf{v}_{\xi,h}) \, d\mathbf{x} = 0, \quad \delta \mathbf{v}_{\xi,h} \in V_{\xi,h}.$$

Then, evaluate the local contributions of the elastic multiscale tensor

$$\mathbb{C}_{\xi,H}^{0,p} = \sum_{l,j=1}^6 \left(\frac{1}{|\mathcal{Y}_\xi|} \int_{\mathcal{Y}_\xi} \mathbb{C}(\mathbf{x})[\boldsymbol{\eta}_l + \boldsymbol{\varepsilon}(\mathbf{w}_{\xi,h,l}^{0,p})] : \boldsymbol{\eta}_j \, d\mathbf{x} \right) \boldsymbol{\eta}_l \otimes \boldsymbol{\eta}_j, \quad p \in \mathcal{P},$$

and collect the full multiscale tensor $\mathbb{C}_{\xi,H}^0$ on process q with $\xi \in \Xi_H \cap \Omega^q$.

Set $\mathbf{z}_h^0 = \mathbf{0}$, $t_0 = 0$, and $n = 1$.

- T1) For given history \mathbf{z}_h^{n-1} and time increment $\Delta t_n \in (0, T - t_{n-1})$ set $t_n = t_{n-1} + \Delta t_n$ and compute the following steps:

- N0) Set $\mathbf{u}_H^{n,0} = \mathbf{u}_H^{n-1}$, $\mathbf{z}_{\xi,h}^{n,0} = \mathbf{z}_{\xi,h}^{n-1}$, $\mathbb{C}_{\xi,h}^{n,0} = \mathbb{C}_{\xi,h}^{n-1}$, $\mathbf{w}_{\xi,h,l}^{n,0} = \mathbf{w}_{\xi,h,l}^{n-1}$, and $k = 1$.
Set the Dirichlet data $\mathbf{u}_H^{n,0}(\mathbf{x}) = \mathbf{u}_D(\mathbf{x}, t_n)$ on all nodal points $\mathbf{x} \in \partial\Omega_D$ of the macro-space V_H .

- N1) Evaluate the macro-strain $\boldsymbol{\varepsilon}_H^{n,k} = \boldsymbol{\varepsilon}(\mathbf{u}_H^{n,k})$ and compute the micro-fluctuation sequentially for all $\xi \in \Xi$ by the following steps:

S0) On process q with $\xi \in \Xi_H \cap \Omega^q$ evaluate $\boldsymbol{\varepsilon}_{\xi,H}^{n,k} = \boldsymbol{\varepsilon}(\mathbf{u}_H^{n,k})(\xi)$ and send $\boldsymbol{\varepsilon}_{\xi,H}^{n,k}$ to all processes.

Set $\mathbf{v}_{\xi,h}^{n,k,0} = \sum_l (\boldsymbol{\varepsilon}_{\xi,H}^{n,k} : \boldsymbol{\eta}_l) \mathbf{w}_{\xi,h,l}^{n,k-1}$, $\mathbb{C}_{\xi,h}^{n,k,0} = \mathbb{C}_{\xi,h}^{n,k}$, and $m = 0$.

S1) Evaluate the micro-strain $\boldsymbol{\varepsilon}_{\xi,h}^{n,k,m} = \boldsymbol{\varepsilon}_{\xi,H}^{n,k} + \boldsymbol{\varepsilon}(\mathbf{v}_{\xi,h}^{n,k,m})$, the nonlinear material response $\mathbf{z}_{\xi,h}^{n,k,m} = \mathbf{z}_{\xi,h,n}(\boldsymbol{\varepsilon}_{\xi,h}^{n,k,m})$, the micro-stress

$$\boldsymbol{\sigma}_{\xi,h}^{n,k,m} = \partial_{\boldsymbol{\varepsilon}} W(\boldsymbol{\varepsilon}_{\xi,h}^{n,k,m}, \mathbf{z}_{\xi,h}^{n,k,m}),$$

and the micro-residual

$$\langle \mathcal{F}_h(\mathbf{v}_{\xi,h}^{n,k,m}), \delta \mathbf{v}_{\xi,h} \rangle = \int_{\mathcal{Y}_{\xi}} \boldsymbol{\sigma}_{\xi,h}^{n,k,m} : \boldsymbol{\varepsilon}(\delta \mathbf{v}_{\xi,h}) \, d\mathbf{x}, \quad \delta \mathbf{v}_{\xi,h} \in V_{\xi,h}.$$

S2) If the micro-residual $\mathcal{F}_h(\mathbf{v}_{\xi,h}^{n,k,m})$ is small enough, set $\boldsymbol{\sigma}_{\xi,h}^{n,k} = \boldsymbol{\sigma}_{\xi,h}^{n,k,m}$ and $\mathbb{C}_{\xi,h}^{n,k} = \mathbb{C}_{\xi,h}^{n,k,m}$, and go to N2).

S3) If $m = m_{\max}$, reduce Δt_n and go to T1).

S4) Evaluate the consistent tangent operator $\mathbb{C}_{\xi,h}^{n,k,m} = \mathbb{C}_{\xi,h,n}(\boldsymbol{\varepsilon}_{\xi,h}^{n,k,m})$ and compute $\Delta \mathbf{v}_{\xi,h}^{n,k,m} \in V_{\xi,h}$ by solving

$$\int_{\mathcal{Y}_{\xi}} \mathbb{C}_{\xi,h}^{n,k,m}[\boldsymbol{\varepsilon}(\Delta \mathbf{v}_{\xi,h}^{n,k,m})] : \boldsymbol{\varepsilon}(\delta \mathbf{v}_{\xi,h}) \, d\mathbf{x} = -\langle \mathcal{F}_h(\mathbf{v}_{\xi,h}^{n,k,m}), \delta \mathbf{v}_{\xi,h} \rangle$$

in parallel for all $\delta \mathbf{v}_{\xi,h} \in V_{\xi,h}$.

S5) Select a damping parameter $s_{n,k,m} \in (0, 1]$ and set

$$\mathbf{v}_{\xi,h}^{n,k,m+1} = \mathbf{v}_{\xi,h}^{n,k,m} + s_{n,k,m} \Delta \mathbf{v}_{\xi,h}^{n,k,m}.$$

If $s_{n,k,m} \leq s_{\min}$, reduce Δt_n and go to T1).

S6) Set $m := m + 1$ and go to S1).

N2) Evaluate the local contributions of the macro-stress

$$\boldsymbol{\sigma}_{\xi,H}^{n,k,p} = \frac{1}{|\mathcal{Y}_{\xi}|} \int_{\mathcal{Y}_{\xi}^p} \boldsymbol{\sigma}_{\xi,h}^{n,k,p} \, d\mathbf{x}, \quad p \in \mathcal{P},$$

and collect the full macro-stress $\boldsymbol{\sigma}_{\xi,H}^{n,k}$ on process q with $\xi \in \Xi_H \cap \Omega^p$.

Then, compute the macro-residual

$$\langle \mathcal{F}_H(\mathbf{u}_H^{n,k}), \delta \mathbf{u}_H \rangle = \int_{\Xi_H} \boldsymbol{\sigma}_{\xi,H}^{n,k} : \boldsymbol{\varepsilon}(\delta \mathbf{u}_H) - \langle \ell^n, \delta \mathbf{u}_H \rangle, \quad \delta \mathbf{u}_H \in V_H(0).$$

N3) If the macro-residual is small enough, set $\mathbf{u}_H^n = \mathbf{u}_H^{n,k}$, $\mathbf{z}_h^n = \mathbf{z}_h^{n,k}$, $n := n + 1$, and go to T1).

N4) If $k = k_{\max}$, reduce Δt_n and go to T1).

N5) Compute the micro-fluctuations $\mathbf{w}_{\xi,h,1}^{n,k}, \dots, \mathbf{w}_{\xi,h,6}^{n,k} \in V_{\xi,h}$ in parallel, by solving

$$\int_{\mathcal{Y}_\xi} \mathbb{C}_{\xi,h}^{n,k} [\boldsymbol{\eta}_l + \boldsymbol{\varepsilon}(\mathbf{w}_{\xi,h,l}^{n,k})] : \boldsymbol{\varepsilon}(\delta \mathbf{v}_{\xi,h}) \, d\mathbf{x} = 0, \quad \delta \mathbf{v}_{\xi,h} \in V_{\xi,h}.$$

Then, evaluate the local contributions of the inelastic multiscale tensor

$$\mathbb{C}_{\xi,H}^{n,k,p} = \sum_{l,j=1}^6 \left(\frac{1}{|\mathcal{Y}_\xi|} \int_{\mathcal{Y}_\xi} \mathbb{C}_{\xi,h}^{n,k} [\boldsymbol{\eta}_l + \boldsymbol{\varepsilon}(\mathbf{w}_{\xi,h,l}^{n,k,p})] : \boldsymbol{\eta}_j \, d\mathbf{x} \right) \boldsymbol{\eta}_l \otimes \boldsymbol{\eta}_j, \quad p \in \mathcal{P},$$

and collect the full inelastic multiscale tensor $\mathbb{C}_{\xi,H}^{n,k}$ on process q with $\xi \in \Xi_H \cap \Omega^q$.

N6) Compute $\Delta \mathbf{u}_H^{n,k} \in V_H(0)$ in parallel, by solving

$$\int_{\Xi_H} \mathbb{C}_{\xi,H}^{n,k} [\boldsymbol{\varepsilon}(\Delta \mathbf{u}_H^{n,k})] : \boldsymbol{\varepsilon}(\delta \mathbf{u}_H) = -\langle \mathcal{F}_H(\mathbf{u}_H^{n,k}), \delta \mathbf{u}_H \rangle, \quad \delta \mathbf{u}_H \in V_H(0).$$

N7) Select a damping parameter $s_{n,k} \in (0, 1]$ and set

$$\mathbf{u}_H^{n,k+1} = \mathbf{u}_H^{n,k} + s_{n,k} \Delta \mathbf{u}_H^{n,k}.$$

If $s_{n,k} \leq s_{\min}$ reduce Δt_n and go to T1).

N8) Set $k := k + 1$ and go to N1).

The damping factors in S5) and N7) are chosen by a line search strategy such that the next residual is decreasing. The collecting routines in T0), N2) and N5) are achieved by summation of the domain decomposed contributions. For more efficiency the pre-processing in T0) is realized only for different microstructures, cf. Section 3.2.6.

The flow chart in Figure 6.1 presents an overview of running processes of the algorithm on the macro-scale (other boxes) and the micro-scale (turquoise boxes). For an increased efficiency in the steps T0), S4), N5) and N6) a parallel multigrid method with a highly scalable coarse grid solver is used to compute (blue lettering) the micro-fluctuations $\mathbf{w}_{\xi,h,1}^{n,k}, \dots, \mathbf{w}_{\xi,h,6}^{n,k}$, the micro-update $\Delta \mathbf{v}_{\xi,h}^{n,k,m}$, and the macro-update $\Delta \mathbf{u}_H^{n,k}$. Broadcast and collective communication with synchronization techniques are used in step S0), N2) and N5) for the scale transition (red lettering) of the parallelized macro-strain $\boldsymbol{\varepsilon}_{\xi,H}^{n,k}$, macro-stress $\boldsymbol{\sigma}_{\xi,H}^{n,k}$ and two-scale tensor $\mathbb{C}_{\xi,H}^{n,k}$. A flexible and modular two-scale data structure for a parallel realization of various nonlinear material models and reduced storage techniques is described in detail in Section 8.2.

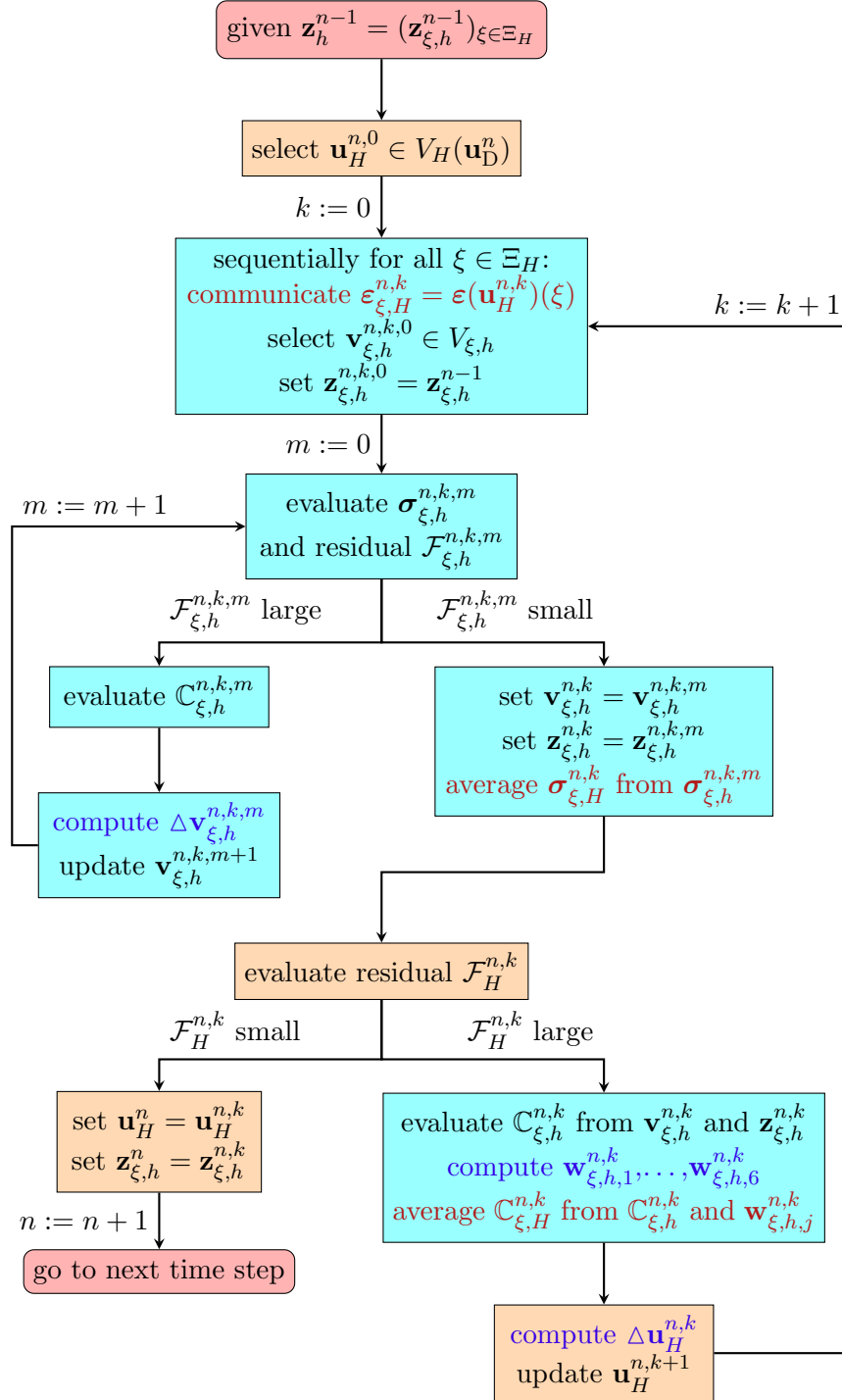


Figure 6.1: Flow chart of the parallel incremental inelastic two-scale algorithm. Turquoise boxes: Computations on the micro-scale. Other boxes: Computations on the macro-scale. Red boxes: Beginning and end of the loading increment. Blue lettering: Parallel multigrid computations. Red lettering: Collective communication and synchronization routines.

Chapter 7

Numerical experiments for inelastic material models

This chapter studies in various experiments the inelastic behavior of rate-independent two-scale material models. Furthermore, a reduced FE² method for optimizing the complex computations is introduced, as well as an investigation of the convergence properties for various scales of heterogeneities. All the simulations have been implemented in the parallel finite element software M++ [65] using a multigrid method with a highly scalable parallel coarse grid solver [35] with Gauss-Seidel smoother.

7.1 Monotonic tensile tests

Again we use the test configuration in Section 4.2 of a polymer PBT with firmly embedded glass fibers with one fourth of the geometry $\Omega_{\text{sym}} \subset \Omega$, see Figure 4.4, and symmetry boundary conditions describing a two sided loading

$$\begin{aligned} \mathbf{u}_D(t, \mathbf{x}) &= \begin{pmatrix} 0 \\ 0 \\ u_0 t \end{pmatrix} && \text{for } x_3 = 6.5, \\ \boldsymbol{\sigma}(\boldsymbol{\varepsilon}(\mathbf{u}), \mathbf{z})\mathbf{n} &= \mathbf{0} && \text{for } \mathbf{x} \in \Gamma_N. \end{aligned}$$

The scaling factor is set to be $u_0 = 0.01$ and $t > 0$. The material parameters for the damage model are taken from [59]. We set in all our simulations the damping and yielding point parameter in the damage model for the polymer to $H = 0.22702$ and $Y_0 = 0.08692$, and for isotropic plasticity we use a yield strength $\sigma_y = 25$ and an isotropic linear hardening law with parameters $H_0 = 1$ and $K_\infty - K_0 = 0$. In V_H and $V_{\xi,h}$ we use conforming hexahedral \mathbb{Q}_1 finite elements.

7.1.1 Simple two-scale damage model

In this experiment we examine the inelastic monotonic uniaxial tensile test for the damage model, using a short fiber-reinforced microstructure with 10% fiber volume fraction and a fiber orientation of 90° to the applied force. We use 1024 integration points for the approximation of the macro-solution \mathbf{u}_H^n , and in every RVE a discretization with $\dim V_{\xi,h} = 823\,875$ for the representation of the micro-solution $\mathbf{v}_{\xi,h}^n$ and $\dim Z_{\xi,h} = 2\,097\,152$ to represent the damage variable $d_{\xi,h}^n$ at every integration point in the RVE.

The stress-strain curve shows the non-linear response in the specimen on the macro-level, which is caused by growing damage effects in the RVEs on the micro-level, see Figure 7.2. With respect to the deformation of the 6 micro-fluctuations $\mathbf{w}_{\xi,h,k}^0$ in $V_{\xi,h} \subset H_{\text{per}}^1(\mathcal{Y}_\xi, \mathbb{R}^D)$ the stress cases $\boldsymbol{\sigma}_{\xi,h}(\mathbf{w}_{\xi,h,k}^0)$ corresponding to the 6 basis tensors $\boldsymbol{\eta}_k$ in $\text{Sym}(3)$ are shown in Figure 7.2. The effective algorithmic material tangent $\mathbb{C}_{\xi,H}^0$ has in every elastic integration point an anisotropic material response, see Figure 7.3. The evolution of the damage field $d_{\xi,h}^n$ of an intersected RVE \mathcal{Y}_ξ around an integration point $\xi = (0.115470, 0.302831, 1.183013)^T$ in the test

bar is shown in Figure 7.4. In the RVE we observe an overall damage of the matrix and severe damage between nearby fibers. Figure 7.5 shows on the left hand side the evolution of the averaged stress $\boldsymbol{\sigma}_{\xi,H}^n = \frac{1}{|\mathcal{Y}_\xi|} \int_{\mathcal{Y}_\xi} \boldsymbol{\sigma}_{\xi,h}^n \, d\mathbf{x}$ and on the right hand side the evolution averaged damage $d_{\xi,H}^n = \frac{1}{|\mathcal{Y}_\xi|} \int_{\mathcal{Y}_\xi} d_{\xi,h}^n \, d\mathbf{x}$. This shows the scale transition of the two-scale damage model by the loss of stress in strongly damaged areas. Finally the material response in every RVE gets inelastic.

The simulation for $t \in [0, 172]$ requires in 43 loading increments with 42 735 evaluations of the effective algorithmic tangent $\mathbb{C}_{\xi,H}^n$ and 216 894 Newton iterations for the computation of the micro-fluctuation $\mathbf{v}_{\xi,h}^n$. For the simulation we used an extrapolated implicit Euler scheme with equidistant time stepping size $\Delta t = 4$. The computation took 4 days, 22 hours and 41 minutes on the ForHlr2 B.3 cluster with 512 cores distributed across 32 nodes each using 16 cores.

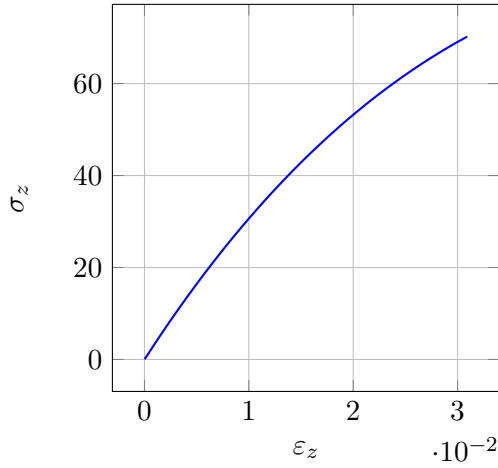


Figure 7.1: Stress-strain curve of a uniaxial monotonic tensile test for a short fiber-reinforced composite with 10% fiber volume fraction and 90° fiber orientation to tensile load.

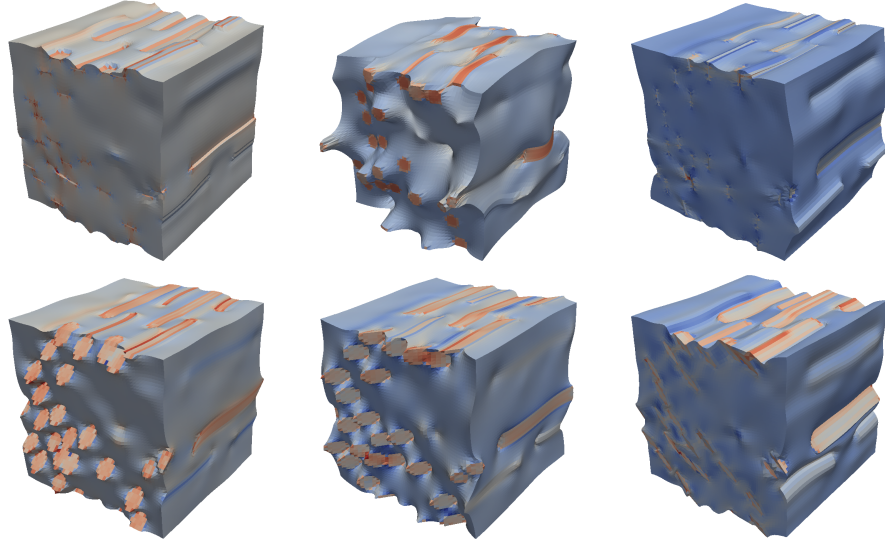


Figure 7.2: Stress states $\sigma_{\xi,h}(\mathbf{w}_{\xi,h,k}^0)$ with respect to the deformation of the 6 micro-fluctuations $\mathbf{w}_{\xi,h,k}^0$ in $V_{\xi,h} \subset H_{per}^1(\mathcal{Y}_{\xi}, \mathbb{R}^D)$ corresponding to the 6 basis tensors $\boldsymbol{\eta}_k$ in $\text{Sym}(3)$ (increasing values from blue to red).

$$\mathbb{C}_{\xi,H}^0 = \begin{pmatrix} 6254.19 & 3913.96 & 4003.21 & 0.61 & 1.08 & -7.87 \\ 3913.96 & 9264.65 & 3934.67 & 3.63 & -16.67 & 2.36 \\ 4003.21 & 3934.67 & 6313.78 & -0.54 & -0.44 & -1.68 \\ 0.61 & 3.63 & -0.54 & 2316.07 & -6.66 & 0.91 \\ 1.08 & -16.67 & -0.44 & -6.66 & 2388.84 & -0.89 \\ -7.87 & -2.36 & -1.68 & 0.91 & -0.89 & 2288.76 \end{pmatrix}$$

Figure 7.3: Preprocessed anisotropic elastic two-scale tensor $\mathbb{C}_{\xi,H}^0$ for an short fiber-reinforced microstructure with 10% volume fraction and 90° fiber orientation to the applied load.

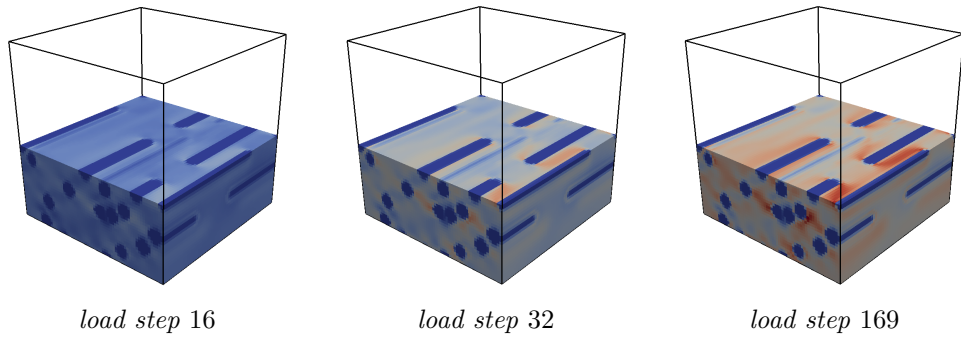


Figure 7.4: Evolution of the damage field $d_{\xi,h}^n$ of a uniaxial component test for a unidirectional short fiber-reinforced polymer with 10% fiber volume content and 90° fiber orientation to the exerted force of an intersected RVE \mathcal{Y}_{ξ} around an integration point $\xi = (0.115470, 0.302831, 1.183013)^T$ in the specimen at selected load steps (increasing values from blue to red).

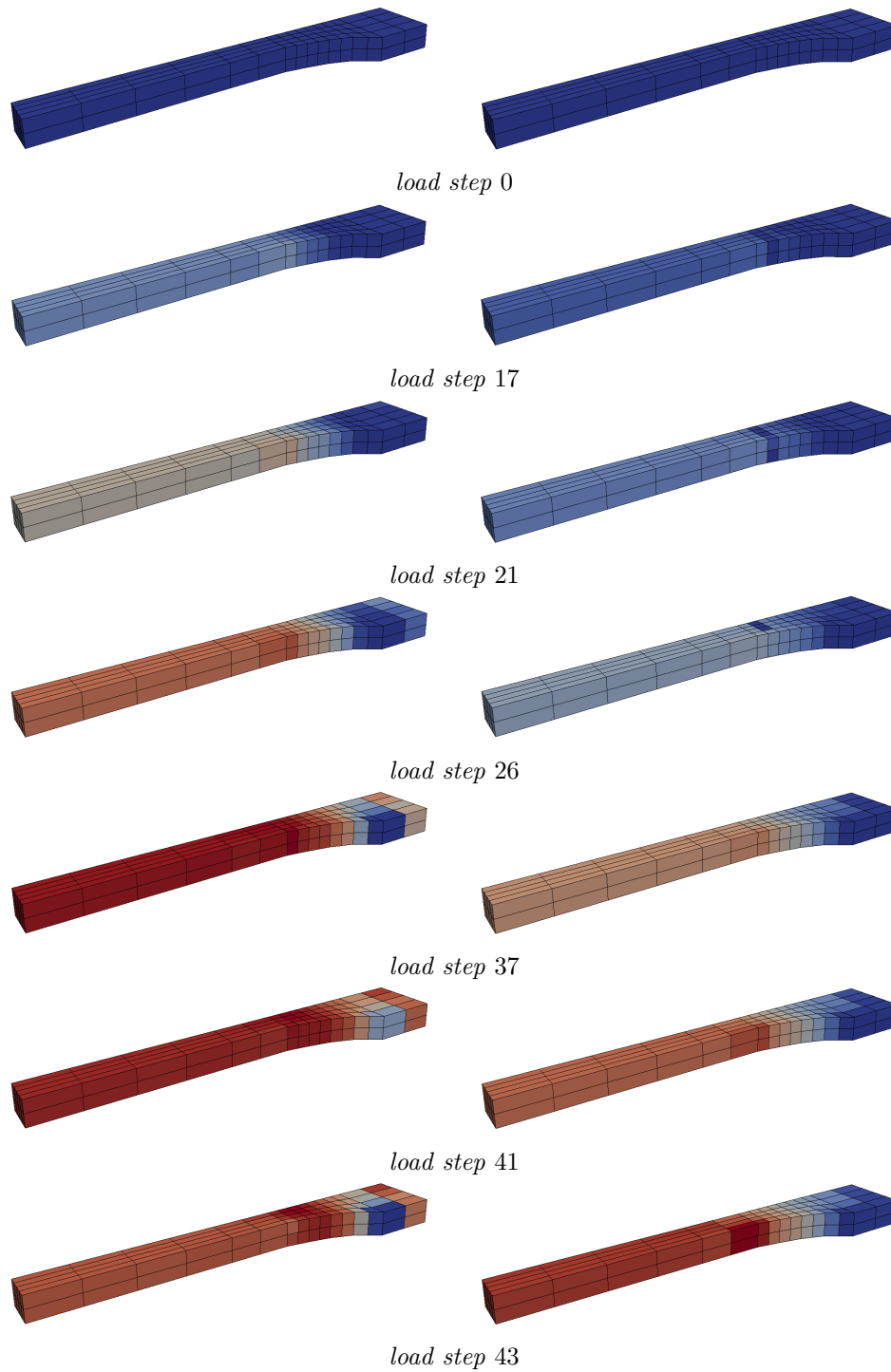


Figure 7.5: Comparison of the evolution between the stress state $\sigma_{\xi,H}^n$ (left) and the damage field $d_{\xi,H}^n$ (right) of the specimen at selected load steps of a uniaxial component test for a short fiber-reinforced material with 10% fiber volume fraction and 0° fiber alignment with respect to the traction in every RVE (increasing values from blue to red).

7.1.2 The two-scale elasto-plasticity model

In this experiment we examine the inelastic uniaxial tensile test for the elasto-plasticity model with a linear isotropic hardening law. We use a short fiber-reinforced microstructure with 10% fiber volume content and a fiber orientation of 45° to the acting force. For the representation of the macro-solution \mathbf{u}_H^n we use 128 integration points and in every RVE a discretization with $\dim V_{\xi,h} = 823\,875$ for the representation of the micro-solution $\mathbf{v}_{\xi,h}^n$ and $\dim Z_{\xi,h} = 2\,097\,152$ to represent the variable of the plastic strain $\boldsymbol{\varepsilon}_{p,\xi,h}^n$ and the isotropic hardening parameter $r_{\xi,h}^n$ at every integration point in the RVE.

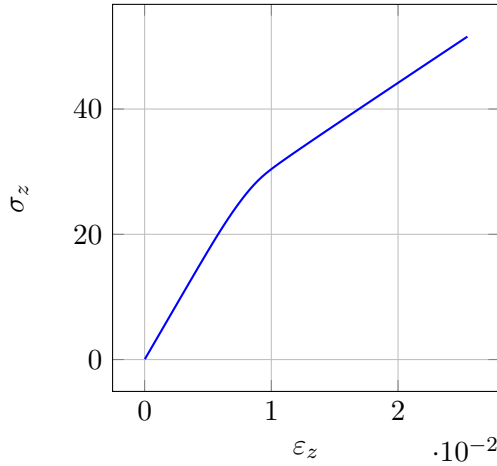


Figure 7.6: Stress-strain curve of a uniaxial monotonic tensile test for a short fiber-reinforced composite with 10% fiber volume fraction and 45° fiber orientation to tensile load.

We noticeably observe in the nonlinear stress-strain curve the linear hardening law of the material model after it starts yielding, see Figure 7.6. With respect to the deformation of the 6 elastic micro-fluctuations $\mathbf{w}_{\xi,h,k}^0$ in $V_{\xi,h} \subset H_{\text{per}}^1(\mathcal{Y}_\xi, \mathbb{R}^D)$ the stress states $\boldsymbol{\sigma}_{\xi,h}(\mathbf{w}_{\xi,h,k}^0)$ corresponding to the 6 basis tensors $\boldsymbol{\eta}_k$ in $\text{Sym}(3)$ are shown in Figure 7.7. The effective algorithmic material tangent $\mathbb{C}_{\xi,H}^0$ evaluated by the 6 elastic micro-fluctuations $\mathbf{w}_{\xi,h,k}^0$ has an anisotropic material response in every elastic integration point of the specimen, see Figure 7.8. The evolution of the plastic strain field $\boldsymbol{\varepsilon}_{p,\xi,h}^n$ of an intersected RVE \mathcal{Y}_ξ around an integration point $\xi = (0.115470, 0.302831, 1.183013)^T$ in the specimen at selected load steps is shown in Figure 7.9. We observe that inelastic plasticity effects only occur around and between nearby fibers. Figure 7.10 shows on the left hand side the evolution of the continuously increasing averaged stress variable $\boldsymbol{\sigma}_{\xi,H}^n = \frac{1}{|\mathcal{Y}_\xi|} \int_{\mathcal{Y}_\xi} \boldsymbol{\sigma}_{\xi,h}^n \, d\mathbf{x}$ and on the right hand side the evolution of the continuously increasing averaged plastic strain $\boldsymbol{\varepsilon}_{p,\xi,H}^n = \frac{1}{|\mathcal{Y}_\xi|} \int_{\mathcal{Y}_\xi} \boldsymbol{\varepsilon}_{p,\xi,h}^n \, d\mathbf{x}$. Finally the material response in every RVE is inelastic.

The simulation for $t \in [0, 135]$ requires in 90 loading increments 8 291 evaluations for the effective algorithmic material response $\mathbb{C}_{\xi,H}^n$ and 54 085 Newton iterations for the computation of the micro-fluctuation $\mathbf{v}_{\xi,h}^n$. For the simulation we used an extrapolated implicit Euler scheme with equidistant time stepping size $\Delta t = 1.5$. The computation took 25 hours, 48 minutes and 53 seconds on the ForHlr2 B.3 cluster with 512 cores distributed across 32 nodes each using 16 cores.

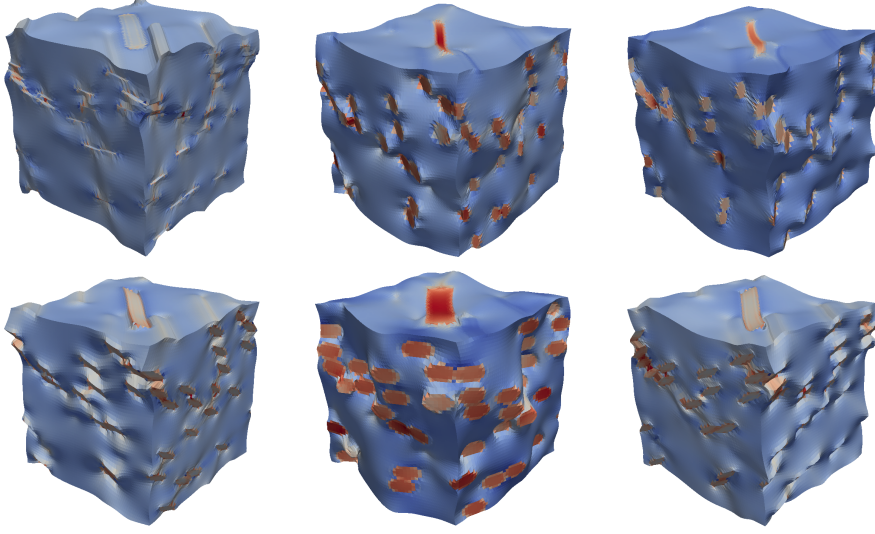


Figure 7.7: Stress states $\sigma_{\xi,h}(\mathbf{w}_{\xi,h,k}^0)$ with respect to the deformation of the 6 micro-fluctuations $\mathbf{w}_{\xi,h,k}^0$ in $V_{\xi,h} \subset H_{per}^1(\mathcal{Y}_{\xi}, \mathbb{R}^D)$ corresponding to the 6 basis tensors $\boldsymbol{\eta}_k$ in $\text{Sym}(3)$ (increasing values from blue to red).

$$\mathbb{C}_{\xi,H}^0 = \begin{pmatrix} 6348.28 & 3964.89 & 3987.37 & 0.57 & -23.82 & -0.38 \\ 3964.89 & 7592.02 & 4335.08 & 13.64 & 998.29 & 3.02 \\ 3987.37 & 4335.08 & 6464.97 & -1.59 & 360.00 & -14.38 \\ 0.57 & 13.64 & -1.59 & 2392.32 & -5.08 & 52.17 \\ -23.82 & 998.29 & 360.00 & -5.08 & 3146.34 & 4.65 \\ -0.38 & 3.02 & -14.38 & 52.17 & 4.65 & 2323.53 \end{pmatrix}$$

Figure 7.8: Preprocessed anisotropic elastic two-scale tensor $\mathbb{C}_{\xi,H}^0$ for an short fiber-reinforced microstructure with 10% volume fraction and 45° fiber orientation to the acting force.

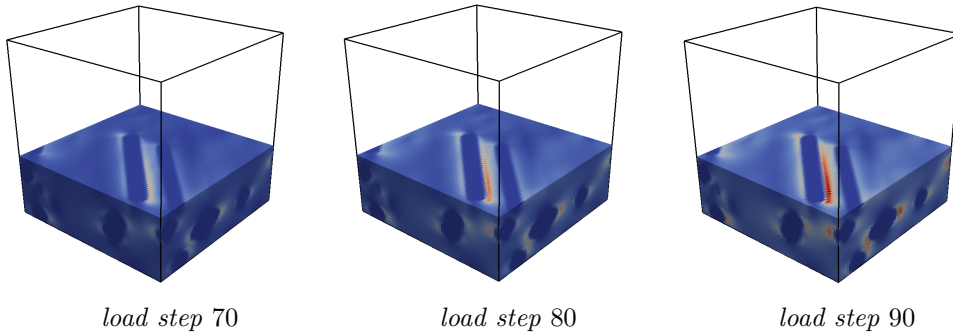


Figure 7.9: Evolution of the plastic strain field $\boldsymbol{\varepsilon}_{p,\xi,h}^n$ of a uniaxial component test for a unidirectional short fiber-reinforced material with 10% fiber volume share and 45° fiber alignment to the acting force of an intersected RVE \mathcal{Y}_{ξ} around an integration point $\boldsymbol{\xi} = (0.115470, 0.302831, 1.183013)^T$ in the specimen at selected load steps (increasing values from blue to red).

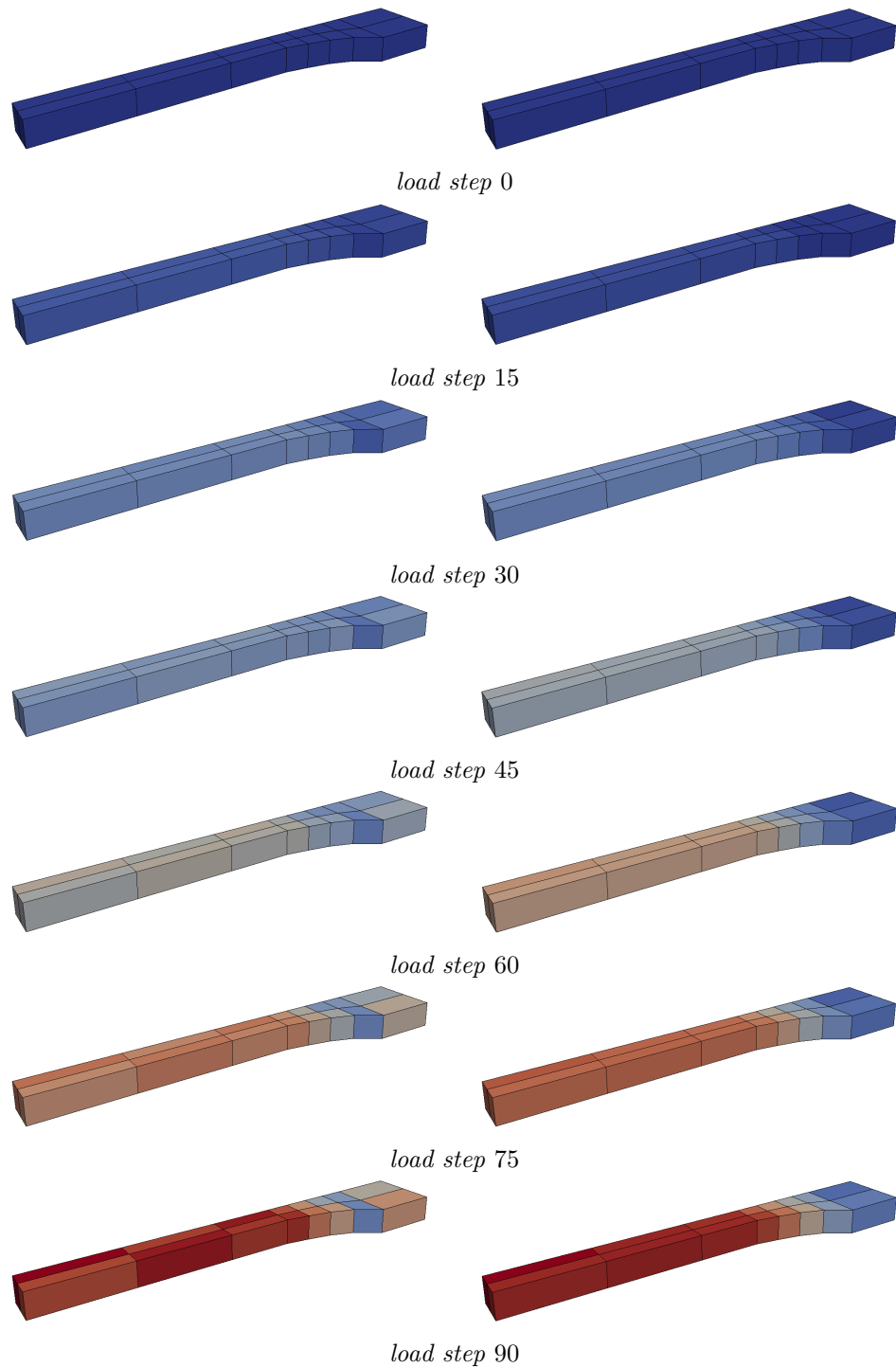


Figure 7.10: Comparison of the evolution between the stress state $\sigma_{\xi,H}^n$ (left) and the plastic strain field $\epsilon_{p,\xi,H}^n$ (right) of the specimen at selected load steps of a uniaxial component test for a short fiber-reinforced material with 10% fiber volume fraction and 45° fiber alignment with respect to the traction in every RVE (increasing values from blue to red).

7.1.3 Two-scale elasto-plasticity with damage

In this experiment we investigate the inelastic monotonic uniaxial tensile test for the elasto-plasticity model with linear hardening and damage, using a microstructure with 10% fiber volume fraction and a fiber orientation of 90° to the acting traction. For the macro-solution \mathbf{u}_H^n we use a discretization with 1024 integration points and in every RVE a discretization with $\dim V_{\xi,h} = 823\,875$ for the representation of the micro-solution $\mathbf{v}_{\xi,h}^n$ and $\dim Z_{\xi,h} = 2\,097\,152$ to represent the damage variable $d_{\xi,h}^n$, the plastic strain $\boldsymbol{\varepsilon}_{p,\xi,h}^n$ and the isotropic hardening parameter $r_{\xi,h}^n$ at every integration point in the RVE.

The nonlinear stress-strain curve shows the inelastic effects of damage and plasticity with linear hardening, see Figure 7.11. Because of the same test scenario and numerical setting like in the investigation of the damage model, the once preprocessed linear algorithmic material tangent $\mathbb{C}_{\xi,H}^0$ is the same as in Figure 7.3 and has an anisotropic material response in every elastic integration point in the specimen. The evolution of the damage $d_{\xi,h}^n$ and the plastic strain $\boldsymbol{\varepsilon}_{p,\xi,h}^n$ of an RVE \mathcal{Y}_ξ around an integration point $\xi = (0.115470, 0.302831, 1.183013)^T$ in the specimen is shown in Figure 7.12 and 7.13. The evolution of the averaged damage field $d_{\xi,H}^n = \frac{1}{|\mathcal{Y}_\xi|} \int_{\mathcal{Y}_\xi} d_{\xi,h}^n \, d\mathbf{x}$, the plastic strain field $\boldsymbol{\varepsilon}_{p,\xi,H}^n = \frac{1}{|\mathcal{Y}_\xi|} \int_{\mathcal{Y}_\xi} \boldsymbol{\varepsilon}_{p,\xi,h}^n \, d\mathbf{x}$ and the stress variable $\boldsymbol{\sigma}_{\xi,H}^n = \frac{1}{|\mathcal{Y}_\xi|} \int_{\mathcal{Y}_\xi} \boldsymbol{\sigma}_{\xi,h}^n \, d\mathbf{x}$ is shown in Figure 7.14 and 7.15. Here we observe that the stress increases first. Then, the stress decreases in strongly damaged areas until plastification starts yielding and thereby the stress increases again. Finally the material response in every RVE is inelastic.

The simulation for $t \in [0, 67.5]$ requires in 45 loading increments 34 989 evaluations of the effective algorithmic material response $\mathbb{C}_{\xi,H}^n$ and 165 564 Newton iterations for the computation of the micro-fluctuation $\mathbf{v}_{\xi,h}^n$. For the simulation we used an extrapolated implicit Euler scheme with equidistant time stepping size $\Delta t = 1.5$. The computation took 3 days, 23 hours and 53 minutes on the ForHlr2 B.3 cluster with 512 cores distributed across 32 nodes each using 16 cores.

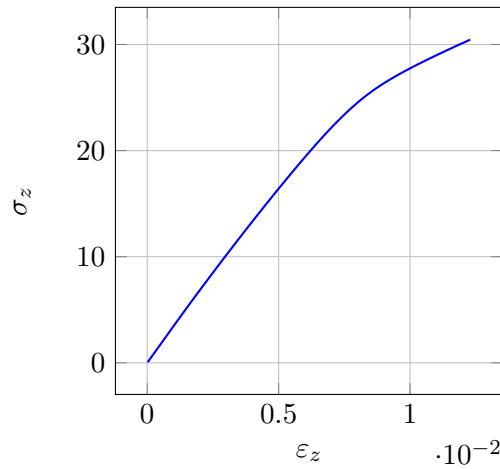


Figure 7.11: Stress-strain curve of a uniaxial monotonic tensile test for a short fiber-reinforced composite with 10% fiber volume fraction and 90° fiber orientation to tensile load.

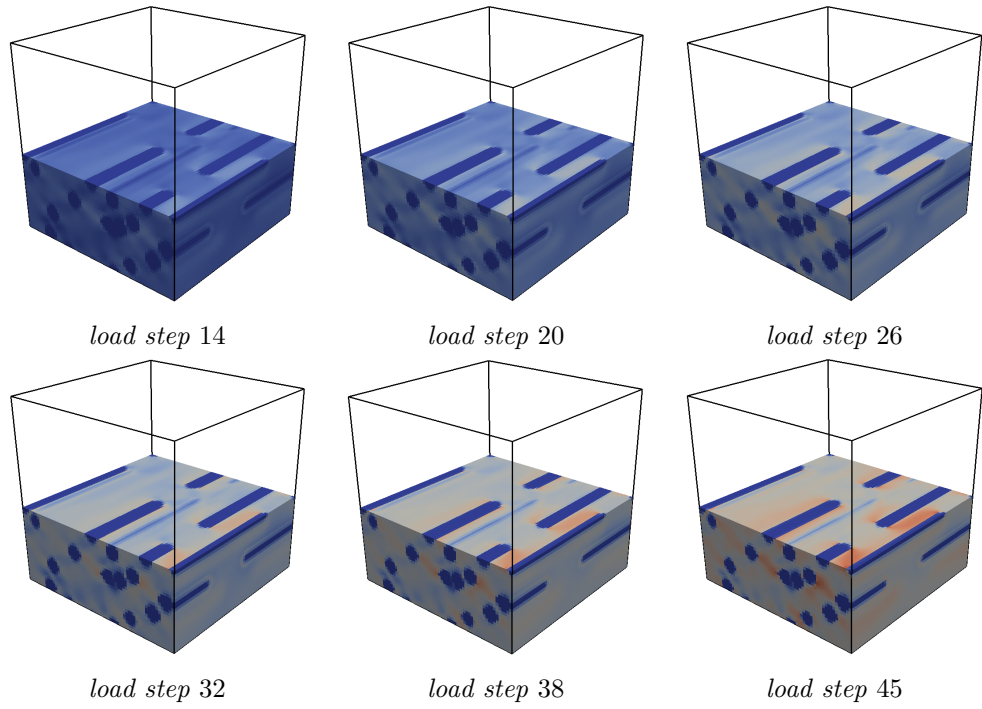


Figure 7.12: Evolution of the damage field $d_{\xi,h}^n$ of a uniaxial monotonic component test for a unidirectional short fiber-reinforced material with 10% fiber volume content and 90° fiber orientation to the exerted force of an intersected RVE \mathcal{V}_ξ around an integration point $\xi = (0.115470, 0.302831, 1.183013)^T$ in the specimen at selected load steps (increasing values from blue to red).

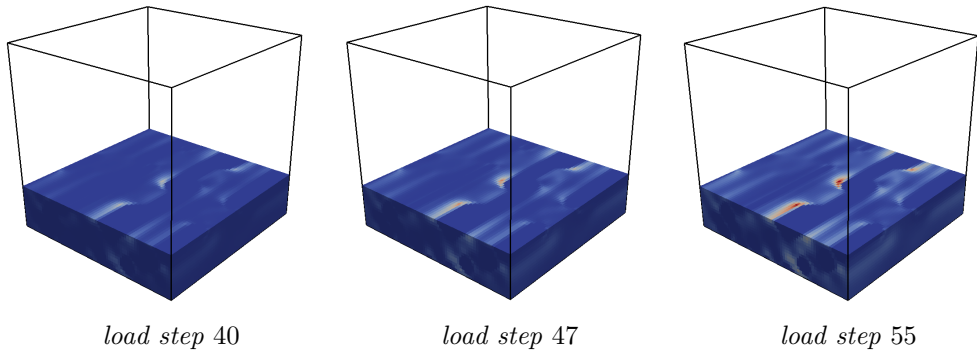


Figure 7.13: Evolution of the plastic strain field $\epsilon_{p,\xi,h}^n$ of a uniaxial monotonic component test for a unidirectional short fiber-reinforced material with 10% fiber volume share and 90° fiber orientation to the acting force of an intersected RVE \mathcal{V}_ξ around an integration point $\xi = (0.115470, 0.302831, 1.183013)^T$ in the specimen at selected load steps (increasing values from blue to red).

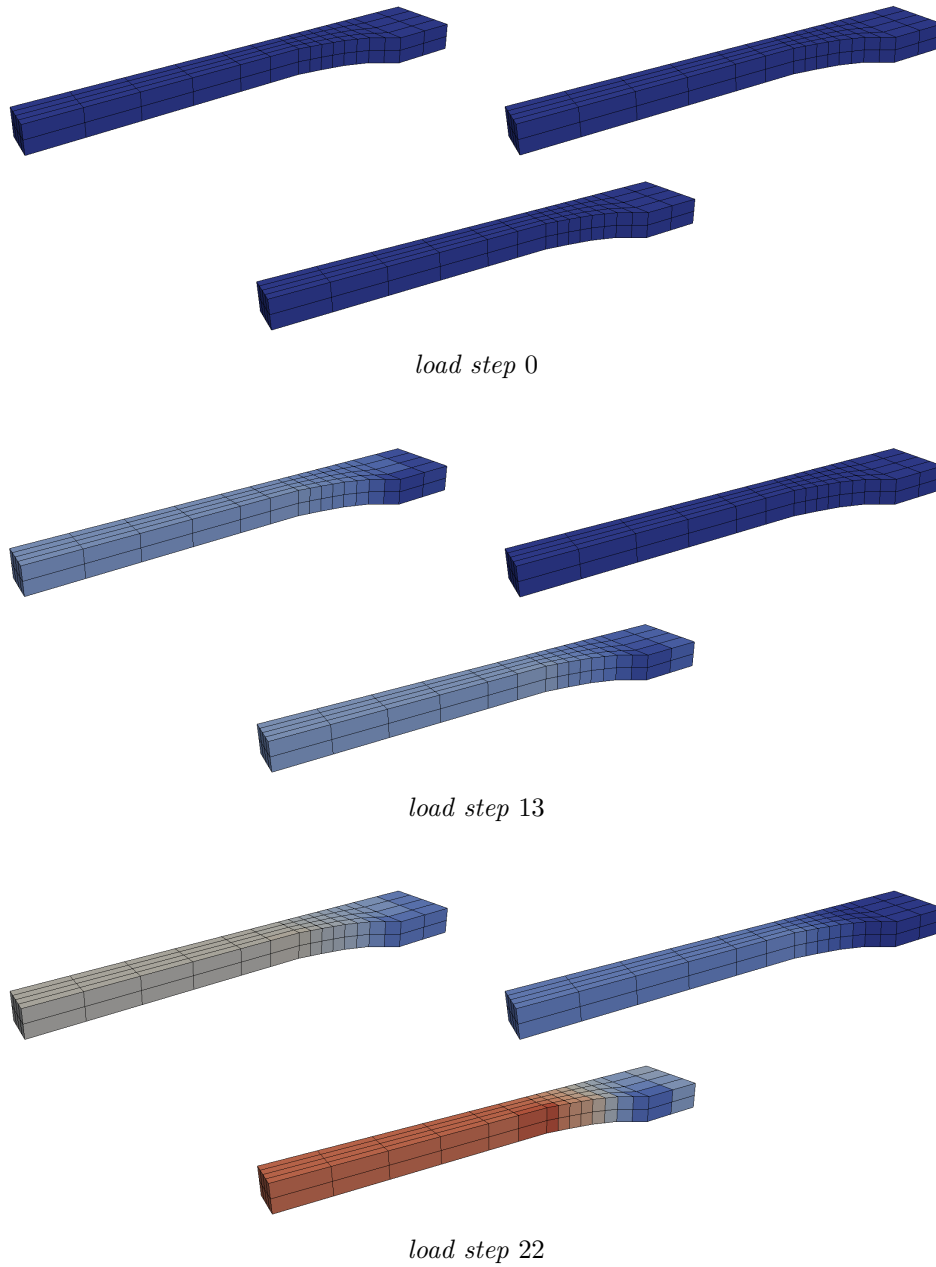


Figure 7.14: Part 1: Comparison of the evolution between the stress state $\sigma_{\xi,H}^n$ (bottom), the damage field $d_{\xi,H}^n$ (top left) and the plastic strain field $\varepsilon_{p,\xi,H}^n$ (top right) of the specimen at selected load steps of a uniaxial monotonic component test for a unidirectional short fiber-reinforced material with 10% fiber volume fraction and 90° fiber orientation to the traction in every RVE (increasing values from blue to red).

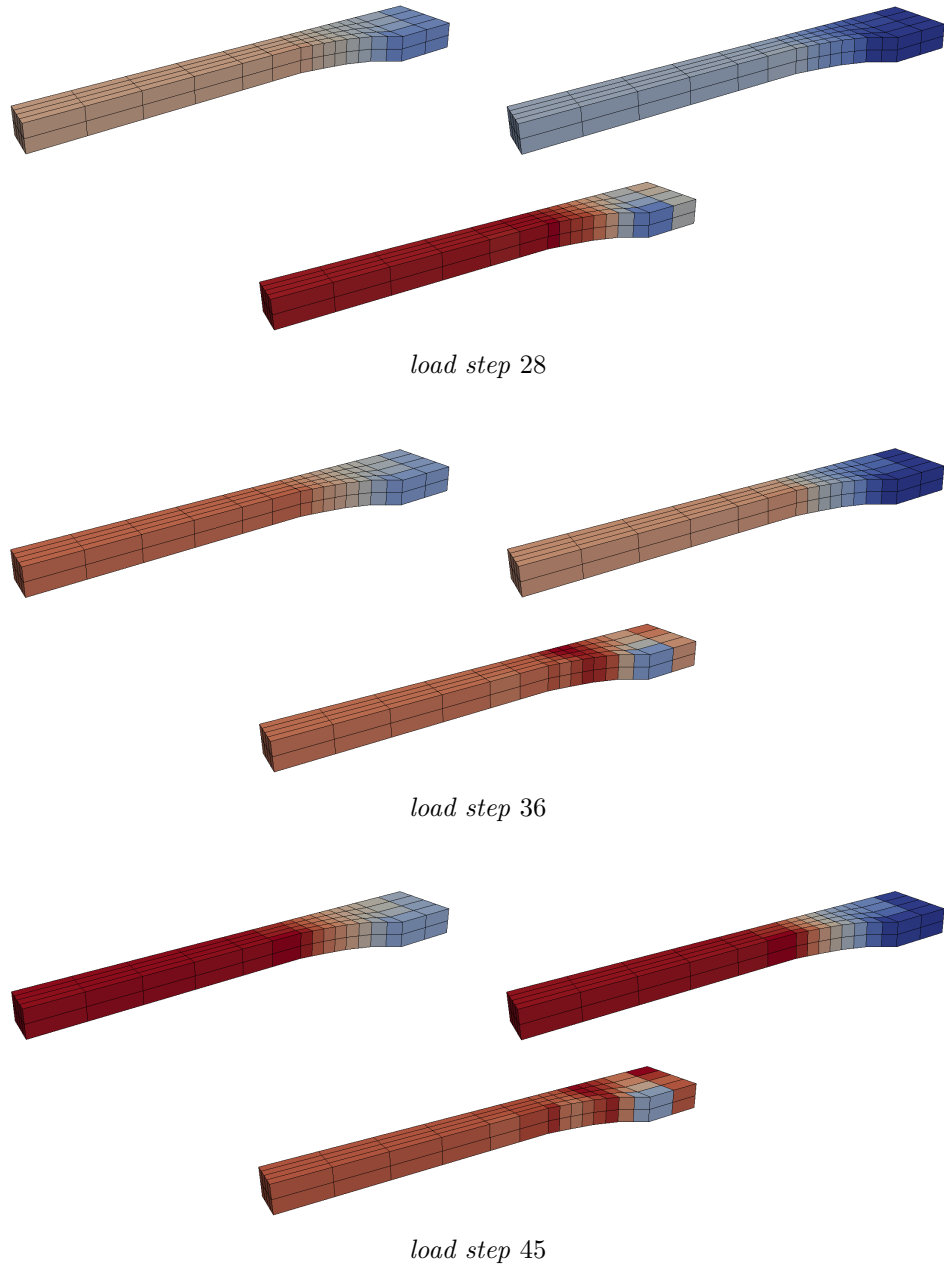


Figure 7.15: Part 2: Comparison of the evolution between the stress state $\sigma_{\xi,H}^n$ (bottom), the damage field $d_{\xi,H}^n$ (top left) and the plastic strain field $\epsilon_{p,\xi,H}^n$ (top right) of the specimen at selected load steps of a uniaxial monotonic component test for a unidirectional short fiber-reinforced material with 10% fiber volume fraction and 90° fiber orientation to the traction in every RVE (increasing values from blue to red).

7.1.4 Various fiber orientations and filler contents

Now, we consider how the material behaves when it becomes loaded beyond the elastic yield limit during a uniaxial monotonic component test for the incremental two-scale damage model. In every RVE we use a microstructure with 10%, 20% and 30% fiber volume filler content and 0° , 45° , 60° and 90° fiber orientation to the applied load. For the representation of the macro-solution we use 128 integration points and in every RVE a discretization with $\dim V_{\xi,h} = 107\,811$ for the representation of the micro-solution $\mathbf{v}_{\xi,h}^n$ and $\dim Z_{\xi,h} = 262\,144$ to represent the damage variable $d_{\xi,h}^n$ at every integration point in the RVE. All the simulations have been performed on the IC2 B.2 cluster with 128 cores distributed across 8 nodes each using 16 cores.

Stress-strain relation: The relationship of tensile force to increasing gauge length, as defined by the stress-strain curves in Figure 7.16, highlights for each fixed fiber orientation with respect to different filler contents, that the most stiffness is achieved for parallel fiber and tensile load orientation. The greater the fiber orientation deviates from the direction of the applied load, the less rigid behaves the two component composite.

Young's modulus: The change in Young's modulus for each ideal elastic medium is a constant. For each inelastic medium it becomes a function in time and load, see Figure 7.17. We observe that Young's modulus is constant for very small deformations. This shows that small loads already lead to damage effects. After reaching the elastic yield limit we observe a linear decrease in Young's modulus for each fiber orientation. For a parallel fiber load orientation the decrease in Young's modulus behaves similar for all fiber filler contents. For all other fiber orientations the linear loss in stiffness becomes stronger for increasing fiber filler contents.

Anisotropy: For the investigation of the isotropy behavior we consider the inelastic evolution of Poisson's ratio and the transversal elongations in the plane orthogonally aligned to the tensile load, see Figure 7.18 and 7.19. For a parallel aligned tensile and fiber orientation the elongations ε_x and ε_y are almost equal respective to the elongation ε_z in tensile direction. This corresponds to the rotational axis along the fiber orientation and therefore the material is perfectly isotropic in the plane transversely to the acting force. For different fiber orientations to tensile load, the material behaves strongly anisotropic over the entire loading time. While the function of Poisson's ratio for an ideal elastic composite is a constant, this characteristic quantity is a function in time and load type for materials with memory. The initial values are within the range of 0.25 and 0.5 and finally between 0.1 and 0.5. Poisson's ratio behaves almost constant with very small deviations over the entire loading time. By means of Poisson's ratio the above anisotropy considerations can be verified.

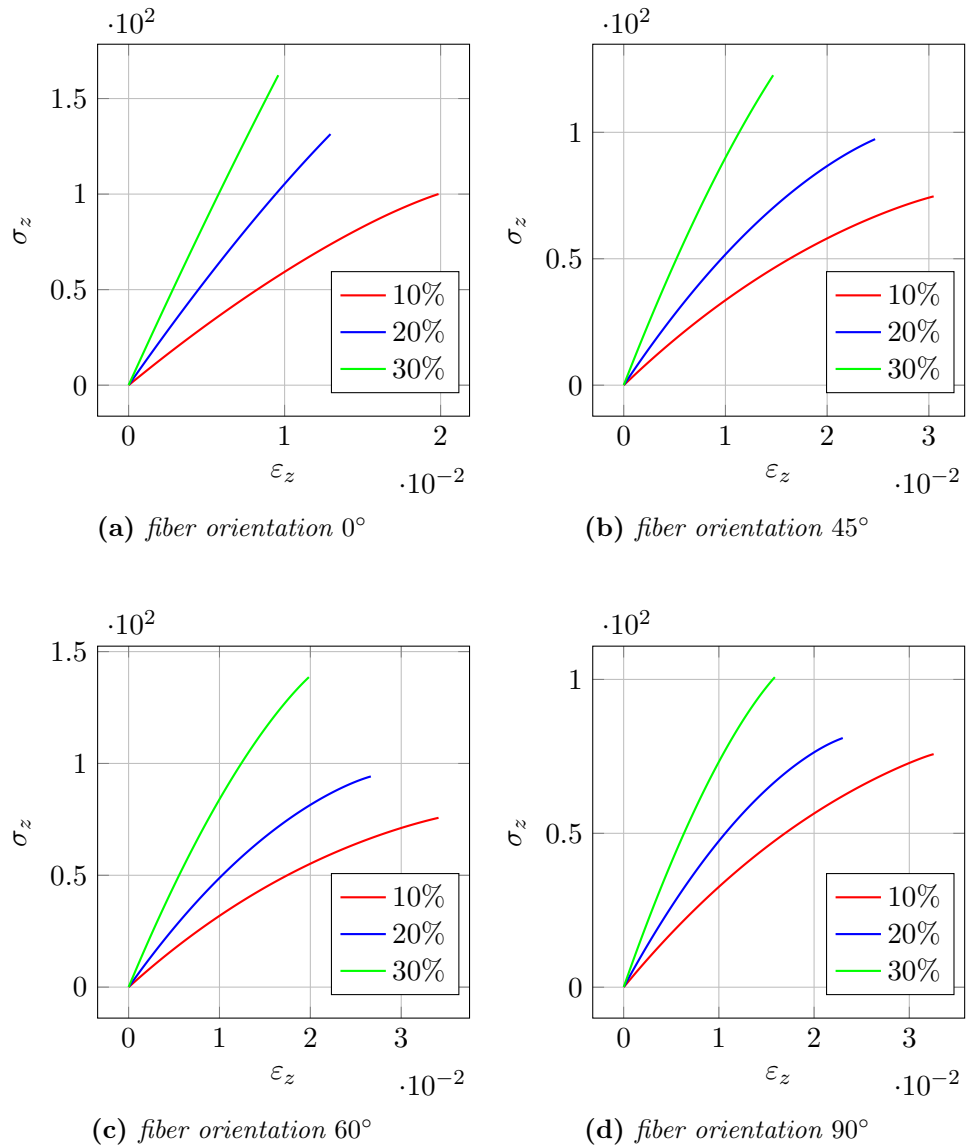


Figure 7.16: Stress-strain curves of a uniaxial monotonic tensile test respective different fiber volume fractions with 10%, 20% and 30% compared to various fixed fiber orientations (a) 0° , (b) 45° , (c) 60° and (d) 90° for a unidirectional short fiber-reinforced material.

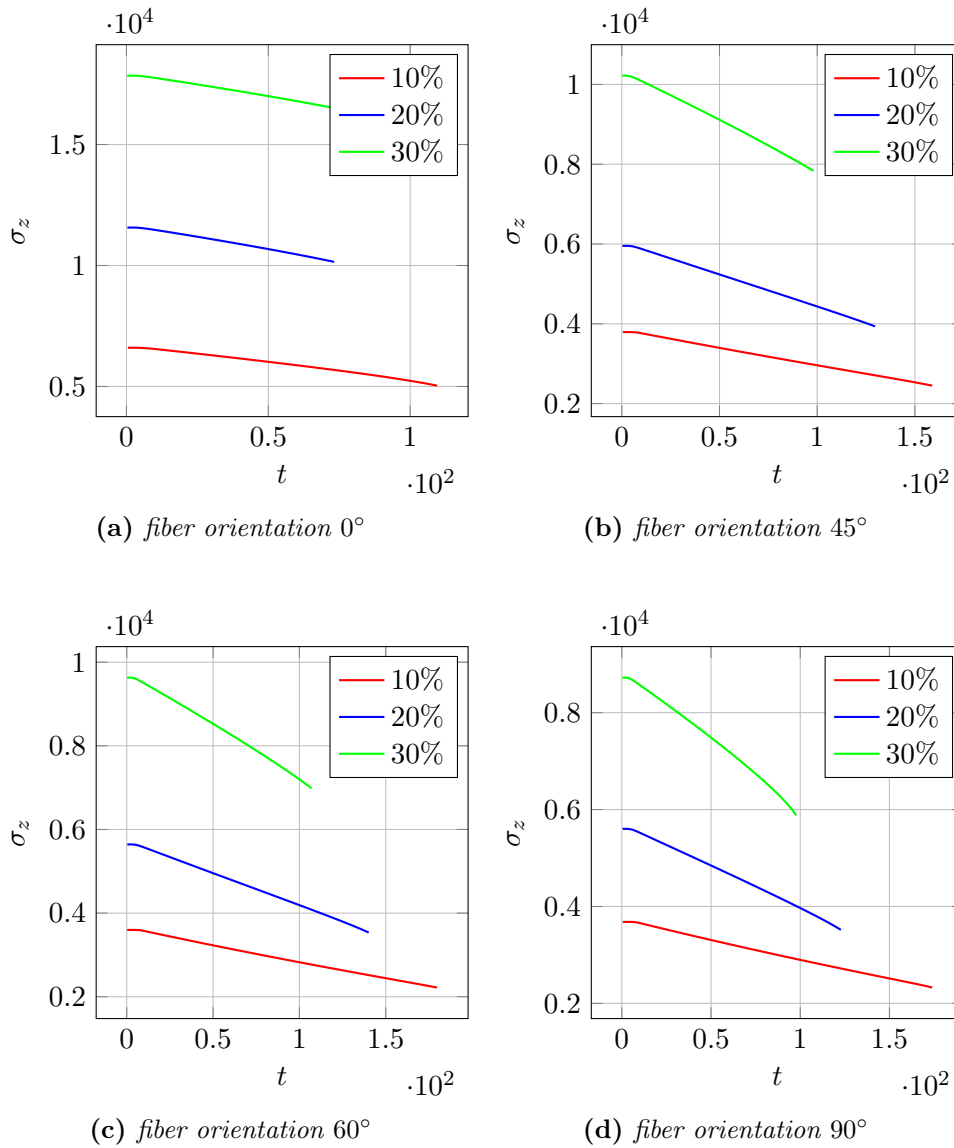


Figure 7.17: Comparison of the E-module E_z in tensile direction over the entire loading time of a uniaxial monotonic tensile test respective different fiber volume fractions with 10%, 20% and 30% with respect to various fixed fiber orientations (a) 0° , (b) 45° , (c) 60° and (d) 90° for a unidirectional short fiber-reinforced material.

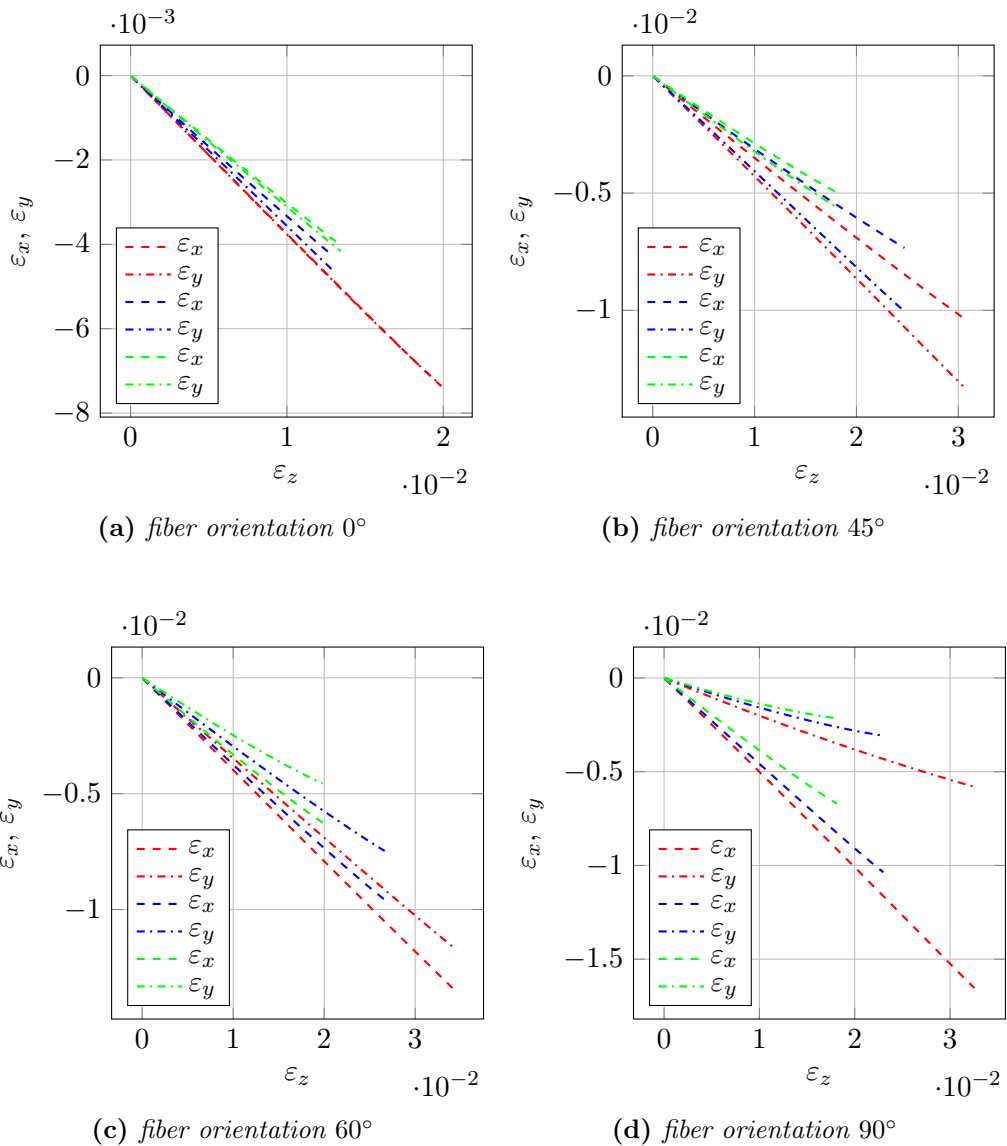


Figure 7.18: Transversal anisotropy investigation over the entire loading time by comparison of the transversal elongations ε_x and ε_y respective to the tensile elongation ε_z of a uniaxial monotonic tensile test respective different fiber volume fractions 10% (red), 20% (blue) and 30% (green) with respect to various fixed fiber orientations (a) 0° , (b) 45° , (c) 60° and (d) 90° for a unidirectional short fiber-reinforced material.

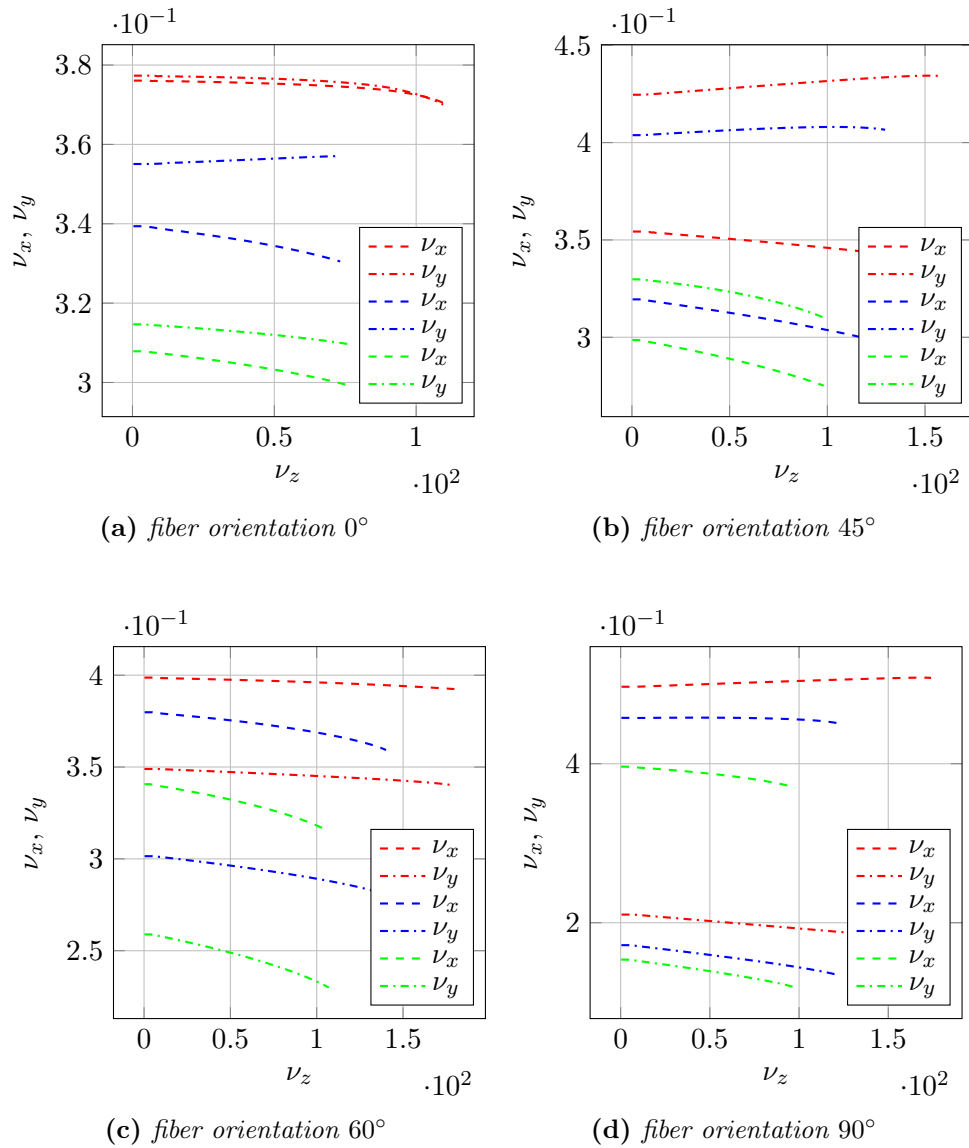


Figure 7.19: Comparison of Poisson's ratio ν_{zx} and ν_{zy} over the entire loading time of a uniaxial monotonic tensile test respective different fiber volume fractions 10% (red), 20% (blue) and 30% (green) with respect to various fixed fiber orientations (a) 0° , (b) 45° , (c) 60° and (d) 90° for a unidirectional short fiber-reinforced material.

Conclusions: The stress-strain curves and the anisotropy investigation for various fiber volume filler contents and fiber orientations of the numerical experiments in Figure 7.16 and 7.18 qualitative transfers to the measurements of a short fiber-reinforced polymer with PBT as carrier matrix, cf. [51, Chap. 2.2, Fig. 10].

7.2 Cyclic component tests

We extend the monotonic uniaxial tensile test to uniaxial cyclic component testing. For the investigation of different inelastic effects we start on the boundary $\Gamma_D \cup \Gamma_N \cup \Gamma_{\text{sym}} = \partial\Omega$ described by a Dirichlet boundary $\Gamma_D = \{\mathbf{x} \in \partial\Omega : x_3 = 6.5\}$, a Neumann boundary $\Gamma_N = \partial\Omega \setminus \{\Gamma_D \cup \Gamma_{\text{sym}}\}$ and a symmetry boundary $\Gamma_{\text{sym}} = \{\mathbf{x} \in \partial\Omega : x_3 = 0 \text{ or } x_2 = 0\}$ with a uniaxial displacement driven load at $x_3 = 6.5$ with

$$\mathbf{u}_D(t, \mathbf{x}) = \begin{cases} (t - T_{k-1})\mathbf{u}_0 & T_{k-1} < t < T_k \text{ loading,} \\ (T_k - t)\mathbf{u}_0 & T_k < t < T_{k+1} \text{ unloading,} \end{cases} \quad \mathbf{u}_0 = \begin{pmatrix} 0 \\ 0 \\ u_0 \end{pmatrix}$$

for the transition points $T_0 = 0 < T_1 < T_2 < \dots$ from loading to unloading and from unloading to loading and we use Neumann boundary conditions $\boldsymbol{\sigma}(\boldsymbol{\varepsilon}(\mathbf{u}), \mathbf{z})\mathbf{n} = \mathbf{0}$ at $\mathbf{x} \in \Gamma_N$. The scaling factor is set to $u_0 = 0.01$. For the comparison of different material models we compute several load cycles. The transition points T_1, T_3, T_5, \dots are chosen such that the maximal stress is increased in every load cycle, and for complete unloading we set $T_{2k} = 2T_{2k-1} - T_{2k-2}$. In V_H and $V_{\xi, h}$ we use a conforming hexahedral space \mathbb{Q}_1 .

7.2.1 Comparison of inelastic two-scale models

In this section we investigate the inelastic material properties for a uniaxial cyclic test scenario for various inelastic two-scale models by the stress-strain curves and the load step diagram, see Figure 7.20. The material parameters for the damage model are taken from [59]. In all cases we use a specimen with 128 integration points and in every RVE a microstructure with 10% fiber volume fraction and a fiber orientation of 90° to the acting force. We set in all our simulations the damping and yielding point parameter in the damage model for the polymer to $H = 0.22702$ and $Y_0 = 0.08692$. For the elastoplasticity model we select a yield strength $\sigma_y = 45$ and an isotropic linear hardening law with parameters $H_0 = 1$ and $K_\infty - K_0 = 0$. In the combining model of damage and plasticity we select a yield strength $\sigma_y = 33$.

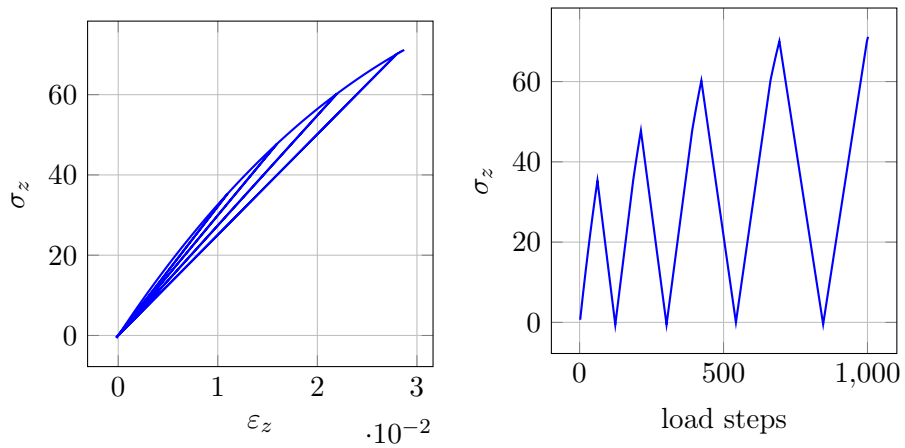
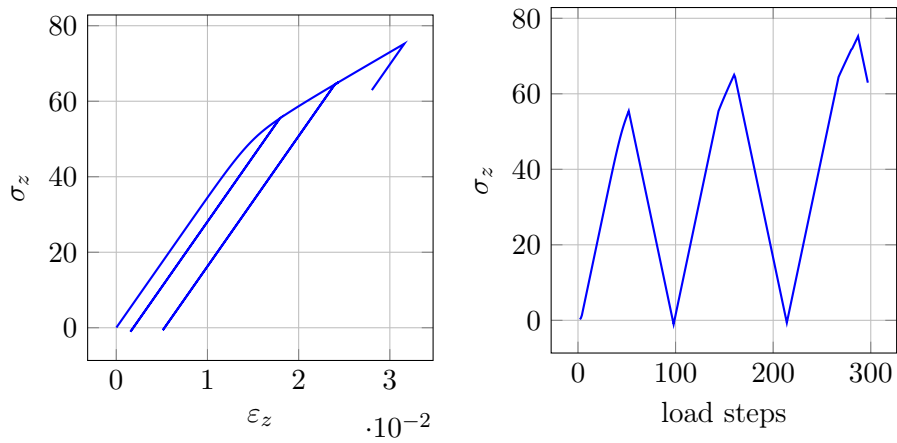
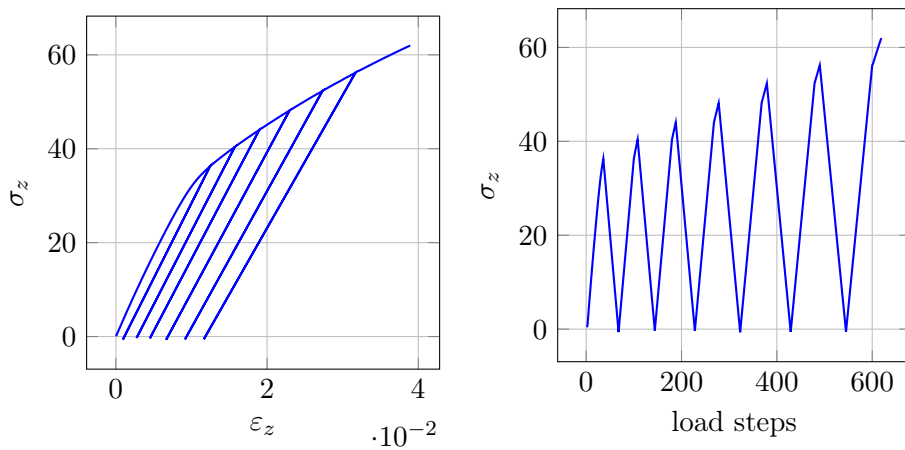
(a) *two-scale damage model*(b) *two-scale elasto-plasticity model with linear hardening*(c) *two-scale elasto-plasticity model with linear hardening and damage*

Figure 7.20: Stress-strain curve (left) and stress-load step diagram (right) of a uniaxial cyclic tensile test with 10% fiber volume fraction and 90° fiber orientation.

Comparison: In the following we compare the inelastic behavior of various rate-independent material models, see Figure 7.20. Each material model behaves elastically until the yield strength is reached. Within this region the composite recovers completely when the load is removed. Beyond this point, the material starts to yield and hardens. During this, the stress decreases continuously due to growing inelastic effects like damage and plasticity. On the other hand, the yield surface increases and the transition from loading to unloading determines the new elastic yield limit. We observe noticeably a linear isotropic hardening law for the elasto-plasticity model and a nonlinear material law for the inelastic evolution of the damage model. However, micromechanical defects cause permanent measurable global changes. After removing the acting force completely, damage effects cause a permanent loss of the elastic stiffness and plasticity effects leads to a permanent strain. When the material is reloaded again it behaves elastically until it exceeds the new elastic yield limit. The coupled model combines the individual effects of isotropic damage and elasto-plasticity with linear hardening.

Conclusions: Comparing with experimental data [51, Chap. 2.2, Fig. 6] we observe that the elasto-plasticity model with damage is sufficient to describe the behavior of a short fiber-reinforced polymer adequately. This shows that the coarse resolution on the macro-scale and the fine resolution on the micro-scale is sufficient enough.

Computation of the two-scale damage model: For the inelastic evolution we use for the simulation in every RVE a discretization with $\dim V_{\xi,h} = 107\,811$ for the representation of the micro-solution $\mathbf{v}_{\xi,h}^n$ and $\dim Z_{\xi,h} = 262\,144$ to represent the damage variable $d_{\xi,h}^n$ at every integration point in the RVE. The inelastic evolution of the simulation requires in 1 003 loading increments 457 012 Newton iteration steps for the computation of the micro-fluctuation $\mathbf{v}_{\xi,h}^n$ and 73 155 evaluations of the effective algorithmic material response $\mathbb{C}_{\xi,H}^n$. Finally, the material response in every RVE is inelastic. We used an extrapolated implicit Euler scheme with equidistant time stepping size $\Delta t = 1$. The simulation was performed on the IC2 B.2 cluster with 256 cores distributed on 16 nodes each equipped with 16 cores and ended automatically after exactly 3 days.

Computation of the two-scale elasto-plasticity model: We use in every RVE $\dim V_{\xi,h} = 892\,857$ for the representation of the micro-solution $\mathbf{v}_{\xi,h}^n$, and $\dim Z_{\xi,h} = 2\,097\,152$ to represent the plastic strain $\boldsymbol{\varepsilon}_{p,\xi,h}^n$ and the isotropic hardening parameter $r_{\xi,h}^n$ at every integration point in the RVE. The computation of the simulation of the elasto-plasticity model with linear hardening requires in 298 loading increments 218 098 Newton iteration steps for the computation of the micro-fluctuation $\mathbf{v}_{\xi,h}^n$ and 94 420 evaluations of the material response $\mathbb{C}_{\xi,H}^n$. Finally, the material response in 126 of 128 RVEs behaves inelastic. For the evaluation of the incremental two-scale equation an

extrapolated implicit Euler scheme with equidistant loading increment $\Delta t = 2$ was used. The simulation of the uniaxial cyclic tensile test was performed for exactly 3 days on the IC2 B.2 cluster using 512 cores distributed across 32 nodes each using 16 cores.

Computation of the two-scale elasto-plasticity model with damage: In every RVE we use a discretization with $\dim V_{\xi,h} = 107\,811$ for the representation of the micro-solution $\mathbf{v}_{\xi,h}^n$ and $\dim Z_{\xi,h} = 262\,144$ to represent the damage variable $d_{\xi,h}^n$ at every integration point in the RVE. Computing the inelastic evolution of the elasto-plasticity model with linear hardening and damage requires in 620 loading increments 347 296 Newton iteration steps for the computation of the micro-fluctuation $\mathbf{v}_{\xi,h}^n$ and 51 691 evaluations for the effective algorithmic material tangent $\mathbb{C}_{\xi,H}^n$. For the simulation an extrapolated implicit Euler scheme with equidistant loading increment $\Delta t = 2$ was used. The simulation was performed on the ForHlr2 B.3 cluster with 512 cores distributed across 16 nodes each using 16 cores for 34 hours, 16 minutes and 5 seconds.

7.2.2 Reduced FE² method

The full simulation of the cyclic inelastic material behavior is computationally very expensive. So we reduce the amount of computations by using a full resolution in a region of interest $\Omega_{\text{ctr}} \subset \Omega$ which is also used to evaluate the stress-strain curve. Then, we use for the representation of the micro-solution $\mathbf{v}_{\xi,h}^n$ and the history variables $\mathbf{z}_{\xi,h}^n$ a fine resolution for the spaces $V_{\xi,h}$ and $Z_{\xi,h}$ in every RVE $\mathcal{Y}_{\xi} \subset \Omega_{\text{ctr}}$, and coarser spaces $V_{\xi,h}^{\text{red}}$ and $Z_{\xi,h}^{\text{red}}$ for every RVE $\mathcal{Y}_{\xi} \not\subset \Omega_{\text{ctr}}$. This leads to an increase in efficiency for the parallel FE² algorithm and thus for a speed up of the simulation of consuming component tests. An illustration of the reduced FE² approach is shown for a simple example in Figure 7.21.

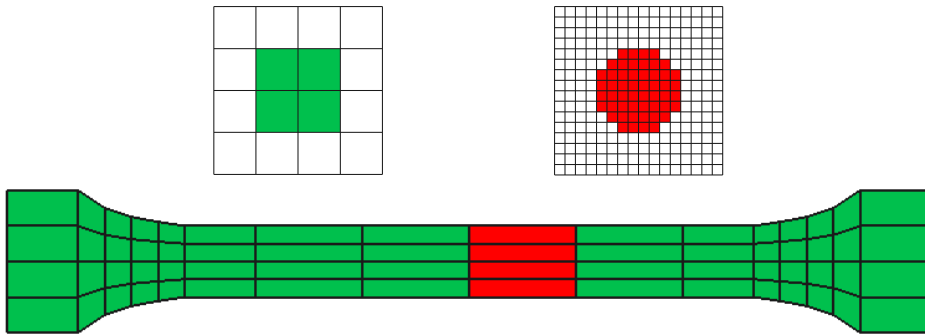


Figure 7.21: Region of interest $\Omega_{\text{ctr}} \subset \Omega$ for the reduced FE² method. Green area: Reduced microstructure resolution $V_{\xi,h}^{\text{red}}$ in every RVE $\mathcal{Y}_{\xi} \not\subset \Omega_{\text{ctr}}$ (top left). Red area: full microstructure resolution $V_{\xi,h}$ in every RVE $\mathcal{Y}_{\xi} \subset \Omega_{\text{ctr}}$ (top right).

We investigate the reduced method for the cyclic loading test with the two-scale damage model, using $\Omega_{\text{ctr}} = (0, 0.5) \times (-0.2, 0.2) \times (0, 2) \subset \Omega$ with $\dim V_{\xi,h} = 107811$ and $\dim Z_{\xi,h} = 262144$ for $\xi \in \Omega_{\text{ctr}}$ and $\dim V_{\xi,h}^{\text{red}} = 14739$ and $\dim Z_{\xi,h}^{\text{red}} = 32768$ for $\xi \notin \Omega_{\text{ctr}}$. For the representation of the macro-solution \mathbf{u}_H^n we use a discretization with 128 integration points, i.e., the region of interest contains 24 integration points which is assumed to cover the numerical area of investigation exactly for the evaluation of the stress-strain curve.

Comparing the results between the full and the reduced method in Figure 7.22 shows that they do not differ notably and thus the less accurate approximation in the RVEs outside the region of interest has only a very small influence to the averaged macroscopic solution in Ω_{ctr} . The small deviation between the reduced and full method implies the possibility to save time in computation in the exterior of critical areas in component testing. This is of great interest for the simulation of the inelastic material behavior for large component dimensions in material science and can be coupled with further reduction techniques.

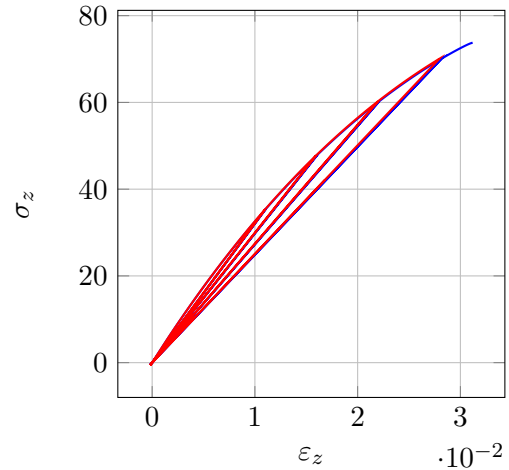


Figure 7.22: Comparison of the cyclic stress-strain curves between the reduced (blue) and full (red) two-scale method.

The simulation for $t \in [0, 938]$ of the reduced method with 938 loading increments requires 439814 Newton iteration steps for computing the micro-fluctuation $\mathbf{v}_{\xi,h}^n$ and 71731 evaluations of the effective algorithmic material response $\mathbb{C}_{\xi,H}^n$. The computation takes 45 hours, 42 minutes and 23 seconds on the IC2 B.2 cluster with 256 cores distributed on 16 nodes each using 16 cores.

7.3 Numerical convergence analysis

For the investigation of the convergence properties for the heterogeneous multiscale method we use the reduced FE^2 approach with a region of interest $\Omega_{\text{ctr}} = (0, 0.5) \times (-0.2, 0.2) \times (0, 2) \subset \Omega$. We consider the two-scale damage model with damping and yielding point parameter $H = 0.22702$ and $Y_0 = 0.08692$. In every RVE we use the same isotropic microstructure with 10% fiber volume fraction. On the macro-scale we

use a fixed approximation with $\dim V_H = 165$ and for every integration point $\xi \notin \Omega_{\text{ctr}}$ we select in every RVE coarse discretizations with $\dim V_{\xi,h}^{\text{red}} = 14\,739$ and $\dim Z_{\xi,h}^{\text{red}} = 32\,768$.

Again we extract various characteristic length scales $\delta/2^n$ of a complex microstructure, see Figure 7.23. Each extraction corresponds to one eighth of its previously microstructure by employing a bisection method and is mapped to the unite cube. This proceeding preserves the material specific properties.

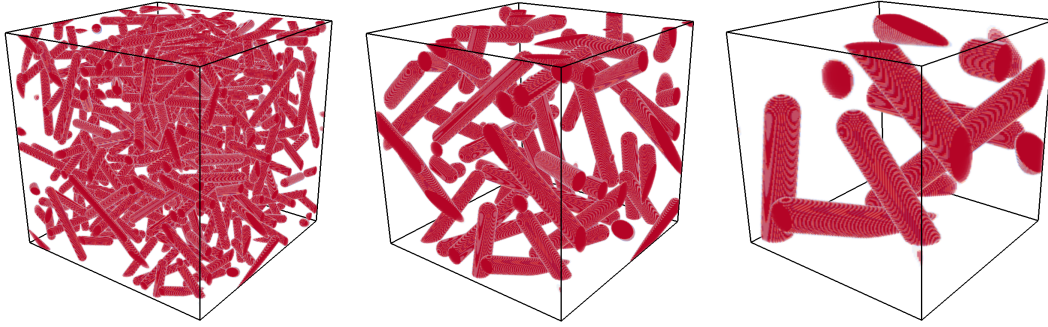


Figure 7.23: Isotropic microstructures with 10% fiber volume fraction for various characteristic length scales δ , $\delta/2$ and $\delta/4$ corresponding to their RVEs \mathcal{Y}_ξ^δ , $\mathcal{Y}_\xi^{\delta/2}$ and $\mathcal{Y}_\xi^{\delta/4}$.

Within the region of interest we evaluate the macro-stress in the Frobenius-norm $\sigma_{H,h}^{\delta/2^n} = \|\sigma_{H,h}^{\delta/2^n}\|_F$, where the macro-stress $\sigma_{H,h}^{\delta/2^n} = \int_{\Xi_H \cap \Omega_{\text{ctr}}} \sigma_{\xi,H}^{\delta/2^n}$ is defined at each integration point $\xi \in \Omega_{\text{ctr}}$ by the averaged micro-stress $\sigma_{\xi,H}^{\delta/2^n} = \frac{1}{|\mathcal{Y}_\xi^{\delta/2^n}|} \int_{\mathcal{Y}_\xi^{\delta/2^n}} \mathbb{C}(\mathbf{x})[\varepsilon_{\xi,H} + \varepsilon(\mathbf{v}_{\xi,h})] d\mathbf{x}$ depending on $\varepsilon_{\xi,H}^n = \varepsilon(\mathbf{u}_H^n)(\xi)$. For the evaluation of the results, we use the extrapolation $\sigma_{H,\text{ex}_h}^{\delta/2^n}$ in (4.4) which is obtained by the mean value of the determined experimental order of convergence p in (4.2) and the relative error $e_{H,\text{rel}_h}^{\delta/2^n}$ in (4.5).

The results of the numerically determined value $\sigma_{H,h}^{\delta/2^n}$, the relative error $e_{H,\text{rel}_h}^{\delta/2^n}$ corresponding to their extrapolated values $\sigma_{H,\text{ex}_h}^\delta = 61.5507$, $\sigma_{H,\text{ex}_h}^{\delta/2} = 54.4619$ and $\sigma_{H,\text{ex}_h}^{\delta/4} = 45.7693$ are listed in Table 7.1. Comparing with the classical two-scale homogenization method for linear elasticity confirm the results towards the inelastic heterogeneous multiscale method with a reduced FE² methodology, cf. Table 4.1, 4.2, 4.3 and Figure 4.11. But we observe that in the inelastic case due to damage in the RVE with different characteristic length scales δ , $\delta/2$ and $\delta/4$ the material response is considerably different. The slope of the double logarithmic scale plot of the numerically determined error $e_h^{\delta/2^n} = \sigma_{H,h}^{\delta/2^n} - \sigma_{H,\text{ex}_h}^{\delta/2^n}$ against the grid size h in Figure 7.24 shows the asymptotic convergence rate of the parallel finite subroutines on the micro-scale which is almost linear, except for a heterogeneity scale with $\delta/4$ which decreases for finer discretization.

In each convergence test we computed 26 loading increments. In 17 loading increments the material response was inelastic in every integration point of the specimen. All convergence tests were performed on the DELTA B.1 and ForHlr2 B.3 cluster with up to 512 cores.

DoFs	$\sigma_{H,h}^\delta$	e_{H,rel_h}^δ	$\sigma_{H,h}^{\delta/2}$	$e_{H,rel_h}^{\delta/2}$	$\sigma_{H,h}^{\delta/4}$	$e_{H,rel_h}^{\delta/4}$
375	95.7385	55.54	73.7455	35.41	63.5587	38.87
2 187	89.5396	45.47	75.7307	39.05	55.7936	21.90
14 739	85.2059	38.43	64.9883	19.37	50.7798	10.95
107 811	72.8031	18.28	59.3220	8.92	48.3919	5.73
823 875	66.6792	8.33	56.7448	4.19	47.3729	3.50
6 440 067	63.9545	3.91	55.5575	2.01	46.6539	1.93

Table 7.1: Numerical results of $\sigma_{H,h}^{\delta/2^n}$ and the relative error $e_{H,rel_h}^{\delta/2^n}$ for uniform mesh refinements on the micro-scale for $\mathcal{Y}_\xi \subset \Omega_{inv}$ and a fixed macro-scale discretization with $\dim V_H = 165$ for the inelastic heterogeneous multiscale method using a reduced FE^2 approach.

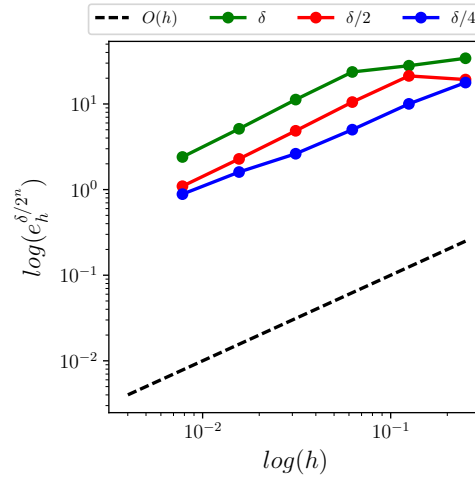


Figure 7.24: Estimated rate of convergence for various scales of heterogeneities $\delta/2^n$ for $n \in \{0, 1, 2\}$ on the micro-level for uniform mesh refinements. The dashed line $O(h)$ indicates the slope of a linear rate.

Chapter 8

Implementation

The implementation of the FE^2 algorithm as introduced in Section 6.3 is discussed in more detail with the focus on optimization issues. Computing the inelastic material behavior is highly complex due to the multiscale character of the problem. Solving this problem can be speed up immensely by parallelization of the algorithm. The algorithm was realized by an FE^2 approach which computes all elements of the macro-scale in parallel. Each sample point on the macro-scale is divided into multiple parallelized micro-scale problems. All micro-scale problems are then computed sequentially to prevent running multiple parallel finite element subprograms at the same time, i.e. each subprogram is efficiently accessed with the maximum available number of cores by using a multigrid method with a highly scalable coarse grid solver. Nevertheless, the introduced FE^2 algorithm transfers to hierarchical architectures mixing different parallel paradigms. In addition to the computational power, limited working memory poses another major bottleneck. In order to address the working memory issue, appropriate data structures and strategies for storage reductions are introduced.

The algorithm was implemented in C++ and the M++ framework was used for computing finite element routines in parallel. For a distributed memory communication the *message passing interface* (MPI) was used. MPI provides collective communication and synchronization techniques.

8.1 Parallel two-scale data structure

In this section an appropriate two-scale data structure is introduced for a parallel implementation of the FE^2 algorithm (see Section 6.3) and parallelization issues of the software package M++ are addressed. The challenging task is the communication and administration of data distributed across multiple finite element subprograms working in parallel.

8.1.1 The parallelization scheme

The parallelization within the M++ framework for distributed memory allocation is realized by a geometric load balancing procedure. According to the recursive coordinate bisection algorithm [66], the geometry is divided in each spatial direction by its elements and balanced distributed across all processes using MPI. This allows the definition of a consistent local domain decomposition and transfers to various data structure techniques.

8.1.2 The two-scale data structure

The two-scale data structure serves as an interface for the communication of various data values between multiple parallel finite element subprograms. For efficiency reasons, a locally decomposed storage technique as discussed above was used to realize the two-scale data structure in terms of an unordered map. Unordered maps are associative containers and allow fast access to values addressed via uniquely identified keys. The value lookup has average constant time complexity $O(1)$ and in the worse case of collisions it degenerates to linear time complexity $O(N)$, where N denotes the entity of elements stored in the hash map. For the inelastic two-scale algorithm of rate-independent materials, as introduced in Section 6.3, the dataset of a single finite element subprogram defines the two-scale data type by

$$(\mathbf{v}_{\xi,h}^n, \mathbf{z}_{\xi,h}^n, \mathbb{C}_{\xi,H}^n, \boldsymbol{\varepsilon}_{\xi,H}^n, \boldsymbol{\sigma}_{\xi,H}^n) \in V_{\xi,h} \times Z_{\xi,h} \times \mathbb{R}_{\text{sym}}^{6 \times 6} \times \mathbb{R}_{\text{sym}}^{3 \times 3} \times \mathbb{R}_{\text{sym}}^{3 \times 3}.$$

The two-scale data structure then is introduced by the solution of the finite element subprogram at each sample point $\xi \in \Xi_H$ of the main finite element routine and can be written as

$$\mathcal{M}_{\xi \in \Xi_H} = \{(\mathbf{v}_{\xi,h}^n, \mathbf{z}_{\xi,h}^n, \mathbb{C}_{\xi,H}^n, \boldsymbol{\varepsilon}_{\xi,H}^n, \boldsymbol{\sigma}_{\xi,H}^n) \in V_{\xi,h} \times Z_{\xi,h} \times \mathbb{R}_{\text{sym}}^{6 \times 6} \times \mathbb{R}_{\text{sym}}^{3 \times 3} \times \mathbb{R}_{\text{sym}}^{3 \times 3}\}.$$

It turns out that a two-scale data structure representation by the full set of data values of the multiple parallel finite element subprograms is too wasteful and may be infeasible for working memory issues, in particular for the simulation of large component dimensions. In the following sections different improvement strategies are discussed and their implementation is outlined.

8.1.3 A storage reduced two-scale data structure

A storage optimized two-scale data structure is introduced here, based on the assumption that just a few sample points exhibit an inelastic material response. This is achieved

by designing a data structure which dynamically allocates storage depending on whether a material points response on the macro-level is elastic or it is irreversibly inelastic after exceeding the yield limit. For more efficiency we address the computation of the elastic responses in detail.

If a material point behaves elastic, then for a subset Ξ_H^{active} of active sample points with different microstructure, the once precomputed 6 micro-fluctuations $\mathbf{w}_{\xi,h,1}, \dots, \mathbf{w}_{\xi,h,6}$ define the elastic responses of the upscaled two-scale tensor $\mathbb{C}_{\xi,H}$, the micro-solution $\mathbf{v}_{\xi,h}^n$ and the averaged stress response $\boldsymbol{\sigma}_{\xi,H}^n$, see Section 3.2.6. For an increase in efficiency the effective two-scale tensor $\mathbb{C}_{\xi,H}$ can be precomputed once, whereas the micro-solution $\mathbf{v}_{\xi,h}^n$ and the stress response $\boldsymbol{\sigma}_{\xi,H}^n$ have to be evaluated in each material point and loading increment by the time depending strain response $\boldsymbol{\varepsilon}_{\xi,H}^n$. Finally, the dependencies summarized define the elastic two-scale data type by the following dataset

$$(\mathbf{w}_{\xi,h,1}, \dots, \mathbf{w}_{\xi,h,6}, \mathbb{C}_{\xi,H}, \boldsymbol{\varepsilon}_{\xi,H}^n) \in V_{\xi,h} \times \dots \times V_{\xi,h} \times \mathbb{R}_{\text{sym}}^{6 \times 6} \times \mathbb{R}_{\text{sym}}^{3 \times 3}.$$

This data type defines, for every different microstructure, at each elastic sample point $\xi \in \Xi_H^{\text{elastic}}$ the elastic two-scale data structure

$$\begin{aligned} \mathcal{M}_{\xi \in \Xi_H^{\text{elastic}}} &= \left\{ \boldsymbol{\varepsilon}_{\xi,H}^n \in \mathbb{R}_{\text{sym}}^{3 \times 3} : \mathbf{v}_{\xi,h}^n = \sum_{j=1}^6 (\boldsymbol{\varepsilon}_{\xi,H}^n : \boldsymbol{\eta}_j) \mathbf{w}_{\xi,h,j}, \quad \mathbb{C}_{\xi,H}^n = \mathbb{C}_{\xi,H} \right. \\ &\quad \left. \text{and } \boldsymbol{\sigma}_{\xi,H}^n = \mathbb{C}_{\xi,H} : \boldsymbol{\varepsilon}_{\xi,H}^n \quad \text{for } (\mathbf{w}_{\xi,h,1}, \dots, \mathbf{w}_{\xi,h,6}, \mathbb{C}_{\xi,H}) \in \mathcal{M}_{\xi \in \Xi_H^{\text{active}}} \right\}. \end{aligned}$$

The dataset of the precomputed data values of the 6 micro-fluctuations and the two-scale tensor is only stored for a subset Ξ_H^{active} of active sample points with different microstructure and is defined in an external data structure

$$\mathcal{M}_{\xi \in \Xi_H^{\text{active}}} = \{(\mathbf{w}_{\xi,h,1}, \dots, \mathbf{w}_{\xi,h,6}, \mathbb{C}_{\xi,H}) \in V_{\xi,h} \times \dots \times V_{\xi,h} \times \mathbb{R}_{\text{sym}}^{6 \times 6}\}.$$

In the event a material point becomes irreversibly inelastic a complete elasto-plastic computation routine of multiple parallel finite element subroutines must be performed to determine the inelastic material behavior. The dataset of these subroutines defines the inelastic data type by

$$(\mathbf{v}_{\xi,h}^n, \mathbf{z}_{\xi,h}^n, \mathbb{C}_{\xi,H}^n, \boldsymbol{\varepsilon}_{\xi,H}^n, \boldsymbol{\sigma}_{\xi,H}^n) \in V_{\xi,h} \times \dots \times V_{\xi,h} \times \mathbb{R}_{\text{sym}}^{6 \times 6} \times \mathbb{R}_{\text{sym}}^{3 \times 3} \times \mathbb{R}_{\text{sym}}^{3 \times 3},$$

and thus the two-scale data structure for each inelastic sample point $\xi \in \Xi_H$ is defined by the set

$$\mathcal{M}_{\xi \in \Xi_H^{\text{inelastic}}} = \{(\mathbf{v}_{\xi,h}^n, \mathbf{z}_{\xi,h}^n, \mathbb{C}_{\xi,H}^n, \boldsymbol{\varepsilon}_{\xi,H}^n, \boldsymbol{\sigma}_{\xi,H}^n) \in V_{\xi,h} \times Z_{\xi,h} \times \mathbb{R}_{\text{sym}}^{6 \times 6} \times \mathbb{R}_{\text{sym}}^{3 \times 3} \times \mathbb{R}_{\text{sym}}^{3 \times 3}\}.$$

Finally, combining all elastic and inelastic data values defines the two-scale data structure:

$$\mathcal{M}_{\xi \in \Xi_H} = \mathcal{M}_{\xi \in \Xi_H^{\text{elastic}}} \cup \mathcal{M}_{\xi \in \Xi_H^{\text{inelastic}}}.$$

This abstract description for a parallel two-scale data structure using the same microstructure for each RVE is realized in the following hierarchical storage units:

```
class TwoScaleSPs : public hash_map<SP,TwoScaleSP,Hash> {
    const TwoScaleTensor& TsT_lin;
    const Vector& w_lin[6];
    ...}
```

Here, we store the once precomputed 6 linear micro-fluctuations `w_lin[6]` and the two-scale tensor `TsT_lin`, which can simply be extended to various microstructures by realizing a data structure which dynamically allocates the 6 micro-fluctuations and the two-scale tensor for each different microstructure. The two-scale data type at each sample point completes the previously discussed elastic and inelastic data type by means of dynamical storage units:

```
class TwoScaleSP {
    Tensor Strain_H;
    TwoScaleTensor* TsT;
    Tensor* Stress_H;
    Vector* v_h;
    SPDamageHistory* DH;
    SPPlasticityHistory* PH;
    ...}
```

For flexibility, the two-scale data structure can be extended easily through various inelastic effects described by the internal variable of different material models. In addition to the dynamic allocation of inelastic effects, memory can further be reduced by using hash tables, discussed in detail in the next section, for representing the internal variable of various material models such as damage `SPDamageHistory` and plasticity `SPPlasticityHistory`.

8.2 Strategies for data and storage reduction

Here, we consider a further reduction in working memory. In particular we focus on a reduced representation of the internal variable and an approach for a parallel internal specification of the microstructure. In addition, we introduce the realization of an RVE microstructure interface.

8.2.1 A reduced internal variable representation

The optimization in memory for the representation of the internal variable without the memory consuming representation by a one-dimensional array is clarified with the aid of an example. Therefore, a composite with a certain percentage volume share of glass fiber firmly embedded in a polymer carrier matrix is considered. Owing to the fact that within the fiber no inelastic evolution takes place, the representation of the internal variable contains at least a certain percentage share of entries with value zero. Generally, it is not efficient to store all the non-zero values of a sparse vector in a one-dimensional array. To address this issue, a dynamic data structure for a storage reduced internal variable representation was developed. Efficiency can be achieved by using locally distributed hash tables, see Section 8.1.2. At runtime, memory is only allocated if a material point on the micro-scale becomes inelastic, i.e. when accessing the hash table, it returns the internal variable value for each inelastic material point, otherwise no key can be found and it returns by default the value zero. However, this realization transfers to all hierarchical accessed sub-meshes of the multigrid method and allows a significant memory reduction. Furthermore, a modular implementation of the internal variables allow a flexible combination of various inelastic material models such as plasticity and damage which have been realized in the following storage units:

```
class SPDamageHistory : public hash_map<Point,DamageHistory,Hash>
class SPPlasticityHistory : public hash_map<Point,PlasticityHistory,Hash>
```

With the focus on memory optimization the data type of the internal variables of damage and plasticity are realized by using dynamical storage units:

```
class DamageHistory {
    double* d_h;
    ...}

class PlasticityHistory {
    Tensor* Strain_p;
    double* r_h;
    ...}
```

8.2.2 Interface for the representation of the microstructure

The description of various microstructures in every RVE requires a flexible interface. For this purpose, we use an octree based interface provided by the Fraunhofer ITWM. Here, we introduce the functionality of the interface and the generation of the microstructures.

Apart from fiber length and diameter, the information required for reconstructing a material composition is the distribution of the fiber within the carrier matrix. The distribution of the fiber, caused by the injection molding process, can be studied by computed tomography scans of the cross sectional specimen area.

All the used microstructures are generated stochastically by the software package GeoDict [20] and are made available by the Fraunhofer ITWM. In order to describe a microstructure voxel images are used. Each voxel is represented by a number and serves as an identification for the subdomain of the microstructure. For a storage efficient representation the voxel image is transformed into an octree container. The octree compresses the voxel image by dividing it into homogeneous subdomains by employing a bisection approach until each subdomain is homogeneous. This is simplified illustrated for a two-dimensional microstructure by an quadtree compression of a pixel image as illustrated in Figure 8.1 and 8.2.

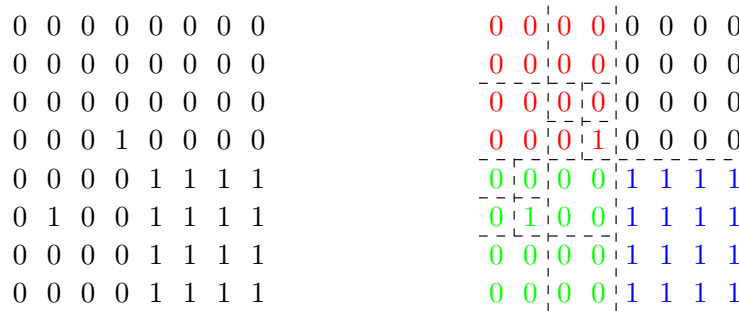


Figure 8.1: Visualization of a quadtree compression. Left: Two-dimensional representation of a microstructure by a pixel image. Right: Final compression: The blue and black subdomains are stored as single value 1 and 0. On the other side the red and green subdomains are further subdivided until each subdomain is homogeneous.

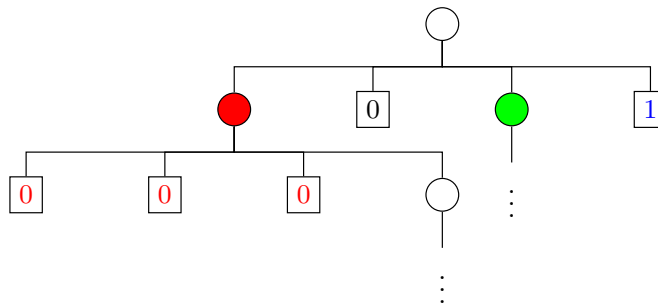


Figure 8.2: Quadtree container compression of a pixel image as shown in Figure 8.1. Each leaf node (square) represents a homogeneous divided subdomain of its parent node (circle).

8.2.3 Working memory efficient microstructure representation

Now, an efficient and flexible way for the parallelization of the microstructure geometry is proposed. The microstructures are stored externally in octree compressed voxel images and accessed by an octree interface as described in the previous Section 8.2.2.

The voxel images are imported on the master process into an octree container, which stores the geometry memory efficient in a tree structure. Then, the master process distributes this container among all slave processes by using collective communication and synchronization techniques provided by MPI. However, a full representation of the geometry on each process is not efficient in the usage of working memory, because each process requires solely a small part of the microstructure. For this purpose, a geometrically load balanced hash table (see Section 8.1.1) for each different microstructure is used. After initialization of the locally distributed hash tables, the octree container memory can be released on each single process. This allows an efficient representation of the microstructure.

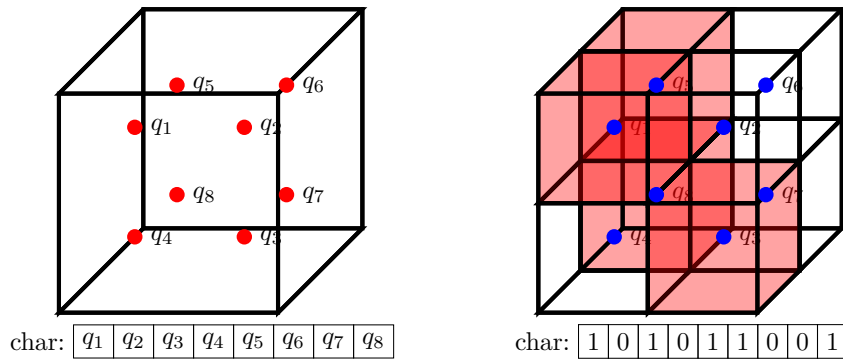


Figure 8.3: Left: Hexahedral finite volume cell with eight integration points (top) and its bitwise data type representation of a hexahedron by a character (bottom). Right: Voxel representation of the subdomain geometry for a hexahedral finite volume cell (top) and its bitwise allocation by the subdomain (bottom).

During the initialization of the local hash tables, memory consumption can be further optimized. Exact integration by linear approximation allows representing the hexahedron by 8 subdomains. A single bit can be used to define if a subdomain contains a fiber or not. In order to describe the values of the 8 subdomains of a hexahedral cell a single variable of type character can be used. However, a character is only allocated and stored in the hash table if at least one subdomain of the hexahedral cell contains a fiber. If a key is not found in the hash table, no fiber exists in the hexahedron and thus the value of 0 is returned by default. The unique bitwise identification of a hexahedral finite volume

cell with linear approximations by its integration points is illustrated on the left hand side in Figure 8.3. The right hand side in Figure 8.3 shows exemplarily the bitwise representation of the subdivided hexahedral volume cell around each integration point in eight voxels representing the subdomain. If the situation arises that the fiber volume share exceeds 50%, then it is useful to identify the geometry of the microstructure by the carrier matrix volume fraction.

Chapter 9

Conclusion and outlook

9.1 Summary and main results

The goal of this thesis was to develop an efficient algorithm for the simulation of the elastic and the inelastic behavior for rate-independent materials with a very complex microstructure due to a small scale of heterogeneity. For this purpose, we presented a heterogeneous multiscale method based on an FE^2 approach that works massively in parallel. More efficiency is achieved by using a multigrid method with a highly scalable periodic coarse grid solver for accelerating the many computations on the micro-scale.

In order to describe the micromechanical processes of a polymer with firmly embedded glass fiber phenomenologically, we discussed different continuum mechanics material models and compared some results with real engineering applications. In several numerical experiments we were able to detect material specific properties of the fiber orientation stemming from the injection molding process by monotonic and cyclic uniaxial component testing. To determine a good choice for the resolution of the microstructure, used to determine the micromechanical proceedings sufficiently enough, we examined the convergence properties for the classical homogenization method for the small strain two-scale elasticity. Finally, we verified the results of the convergence investigation for the classical homogenization method of the two-scale elasticity towards the inelastic heterogeneous multiscale method using an FE^2 approach for the rate-independent simple two-scale damage model.

The parallel implementation of the FE^2 method was realized in flexible modules and transfers to a large variety of multiscale models by an appropriate two-scale data structure. Besides the high amount of computational power, the required amount of working memory is another drawback in conventional algorithms. For this reason, we presented some strategies for reducing memory consumption of the algorithm. Particularly the treatment of short fiber-reinforced polymers allows a reduction for the representation of

the internal variable within the parallel implementation. Furthermore, a parallel memory optimized realization of an efficient and flexible interface for the import of various microstructures was presented.

9.2 Outlook and further applications

The sequentially realized parallel FE² approach can be executed on hierarchical parallel architectures mixing different parallel paradigms. Despite the parallel implementation, the computation of a fully coupled approach is challenging. For large component dimensions the many boundary value problems represented by the RVE on the micro-scale are costly to solve. An adaptive combination of various homogenization techniques can be a possible solution to this problem. The simplest way is the coupling of the heterogeneous multiscale method with simple analytical homogenization schemes in non critical macro-areas. Configurational forces can be used to identify critical areas, e.g. see [31, 45]. Moreover, the quantification of critical sample points can also be used for the region of interest to extend the presented reduced FE² approach by adaptivity.

In order to accelerate the computation, [1] proposed offline precomputing of intermediate results for the online multiscale simulation for the RVE. A reduced basis for the RVE is constructed in an offline stage using a greedy algorithm. In the online stage the once precomputed reduced basis space is then used to determine the effective response. A new reduced basis is only performed if the computation becomes numerically unstable.

Within the treatment of thermoplastic engineering composites a further application field is the incorporation of rate-dependent material effects for extending viscoelastic properties in component testing. Another application within this field is the transition of micro cracks from the corresponding RVE to its sample point to fractures on the macro-scale through an appropriate coupling.

Other application fields include among other things the treatment of the flow of rainwater through a porous medium as discussed in Section 1.1, the poro elasticity in biomechanics or the poro elasto-plasticity model frequently used in soil mechanics.

Appendix A

Fundamental tools from convex analysis and optimization

This thesis relies on using semi-smooth unconstrained optimization problems, which provide necessary tools required for evaluating the flow rule of a rate-independent material. Before this is discussed in detail, the necessity for treating the specific problems is motivated.

In this thesis we discuss an energetic framework described by the total energy $\mathcal{E}(t, \mathbf{u}, \mathbf{z})$ whose evolution is restricted by the dissipation potential $\mathcal{R}(\dot{\mathbf{z}})$. The dissipation potential $\mathcal{R}(\dot{\mathbf{z}})$ determines the set of admissible thermodynamic states. By construction, the plastic dissipation $\mathcal{R}(\dot{\mathbf{z}})$ coincides with an indicator function and serves as a penalty term. Thus, the evolution of the history variable \mathbf{z} is equivalent to a semi-smooth unconstrained optimization problem defined by the flow rule $-\partial_{\mathbf{z}}\mathcal{E}(t, \mathbf{u}, \mathbf{z}) \in \partial\mathcal{R}(\dot{\mathbf{z}})$. This means we need to study by duality a generalization concept of ordinary differential equations of the type of a differential inclusion $\dot{\mathbf{z}} \in \partial\mathcal{R}^*(\mathbf{z})$. Since the dissipation potential coincides with an indicator function of a convex set the plastic potential \mathcal{R}^* is an indicator function $\chi_C(\dot{\mathbf{z}})$ corresponding to the set of admissible states $C = \{\mathbf{y} \in \mathbb{R}^N : \mathcal{F}(\mathbf{y}) \leq 0\}$ of thermodynamic forces $\mathbf{y} = -\partial\mathcal{E}(t, \mathbf{u}, \mathbf{z})$. The principle of maximum dissipation described by the support function of the plastic potential \mathcal{R} is an optimization problem of exact the same type, see Section 2.3.3.

For more details in optimization theory and the existence of optimal solutions, the reader is referred to the books of Ekeland and Témam [16], Geiger and Kanzow [19] and Jarre and Stoer [26].

A.1 Optimality conditions for semi-smooth unconstrained problems

The goal of this approach is to find a solution of a constrained optimization problem for a closed, convex and nonempty set $C \subset V$ of a finite dimensional vector space $V = \mathbb{R}^N$ with inner product $\langle \cdot, \cdot \rangle$ and a sufficiently smooth objective function $f : V \rightarrow \mathbb{R}$ of the form

$$\min f(x) \quad \text{subject to } x \in C. \quad (\text{A.1})$$

This raises the question of how to deal with constraints in the optimization theory. An easy way of doing this is to transform the constrained situation into a well known unconstrained optimization problem. For that reason we introduce the indicator function for a set $C \subset V$, which has an infinite jump for any point on the boundary of C and thus is highly non-smooth, at a point $x \in V$ by

$$\chi_C(x) = \begin{cases} 0 & x \in C, \\ +\infty & \text{otherwise.} \end{cases}$$

It can easily be seen that the indicator function of a convex set is convex itself. Then, with the indicator function as penalty term, we can define the augmented function

$$f(x) + \chi_C(x) = \begin{cases} f(x) & x \in C, \\ +\infty & \text{otherwise.} \end{cases}$$

With this construction we are able to rewrite above constrained optimization problem (A.1) as an unconstrained optimization problem of the following type

$$\min f(x) + \chi_C(x) \quad \text{subject to } x \in V. \quad (\text{A.2})$$

The sum of the objective function f with the penalty term χ_C is non-differentiable. For this purpose we suppose in the following that the objective function f is a uniformly convex function and that $C \subset V$ is a closed convex set and thus by the Proposition [16, Chap. I, Prop. 2.3] the indicator function is lower semi-continuous. Altogether for a convex, closed and nonempty set the indicator function is proper, convex and lower semi-continuous. Then, a minimizer $x \in V$ exists if and only if zero lies in the set of subgradients belonging to the augmented function, which can be confirmed by the Moreau-Rockafellar formula [16, Chap. I, Prop. 5.6] as the sum of two convex sets, expressed by

$$0 \in \nabla f(x) + \partial \chi_C(x).$$

Here, the fact is used, that the set of all subgradients $z \in V$ denoted by the subdifferential $\partial f(x) = \{z \in V : \langle z, y - x \rangle + f(x) \leq f(y) \text{ for all } y \in C\}$ of a convex and differentiable function $f : V \rightarrow \mathbb{R}$ at $x \in V$ is subdifferentiable at $x \in V$ with $\partial f(x) = \{\nabla f(x)\}$. The application of the subdifferential to a convex indicator function at a point $x \in V$ is determined by the set of all subgradients $z \in V$ such that

$$\partial \chi_C(x) = \{z \in V^* : \langle z, y - x \rangle \leq 0 \text{ for all } y \in C\} = \begin{cases} N_C(x) & x \in C, \\ \emptyset & \text{otherwise.} \end{cases}$$

Here, we denote the normal cone $N_C(x) = \{z \in V^* : \langle z, y - x \rangle \leq 0 \text{ for all } y \in C\}$ for a convex set $C \subset V$ as the set of all vectors y normal to the set C at point x .

A.1.1 First order optimality condition

The application of the Moreau-Rockafellar formula delivers a necessary and, in case of convexity, a sufficient condition for an optimal solution of the unconstrained optimization problem (A.2) represented in the following theorem.

Theorem A.1

Let $f : V \rightarrow \mathbb{R}$ be a differentiable function and let $C \subset V$ be a nonempty convex set, then a necessary condition for an optimal solution $x \in C$ of the unconstrained semi-smooth optimization problem (A.2) exists if and only if

$$-\nabla f(x) \in N_C(x).$$

If f is also convex, then the condition becomes sufficient.

Proof. By application of the Moreau-Rockafellar formula and the definition of the normal cone holds that $-\nabla f(x) \in N_C(x)$ if and only if $\langle \nabla f(x), y - x \rangle \geq 0$ for each $y \in C$. \square

Especially, this thesis discusses a specific closed convex set C generated by inequality constraints $g(x) \leq 0$. Therefore, we have to guarantee that the properties of the convex closed set C remain valid to ensure the assumptions of the Moreau Rockafellar formula hold true. It can easily be seen that this is true, when the set generating function g is proper, convex and lower semi-continuous. As consequence to this fact we can state the following theorem, which points to be a very useful interface relating to the geometric and analytic point of view in optimization theory.

Theorem A.2

Suppose that the function $g : V \rightarrow \mathbb{R} \cup \{+\infty\}$ is proper, convex and lower semi-continuous with $0 \notin \partial g(x)$, then the normal cone of a convex set $C = \{x \in V : g(x) \leq 0\}$ with inequality constraints is determined by

$$N_C(x) = \begin{cases} \{0\} & \text{if } g(x) < 0, \\ \emptyset & \text{if } g(x) > 0, \\ \{\lambda \partial g(x) : \lambda \geq 0\} & \text{if } g(x) = 0. \end{cases}$$

Proof. We notice that, by convention, $N_C(x) = \emptyset$ holds for the normal cone for any point x not belonging to the set C .

At first we will show, if the point x lies in the interior of the set C , that $N_C(x) = \{0\}$ holds for the normal cone of the set C . This part will be shown by contradiction. By definition of the normal cone holds that $0 \in N_C(x)$. Now, we assume that there exists a point $p \in N_C(x)$ with $p \neq 0$. For any different point x in the interior of C and a constant $\alpha > 0$ sufficiently small we define the feasible direction $y = x + \alpha p$, which belongs to C . For this reason the inequality $0 \geq \langle p, y - x \rangle = \alpha \|p\|^2$ is only fulfilled for $p = 0$, which in turn contradicts the assumptions.

Finally we will show, that $N_C(x) = \{\lambda \partial g(x) : \lambda \geq 0\}$ holds for the normal cone of a convex set with inequality constraints $C = \{x \in V : g(x) \leq 0\}$. The sublevel set $C = \{x \in V : g(x) \leq 0\}$ of a convex function g is convex itself. Then, we will show, if x lies on the boundary of the set C , that $N_C(x) = \lambda \partial g(x)$ for some $\lambda \in \mathbb{R}_{\geq 0}$ holds for the normal cone. The boundary of a convex sublevel set $C = \{x \in V : g(x) \leq 0\}$ is denoted by the level curve of the active set $C_{\mathcal{A}} = \{x \in V : g(x) = 0\}$. Therefore, the supporting hyperplane at a boundary point x_0 in the active set $C_{\mathcal{A}}$ is the tangent plane, which in turn can be expressed by the graph of the first order Taylor expansion that is defined by $\nabla g(x_0)(y - x_0)$, whereas the gradient $\nabla g(x_0)$ is characterized as the normal of the boundary at point x_0 . Should the situation arise that the boundary point is non-smooth, then by the subdifferentiability of a convex function, the normal cone is generated by the set of all subgradient rays $\{\lambda \nabla g(x_0)\}$ with $\lambda \geq 0$ at point x_0 in the set of the active inequality constraints $C_{\mathcal{A}}$ of the lower semi-continuous function g . Finally, this leads to the definition of the normal cone by $N_C(x_0) = \overline{\text{con}}(C - \{x_0\}) = \overline{\text{con}}(\partial g(x_0)) = \text{cl}(\mathbb{R}_{\geq 0} \partial g(x_0))$. \square

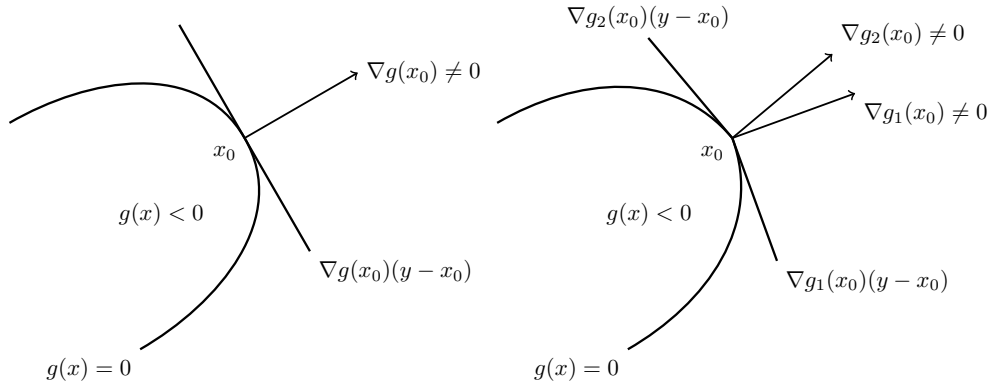


Figure A.1: Left: The function $g(x)$ is differentiable. Then, the subdifferential is defined by the one-pointed set of the gradient $\nabla g(x_0)$. Right: The function $g(x)$ is non-differentiable in point x_0 such that the gradients $\nabla g_1(x_0)$ and $\nabla g_2(x_0)$ generate the set $\partial g(x_0)$.

Theorem A.2 in combination with the optimality condition of Theorem A.1 clearly states an unconstrained optimization problem for any point in the interior of the feasible region $g(x) < 0$ and Fermat's generalized Theorem of stationary points $\nabla f(x) = 0$ for each differentiable function $f : V \rightarrow \mathbb{R}$ must be valid to be a local optimum $x \in V$ of the objective function f . On the other hand the first order optimality condition for a local optimum $x \in C$ and differentiable function f in combination with a lower semi-continuous function g at point x can be expressed, if the level set $g(x) = 0$ is active and the parallelity condition

$$-\nabla f(x) \in \lambda \partial g(x) \quad \text{for some } \lambda \in \mathbb{R}_{\geq 0}$$

holds true in the sense of subdifferentiability. An illustration of the non-smooth optimality condition is presented on the right hand side in Figure A.1.

A.1.2 Existence of solutions

The conclusions of the previous Section A.1.1 for a continuously differentiable and uniformly convex function $f : V \rightarrow \mathbb{R}$ and a proper, convex and lower semi-continuous function $g : V \rightarrow \mathbb{R}$ immediately leads us to introduce the complementary slackness condition $\lambda \geq 0$, $g(x) \leq 0$ and $\lambda g(x) = 0$ to guarantee optimality for the restated unconstrained optimization problem (A.2) by the semi-smooth Lagrangian functional $\mathcal{L} : V \times \mathbb{R} \rightarrow \overline{\mathbb{R}}$ defined by

$$\mathcal{L}(x; \lambda) = f(x) + \lambda g(x) \quad \text{for some } \lambda \geq 0.$$

This treatment results in the definition of the Karush-Kuhn-Tucker (KKT) conditions

$$\begin{aligned} 0 &\in \nabla f(x) + \lambda \partial g(x), \\ \lambda g(x) &= 0, \\ g(x) &\leq 0, \\ \lambda &\geq 0. \end{aligned}$$

A point fulfilling this condition is called a KKT-point.

Now, we propose a crucial theorem in mathematical optimization which collects above conclusions to a sufficient first order optimality condition.

Theorem A.3

Suppose that the function $f : V \rightarrow \mathbb{R}$ is uniformly convex and $g : V \rightarrow \mathbb{R}$ is proper, convex and lower semi-continuous, then a global optimal solution $x \in V$ exists of the optimization problem (A.1) if there exists a Lagrange multiplier $\lambda \in \mathbb{R}_{\geq 0}$ such that (x, λ) is a KKT-point.

Proof. If (x, λ) is a KKT point, it is a saddle point of the Lagrangian functional \mathcal{L} , i.e.

$$\mathcal{L}(x; \mu) \leq \mathcal{L}(x; \lambda) \leq \mathcal{L}(y; \lambda) \quad \text{for each } y \in V \text{ and } \mu \geq 0.$$

Then, with $\lambda g(x) = 0$ and $g(y) \leq 0$ it follows that $f(x) \leq f(y)$ for all $y \in V$. \square

However, each continuously differentiable and convex function $g : V \rightarrow \mathbb{R} \cup \{+\infty\}$ is also a proper, convex and lower semi-continuous function with the property that the subdifferential coincides with a one-pointed set of the gradient, i.e. $\partial g(x) = \{\nabla g(x)\}$, and thus, for $\nabla g(x) \neq 0$, the parallelity inclusion of the KKT-condition becomes an equation

$$-\nabla f(x) = \lambda \nabla g(x) \quad \text{for some } \lambda \in \mathbb{R}_{\geq 0},$$

as illustrated on the left hand side in Figure A.1.

This concept is applied for evaluating the differential inclusion of the incremental flow rule for designing an appropriate algorithm to determine the nonlinear material evolution. Due to the energetic formulation of rate-independent materials discussed in the thesis, it can be used for an existence and uniqueness statement of a solution for the discretized problem.

Appendix B

Hardware Specification

All the simulations and numerical experiments for the elastic and inelastic parallel FE² approach in this thesis have been performed using one of the following clusters. On all clusters the GCC version 6 and OpenMPI version 1.8.x was used.

B.1 DELTA Cluster MA-PDE

Hardware specification:

- Operating system: Ubuntu 16.04.2 LTS
- Network: InfiniBand 4X QDR Interconnect
- Main memory (in total): 1.8 TB
- Cores (in total): 320
- Nodes (in total): 8

Node specification:

- 6 thin nodes each with 32 cores, each node being equipped with an AMD Opteron 6274 processor with a frequency of 2.2 GHz and 128 GB RAM,
- 2 fat nodes each with 64 cores, each node being equipped with an AMD Opteron 6376 processor with a frequency of 1.4 GHz and 512 GB RAM

B.2 Institute Cluster IC2

Hardware specification:

- Operating system: Suse Linux Enterprise (SLES) 11

- Network: InfiniBand 4X QDR Interconnect
- Main memory (in total): 32.6 TB
- Peak performance (theoretical in total): 162 TFLOPS
- Cores (in total): 7 872
- Nodes (in total): 497

Node specification:

- 10 service nodes, 2 login nodes and 480 thin nodes each node being equipped with 16 cores, and each node has 2 Octa-Core Intel Xeon E5-2670 processors with a frequency of 2.6 GHz and 64 GB RAM, 5 × 1 TB local HDD (service nodes) and 2 × 1 TB (thin nodes) with 332.8 GFLOPS theoretical top performance
- 5 fat nodes each with 32 cores, each node being equipped with 4 Octa-Core Intel Xeon E7-8837 processors with a frequency of 2.67 GHz and 512 GB RAM and 4 × 1 GB local HDD with 340.4 GFLOPS theoretical top performance

B.3 Forschungshochleistungsrechner ForHlr2

Hardware specification:

- Operating system: Red Hat Enterprise Linux (RHEL) 7.x
- Network: InfiniBand 4X EDR Interconnect
- Peak performance (theoretical in total): 1 PFLOPS
- Main memory (in total): 95 TB
- Cores (in total): 24 161
- Nodes (in total): 1 186

Node specification:

- 8 service nodes, 5 login nodes and 1 152 thin nodes each with 20 cores, each node being equipped with 2 Deca Core Intel Xeon E5-2660 v3 processors with a frequency of 2.6 GHz and 64 GB RAM, 480 GB local SSD with 832 GFLOPS theoretical top performance

- 21 fat nodes each with 48 cores, each node being equipped with 4 Intel Xeon E7-4830 processors with a frequency of 2.1 GHz and 4 NVIDIA GeForce GTX980 Ti graphic cards, at least 1 TB min memory and 4×960 GB local SSD with 1 613 GFLOPS theoretical top performance

Bibliography

- [1] A. Abdulle and Y. Bai. Reduced basis finite element heterogeneous multiscale method for high-order discretizations of elliptic homogenization problems. *Journal of Computational Physics*, 231(21):7014–7036, 2012.
- [2] H. Alber. *Materials with Memory: Initial-Boundary Value Problems for Constitutive Equations with Internal Variables*. Lecture Notes in Mathematics. Springer, Berlin Heidelberg, 2006.
- [3] G. Allaire. Homogenization and two-scale convergence. *SIAM Journal on Mathematical Analysis*, 23(6):1482–1518, 1992.
- [4] G. Allaire. Two-scale convergence and homogenization of periodic structures. *ICTP School on homogenization*, 1993.
- [5] G. Allaire, A. Damlamian, and U. Hornung. Two-scale convergence on periodic surfaces and applications. In *Proceedings of the International Conference on Mathematical Modelling of Flow Through Porous Media*, Singapore, 1996. World Scientific Publication.
- [6] N. Bakhvalov and G. Panasenko. *Homogenisation: Averaging Processes in Periodic Media : Mathematical Problems in the Mechanics of Composite Materials*. Springer, Dordrecht, 1989.
- [7] A. Braides. *Gamma-convergence for Beginners*. Oxford lecture series in mathematics and its applications. Oxford University Press, 2002.
- [8] A. Cauvin and R. B. Testa. Damage mechanics: Basic variables in continuum theories. *International Journal of Solids and Structures*, 36(5):747–761, 1999.
- [9] R. Christensen and K. Lo. Solutions for effective shear properties in three phase sphere and cylinder models. *Journal of the Mechanics and Physics of Solids*, 27(4):315–330, 1979.
- [10] P. Ciarlet. *The Finite Element Method for Elliptic Problems*. Classics in Applied Mathematics. Society for Industrial and Applied Mathematics, 2002.

-
- [11] D. Cioranescu and P. Donato. *An Introduction to Homogenization*. Oxford lecture series in mathematics and its applications. Oxford University Press, 1999.
- [12] E. De Giorgi. G-operators and γ -convergence. In *Proceedings of the International Congress of Mathematicians*, volume 1, page 2, 1983.
- [13] P. H. Dederichs and R. Zeller. Variational treatment of the elastic constants of disordered materials. *Zeitschrift für Physik: A Hadrons and Nuclei*, 259(2):103–116, 1973.
- [14] S. Diebels, A. Jung, Z. Chen, H. Seibert, and T. Scheffer. Experimentelle Mechanik: Von der Messung zum Materialmodell. *Rundbrief GAMM*, 2015.
- [15] Y. Efendiev and T. Y. Hou. *Multiscale Finite Element Methods: Theory and Applications*, volume 4 of *Surveys and Tutorials in the Applied Mathematical Sciences*. Springer, New York, 2009.
- [16] I. Ekeland and R. Témam. *Convex Analysis and Variational Problems*. Classics in Applied Mathematics. Society for Industrial and Applied Mathematics, 1999.
- [17] J. D. Eshelby. The determination of the elastic field of an ellipsoidal inclusion, and related problems. In *Proceedings of the Royal Society of London A: Mathematical, Physical and Engineering Sciences*, volume 241, pages 376–396. The Royal Society, 1957.
- [18] F. Feyel and J.-L. Chaboche. FE2 multiscale approach for modelling the elastoviscoplastic behaviour of long fibre SiC/Ti composite materials. *Computer methods in applied mechanics and engineering*, 183(3):309–330, 2000.
- [19] C. Geiger and C. Kanzow. *Theorie und Numerik restringierter Optimierungsaufgaben*. Springer-Lehrbuch Masterclass. Springer, Berlin Heidelberg, 2002.
- [20] GeoDict. The digital material laboratory. <http://www.geodict.de/>, 2014.
- [21] M. E. Gurtin. *An introduction to continuum mechanics*, volume 158. Academic press, San Diego, 1982.
- [22] W. Han and B. D. Reddy. *Plasticity: Mathematical theory and numerical analysis*, volume 9. Springer, New York Berlin Heidelberg, 2012.
- [23] Z. Hashin. The elastic moduli of heterogeneous materials. Technical report, DTIC Document, 1960.
- [24] G. Holzapfel. *Nonlinear solid mechanics: A continuum approach for engineering*. Wiley, Chichester New York, 2000.

-
- [25] D. E. ISO. 527-1: Kunststoffe-Bestimmung der Zugeigenschaften-Teil 2: Prüfbedingungen für Form- und Extrusionsmassen (ISO/DIS 527-2: 2010). *Deutsche Fassung prEN ISO 527, 2*, 2010.
- [26] F. Jarre and J. Stoer. *Optimierung*. Springer-Lehrbuch. Springer, Berlin Heidelberg, 2013.
- [27] J. Ju. On energy-based coupled elastoplastic damage theories: Constitutive modeling and computational aspects. *International Journal of Solids and Structures*, 25(7):803–833, 1989.
- [28] L. Kachanov. *Introduction to continuum damage mechanics*. Mechanics of Elastic Stability. Springer, 1986.
- [29] E. Kröner. Berechnung der elastischen Konstanten des Vielkristalls aus den Konstanten des Einkristalls. *Zeitschrift für Physik*, 151(4):504–518, 1958.
- [30] E. Kröner. Bounds for effective elastic moduli of disordered materials. *Journal of the Mechanics and Physics of Solids*, 25(2):137–155, 1977.
- [31] C. Kuhn. *Numerical and analytical investigation of a phase field model for fracture*. PhD thesis, Technische Universität Kaiserslautern, Lehrstuhl für Technische Mechanik, 2013.
- [32] H. Lippmann and J. Lemaitre. *A Course on Damage Mechanics*. Springer, Berlin Heidelberg, 1996.
- [33] D. Lukkassen, G. Nguetseng, and P. Wall. Two-scale convergence. *International journal of pure and applied mathematics*, 2(1):35–86, 2002.
- [34] J. Marsden and T. Hughes. *Mathematical Foundations of Elasticity*. Dover Civil and Mechanical Engineering Series. Dover, 1994.
- [35] D. Maurer and C. Wieners. A parallel block LU decomposition method for distributed finite element matrices. *Parallel Computing*, 37(12):742–758, 2011.
- [36] C. Miehe, J. Schotte, and J. Schröder. Computational micro-macro transitions and overall moduli in the analysis of polycrystals at large strains. *Computational Materials Science*, 16(1):372–382, 1999.
- [37] C. Miehe, J. Schröder, and J. Schotte. Computational homogenization analysis in finite plasticity. *Computer methods in applied mechanics and engineering*, 171:3–4, 1999.
- [38] A. Mielke. Evolution of rate-independent systems. In *Handbook of Differential Equations: Evolutionary Equations*, volume 2, chapter 6, pages 461–559. 2005.

-
- [39] A. Mielke and T. Roubíček. *Rate-Independent Systems: Theory and Application*. Applied Mathematical Sciences. Springer New York, 2015.
- [40] A. Mielke and F. Theil. A mathematical model for rate-independent phase transformations with hysteresis. In *Proceedings of the Workshop on "Models of Continuum Mechanics in Analysis and Engineering"*, pages 117–129, 1999.
- [41] A. Mielke and F. Theil. On rate-independent hysteresis models. *NoDEA: Nonlinear Differential Equations and Applications*, 11(2):151–189, 2004.
- [42] A. Mielke and A. M. Timofte. Two-scale homogenization for evolutionary variational inequalities via the energetic formulation. *SIAM Journal on Mathematical Analysis*, 39(2):642–668, 2007.
- [43] T. Mori and K. Tanaka. Average stress in matrix and average elastic energy of materials with misfitting inclusions. *Acta metallurgica*, 21(5):571–574, 1973.
- [44] H. Moulinec and P. Suquet. A numerical method for computing the overall response of nonlinear composites with complex microstructure. *Computer Methods in Applied Mechanics and Engineering*, 157(1-2):69–94, 1998.
- [45] R. Mueller, S. Kolling, and D. Gross. On configurational forces in the context of the finite element method. *International Journal for Numerical Methods in Engineering*, 53(7):1557–1574, 2002.
- [46] S. Murakami. Notion of continuum damage mechanics and its application to anisotropic creep damage theory. *ASME, Transactions, Journal of Engineering Materials and Technology*, 105:99–105, 1983.
- [47] F. Murat and L. Tartar. H-convergence. In *Topics in the mathematical modelling of composite materials*, Progress in Nonlinear Differential Equations and Their Applications, pages 21–43. Birkhäuser Boston, 1997.
- [48] G. Papanicolau, A. Bensoussan, and J. Lions. *Asymptotic Analysis for Periodic Structures*. Studies in Mathematics and its Applications. Elsevier Science, 1978.
- [49] Y. Rabotnov. *Creep Problems in Structural Members*. Applied Mathematics and Mechanics Series. Elsevier, 1969.
- [50] A. Reuss. Berechnung der Fließgrenze von Mischkristallen auf grund der Plastizitätsbedingung für Einkristalle. *ZAMM-Journal of Applied Mathematics and Mechanics*, 9(1):49–58, 1929.
- [51] C. Röhrig, T. Scheffer, and S. Diebels. Mechanical characterization of a short fiber-reinforced polymer at room temperature: Experimental setups evaluated by an

- optical measurement system. *Continuum Mechanics and Thermodynamics*, pages 1–19, 2017.
- [52] E. Sanchez-Palencia and A. Zaoui. *Homogenization techniques for composite media: lectures delivered at the CISM International Center for Mechanical Sciences, Udine, Italy, July 1-5, 1985*. Lecture notes in physics. Springer, 1987.
- [53] J. Schröder. A numerical two-scale homogenization scheme: The FE2-method. In *Plasticity and Beyond: Microstructures, Crystal-Plasticity and Phase Transitions*, pages 1–64. Springer, Vienna, 2014.
- [54] F. Sidoroff. Description of anisotropic damage application to elasticity. In *Physical Non-Linearities in Structural Analysis: Symposium Senlis, France May 27–30, 1980*, pages 237–244. Springer, Berlin Heidelberg, 1981.
- [55] J. Simo and T. Hughes. *Computational Inelasticity*. Interdisciplinary Applied Mathematics. Springer, New York, 2000.
- [56] R. Smit, W. Brekelmans, and H. Meijer. Prediction of the mechanical behavior of nonlinear heterogeneous systems by multi-level finite element modeling. *Computer methods in applied mechanics and engineering*, 155(1-2):181–192, 1998.
- [57] S. Spagnolo. Sul limite delle soluzioni di problemi di cauchy relativi all’equazione del calore. *Annali della Scuola Normale Superiore di Pisa-Classe di Scienze*, 21(4):657–699, 1967.
- [58] S. Spagnolo. Sulla convergenza di soluzioni di equazioni paraboliche ed ellittiche. *Annali della Scuola Normale Superiore di Pisa-Classe di Scienze*, 22(4):571–597, 1968.
- [59] J. Spahn. *An efficient multiscale method for modeling progressive damage in composite materials*. PhD thesis, Technische Universität Kaiserslautern, Lehrstuhl für Technische Mechanik, 2015.
- [60] J. Spahn, H. Andrä, M. Kabel, and R. Müller. A multiscale approach for modeling progressive damage of composite materials using fast Fourier transforms. *Computer Methods in Applied Mechanics and Engineering*, 268:871–883, 2014.
- [61] L. Tartar. Compensated compactness and applications to partial differential equations. In *Nonlinear analysis and mechanics: Heriot-Watt symposium*, volume 4, pages 136–212, 1979.
- [62] M. Thomas and A. Mielke. Damage of nonlinearly elastic materials at small strain - Existence and regularity results -. *Zeitschrift Angewandte Mathematik und Mechanik*, 90:88–112, Feb. 2010.

-
- [63] W. Voigt. *Lehrbuch der Kristallphysik mit Ausschluß der Kristalloptik*. Vieweg+Teubner Verlag, Wiesbaden, 1966.
- [64] E. Weinan, B. Engquist, et al. The heterogeneous multiscale methods. *Communications in Mathematical Sciences*, 1(1):87–132, 2003.
- [65] C. Wieners. A geometric data structure for parallel finite elements and the application to multigrid methods with block smoothing. *Computing and Visualization in Science*, 13(4):161–175, 2010.
- [66] R. D. Williams. Performance of dynamic load balancing algorithms for unstructured mesh calculations. *Concurrency: Practice and experience*, 3(5):457–481, 1991.
- [67] H. Ziegler. *Some Extremum Principles in Irreversible Thermodynamics, with Application to Continuum Mechanics*. Swiss Federal Institute of Technology, 1962.
- [68] H. Ziegler. *An Introduction to Thermomechanics*. North-Holland Series in Applied Mathematics and Mechanics. Elsevier Science, 2012.